Ph.D. DISSERTATION

# Study on Resistive Switching Systems: Demonstration of Neuromorphic Hardware Implementation

by

**Hyungkwang Lim**

**February 2016**

DEPARTMENT OF MATERIALS SCIENCE AND ENGINEERING

COLLEGE OF ENGINEERING

SEOUL NATIONAL UNIVERSITY

# Abstract

Artificial neural networks have been attracted a great interest due to its unique functionality, i.e. 'learning' ability. Recently, the necessity of spiking neural network (SNN) is likely to increase so as to handle dynamic information from our "real world". Regarding the time consuming process of the SNN within *in-silico* method, hardware-based SNNs have received remarkably great attention. In this thesis, memory and switch devices were investigated, then proof-of-concept demonstration was conducted for building blocks of SNNs, i.e. an artificial neuron and synapse.

Short-term synaptic plasticity of faradaic type electrochemical capacitors (ECs) utilizing $TiO_2$ mixed ionic-electronic conductor (MIEC) were reported. Various reactive electrode materials e.g. Ti, Ni, and Cr were employed to emulate redox-related short-term memory (STM) of the artificial synapse. By experiments, it turned out that the potentiation behaviors did not represent unlimited growth of synaptic weight. Instead, the behaviors exhibited limited synaptic weight growth that can be understood by means of an empirical equation similar to the Bienenstock-Cooper-Munro (BCM) rule, employing a sliding threshold. The observed potentiation behaviors were analyzed using the empirical equation and the difference between the different ECs were parameterized.

For the emulation of abrupt conductance fluctuation at the neurons' membrane, three types of non-memory switching systems were examined. First, current-voltage hysteresis of $TiO_2$-based non-faradaic capacitors was investigated to primarily focus on the correlation between the blocking contact and the elasticity, i.e. non-plasticity, of the capacitors' resistance change, in experimental and theoretical methods. The similarity between the spike firing behavior in neurons and the elasticity of the non-faradaic capacitors was addressed. Second, GeSe-based threshold switches (TSs) were examined. Both single (Pt/GeSe/Pt)-and dual-layered

($Cu/SiO_x/GeSe_x/Pt$) TSs exhibited monostable resistance switching, i.e. non-memory switching phenomenon. Towards this end, oscillatory circuits encompassing the TS were considered based on the leaky integrate-and-fire (LIF) neuron model.

Therefore, simulations on the neuronal behavior of neuristor-based leaky integrate-and-fire (NLIF) neurons were conducted based on the threshold switch. The spike firing dynamics of the NLIF neuron was analyzed on two-dimensional phase plane, whose results suggest the dynamics is determined by two nullclines conditional on the variables on the plane, and thus the fixed point also conditional on them. A note should be placed on the operational noise caused by the variability of the threshold switching behavior in the neuron on each switching event. As a consequence, we found that the NLIF neuron exhibits a Poisson-like noise in spike firing, delimiting reliability of information conveyed by individual NLIF neurons. To highlight neuronal information coding at a higher level, a population of noisy NLIF neurons is analyzed in regard to probability of successful information decoding given the Poisson-like noise of each neuron. The result suggests highly probable success in decoding in spite of large variability of individual neurons due to the variability of the threshold switching behavior.

Third, a proof-of-concept demonstration of relaxation oscillator-based leaky integrate-and-fire (ROLIF) neuron circuit was realized by employing an amorphous chalcogenide-based threshold switch and *non-ideal* op-amp. The proposed ROLIF neuron offers biologically plausible features such as analog-type encoding, signal amplification, unidirectional synaptic transmission, and Poisson noise. The synaptic transmission between pre and postsynaptic neurons is achieved through a passive synapse (synaptic resistor). The synaptic resistor coupled with the non-ideal op-amp enables synaptic weight-dependent excitatory postsynaptic potential (EPSP) evolution that evokes postsynaptic neuron's spiking. In an attempt to

generalize our proposed model, we theoretically examine ROLIF neuron circuits adopting different non-ideal op-amps of different gains and slew rates. The simulation results points to the importance of the gain in postsynaptic neuron's spiking irrespective of the slew rate as far as the rate exceeds a particular value, providing the basis of the ROLIF neuron circuit design. We eventually highlight the behavior of a postsynaptic neuron in connection to multiple presynaptic neurons via synapses in terms of the EPSP evolution amid simultaneously incident asynchronous and noisy presynaptic neurons' spikes – which in fact uncovers the beauty of the random noise in spatial integration.

---

**Keywords:** Neuromorphic engineering, Artificial synapse, Artificial neuron, Threshold switch, S-shaped negative differential resistance, Short-term memory, Electrochemical capacitor, Non-faradaic type capacitor, Neuronal noise, Neuristor-based leaky integrate-and-fire neuron, Relaxation oscillator-based leaky integrate-and-fire neuron

**Student Number:** 2010-22768

Hyungkwang Lim

# Table of Contents

# List of Tables

# List of Figures

# List of Abbreviations

| | |
|---|---|
| AI | Artificial Intelligence |
| ANN | Artificial Neural Network |
| BCM | Bienenstock-Cooper-Munro |
| BE | Bottom Electrode |
| CCW | Counter-Clockwise |
| CMOS | Complementary Metal-Oxide-Semiconductor |
| CPU | Central Processing Units |
| CTP | $Cr/TiO_2/Pt$ |
| CW | Clockwise |
| DUT | Device Under Test |
| EC | Electrochemical Capacitor |
| ECM | Electrochemical Metallization |
| EMF | Electromotive Force |
| ESR | Equivalent Series Resistance |
| EPSC | Excitatory Post-Synaptic Current |
| EPSP | Excitatory Post-Synaptic Potential |
| I-V | Current-Voltage |
| ISI | Inter-Spike Interval |
| J-V | Current density-Voltage |
| LIF | Leaky Integrate-and-Fire |
| LTD | Long-Term Depression |
| LTM | Long-Term Memory |
| LTP | Long-Term Potentiation |
| MIEC | Mixed Ionic-Electronic Conductor |
| MOSFET | Metal-Oxide-Semiconductor Field-Effect Transistor |
| $Na^+/K^+$ -ATPase | $Na^+/K^+$ Adenosine TriPhosphatase |
| NDR | Negative Differential Resistance |
| NLIF | Neuristor-based Leaky Integrate-and-Fire |
| NTP | $Ni/TiO_2/Pt$ |

| | |
|---|---|
| PAO | Pearson-Anson Oscillator |
| PDF | Probability Density Function |
| PG | Pulse Generator |
| RAM | Random Access Memory |
| ROLIF | Relaxation Oscillator-based Leaky Integrate-and-Fire |
| SNN | Spiking Neural Network |
| STD | Short-Term Depression |
| STM | Short-Term Memory |
| STP | Short-Term Potentiation |
| TE | Top Electrode |
| TMO | Transition Metal Oxide |
| TS | Threshold Switch |
| TTP | $Ti/TiO_2/Pt$ |
| VCM | Valence Change Memory |

# 1. Introduction

## 1.1. Building blocks of a biological neural network

### 1.1.1. Biological neuron

In biological neural networks, negiboring neurons communicate with each other through 'spike', which is often referred to as action potential. In a neuron, without external stimualtion, the neuron's lipid membrane separating extracellualr and intracellular media stays polarized with a resting potential of approximatedly -70 mV.[1] Ion pumps for $Na^+$ and $K^+$ ions, sodium-potassium adenosine triphosphatase ($Na^+/K^+$ -ATPase), embedded in the lipid membrane, produce certain $Na^+$ and $K^+$ concentration differences between intracelluar and extracelluar media, resulting in the generation of a Nernst potential of approximately -70 mV.[2] Hence, the membrane acts as a biological battery. If the sum of external stimuli is above a certain threshold, voltage-gated ion channels embedded in the membrane are opened, resulting in the flow of ions induced by the electrochemical potential gradient. (see Figure 1.1) Therefore, the polarized membrane is depolarized and the spike is generated, i.e. action potential firing. Spikes are short-lasting since $Na^+/K^+$ -ATPase ion pumps attempt to restore the concentration gradients of $Na^+$ and $K^+$ towards the membrane's resting state. That is, the spike firing within neurons is a matter of 'elasticity' regarding the state of the membrane. The firing characteristic of neurons is often reffered to as 'all-or-non-firing' in light of the failed and successful spike generation on the basis of the threshold.

Macroscopically, a set of spikes, i.e. spike train, is a encoding result of input soma current of the neuron of interset. Generally, the number of spikes per unit time, i.e. activity, increases monotonically with soma current. This phenomenon is widely known for neuron response function or gain function.

Therefore, the neuron can encode change of soma current into activity, reflecting the analog-type encoding characteristic of the biological neuron. When we consider a sensory part of the mamallian neural network, the biological neuron can also encode physical magnitue of real world. The role of the sensory part is to convert continuous physical magnitude such as angle of light bar, wind direction, and sound intensity into different magnitude of soma current. The relationship between the physcical magnitue of real world and activity is often referred to as tuning curve, representing encoding selectivity of the biological neuron.

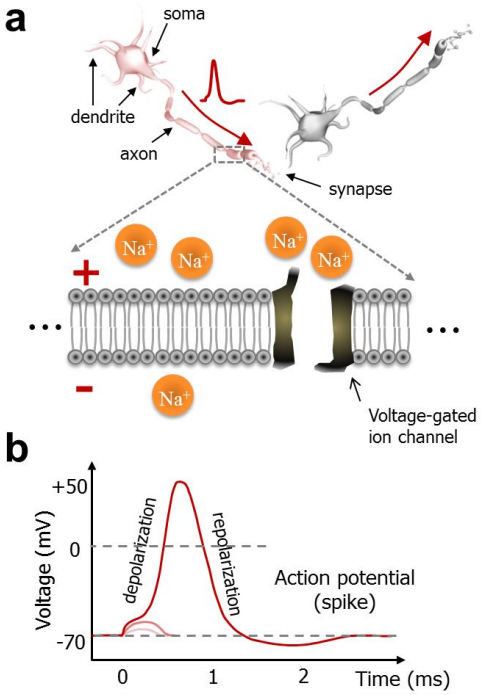


Figure 1.1 Schematics of the (a) biological neuron and (b) action potential (spike). Only sodium ions are indicated in the schematic for symplicity.

### 1.1.2. Biological synapse

A synapse is located between neighboring neurons, serving as a node defining the connection between the neurons. Neurons and chemical synapses form a large-scaled complex neural network carrying out higher-level functionalities such as learning and memory. Unlike CPUs (Boolean systems), neural networks are analog systems. That is, the amount of information which can be stored in a single synapse is unlimited, whereas in the case of Boolean systems only one of the binary numbers, '0' and '1', can be stored at a memory node.The difficulties in predicting the collective behavior of complex neural networks arise from the analog behavior of synapses and the random distribution of neurons.[3, 4]

It is known that there are two types of synapse in the mammalian brain: the electrical synapse and the chemical synapse.[5] An electrical synapse allows 'bidirectional' electrical signal flow between the neighboring neurons by means of the drift of related ions. Note that the drift results from an electric potential gradient, i.e. electric field, through the electrical synapse. That is, the signal flow does not involve chemical reactions. In this case, presynaptic and postsynaptic neurons are defined by the signal flow direction, i.e. a signal flows from a presynaptic to a postsynaptic neuron. In the case of a chemical synapse, signal flow is 'unidirectional', since the flow of neurotransmitters (chemical messengers) is restricted to one direction, from a presynaptic neuron, releasing neurotransmitters, to a postsynaptic neuron, receiving the neurotransmitters. (See Figure 1.2) This signal transmission process is believed to involve $Ca^{2+}$- related complicated chemical reactions in the postsynaptic neuron.[6-8] Activation of these chemical reactions yields an increase in the strength of the correlation between the two adjacent neurons.

Chemical synapses, rather than electrical synapses, are thought to be involved in learning and memory. Our main concern is therefore with chemical synapses and their short-term memory (STM) and long-term

memory (LTM) effects. For simplicity, we term a chemical synapse as a 'synapse' without modifiers. 'Neurons that fire together, wire together', the quote that Hebb mentioned, abstractly describes the activity-dependent plasticity of a synapse.[9] In this quote, neuron firing means that the membrane of each neuron is strongly depolarized, resulting in action potential firing, i.e. a neuron's activation. When both presynaptic and postsynaptic neurons are activated, the correlation between the neurons strengthens. The strength of the correlation is defined as the 'synaptic weight'. An increase (decrease) of synaptic weight is referred to as potentiation (depression). Furthermore, depending on the duration of the changed synaptic weight, the change is classified as short-term potentiation (STP) and depression (STD), or long-term potentiation (LTP) and depression (LTD).

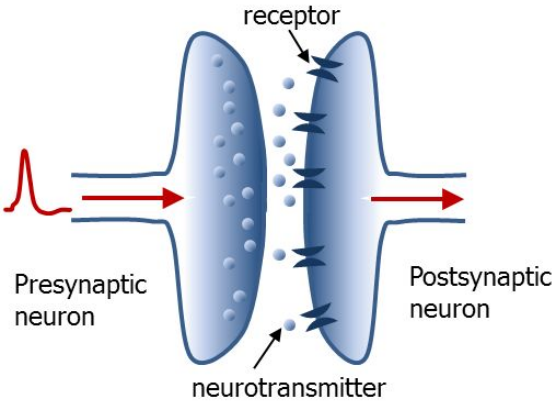


Figure 1.2 A schematic of the chemical synapse

## 1.2. Overview on the neuromorphic engineering

### 1.2.1. What is the artificial neural network?

A megatrend in current technology development appears towards human beings' less working life. 'Work' in this term does not necessarily mean only occupational activity. Rather, it encompasses all activities that can be done only by human beings. Decision-making is an example that human beings very often encounter in daily life and cannot be done by 'things'. Thus, human beings can work less to a great extent if things are able to do the work instead. In this regards, artificial intelligence (AI) has recently been attracting great attention and methodology for AI – deep learning[10] – has been popularly invoked. It should be noted that AI in this sense means decision-making ability on the basis of training or learning with training sets. The artificial neural network (ANN) underlies deep learning, which is inspired by brains and their information processing pathways. The ANN takes after the brain considering their structure that consists of artificial neurons and synapses. However, there exists a large disparity in detailed behavior between the ANN and brain. The binary states are given to each artificial neuron in the ANN in response to the sum of the inputs plus bias – the neuron is often expressed by the Heaviside step function or sigmoid function.[10] These artificial neuron models largely differ from the biological neuron that represents analogue information by means of spiking dynamics.[11, 12]

### 1.2.2. Necessity of the spiking neural network and hardware building blocks

The spiking neural network (SNN) is another class of network for AI, which is distinguished from the aforementioned ANN considering its neural

representation on the spiking (dynamic) grounds.[13-15] Spiking neurons fire spikes upon the membrane potential crossing a threshold for spiking. The membrane potential evolves in due course with incident synaptic current. In addition, spiking activity – defining how often spiking occurs – significantly matters in representing analog-type information. The spiking neuron real-time responses to time-dependent synaptic current, making it suitable for real-time information representation, which interacts with the real world.[13] Given the spiking neuron's dynamic response, the physiological spatiotemporal learning rules, e.g. the Hebbian learning rules, may be directly applied to training the SNN. In this regards, the SNN shares more similarities with the biological neural network than the ANN.

Both ANN and SNN are often realized on computers by emulation means – popularly referred to as 'in silico' network. In supervised learning, in silico synapses are trained so as to minimize a disparity between the calculated output and the desired one – so-called a cost function.[10, 16] The cost function minimization requires mathematical algorithms such as a gradient descent method and its variations. By all rights, the calculation efficiency can be largely improved by making use of a more efficient algorithm such as a stochastic gradient descent method.[17] However, the calculation is still costly when associated with a large number of synapses, hidden layers, and training sets.[10] Calculating the SNN appears even more daunting given the requirement of time-domain calculation of spiking and synaptic weight change. A need for a large amount of computational resource and the consequent long computation time are hardly capable of real-time interaction with the world.

A workaround solution to the above-mentioned inherent issues is perhaps to implement such SNNs in physics-based hardware, which no longer requires such time-consuming calculations. Building a hardware SNN using proper 'unit blocks' is of significant concern. Regarding the current maturity

level of hardware SNN technology improvements in building blocks, plasticity-induction protocols, and learning protocols at the network level definitely need to be continued. In particular, as the entire network works on building block grounds, placing emphasis on underpinning artificial neurons most likely lays the foundation of success in the technology.

### 1.2.3. Conventional and current approaches towards the hardware implementation

To date, a great deal of efforts have been made to realize artificial hardware neurons and synapses, using conventional complementary metal-oxide-semiconductor (CMOS) technologies.[18, 19] This CMOS-based approach has been the mainstream approach of neuromorphic (hardware) engineering. (see Figure 1.3)

A recent emerging research trend is the increasing adoption of alternative approaches to realize artificial neurons and synapses. These emerging approaches differ from the mainstream approach in that neural functionalities are implemented by introducing functional materials-based elements that could partly replace CMOS-based elements in the former.[5] One of the advantages of these new approaches is that it may enable the circuitry of SNNs to be substantially simplified by using a less number of CMOS elements than the conventional approach. An artificial neuron example of such approaches is a recent breakthrough by Pickett et al., who achieved the LIF neuron by using two pairs of a Mott insulator and a capacitor.[20] In this system, threshold switching phenomenon of the Mott insulator was employed to realize 'elasticity' of the spike, i.e. rapid alteration of the membrane potential. Artificial synapses also have been realized by means of various physical concepts, e.g. ferroelectricity,[21-23] the phase change of higher chalcogenides,[24, 25] ferromagnetism,[26, 27] and nanoionics.[28-34] In these systems, their conductance (or resistance) is taken

as the synaptic weight. Among these candidates, nanoionic systems exhibiting the valence change memory (VCM) effect, coined by Waser et al,[35] appear to meet the requirement of 'unidirectional signal transmission' of a chemical synapse. In a two-terminal passive VCM system, a particular change in the conductance (or resistance) is made by only one of the two electric field directions. Therefore, this polarity-dependent synaptic weight change perhaps enables unidirectional potentiation to be realized.

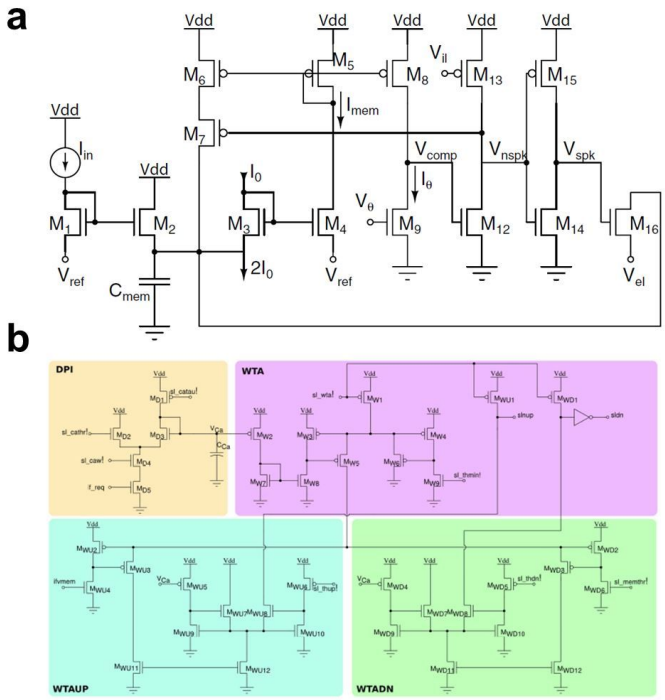


Figure 1.3 Equivalent circuits of (a) an artificial neuron[18] and (b) an artificial synapse[19] based on CMOS elements.

## 1.3. Bibliography


[1] A. L. Hodgkin, A. F. Huxley, *J. Physiol.*, 117, 500 (1952).

[2] J. C. Skou, *Biochim. Biophys. Acta*, 23, 394 (1957).

[3] B. Cheng, D. M. Titterington, *Statist. Sci.*, 2 (1994).

[4] J. J. Hopfield, *Proc. Natl. Acad. Sci. USA*, 79, 2554 (1982).

[5] D. S. Jeong, I. Kim, M. Ziegler, H. Kohlstedt, *RSC Adv.*, 3, 3169 (2012).

[6] J. Lisman, *Proc. Natl. Acad. Sci. USA*, 86, 9574 (1989).

[7] J. Lisman, *Trends Neurosci.*, 17, 406 (1994).

[8] R. C. Malenka, Nicoll, R. A., *Science*, 285, 1870 (1999).

[9] D. O. Hebb, *The organization of behavior*, Wiley & Sons, New York, USA 1949.

[10] Y. LeCun, Y. Bengio, G. Hinton, *Nature*, 521, 436 (2015).

[11] P. Dayan, L. F. Abbott, *Theoretical Neuroscience*, The MIT Press, Cambridge, MA, USA 2001.

[12] W. Gerstner, W. M. Kistler, *Spiking Neuron Models: Single Neurons, Population, Plasticity*, Cambridge University Press, Cambridge, UK 2002.

[13] C. Eliasmith, C. H. Anderson, *Neural Engineering*, The MIT Press, Cambridge, MA, USA 2004.

[14] S. Ghosh-Dastidar, H. Adeli, *Neural Networks*, 22, 1419 (2009).

[15] D. Goodman, R. Brette, *Front. Neuroinform.*, 2, 5 (2008).

[16] Y. LeCun, *Generalization and Network Design Strategies: Connectionism in Perspective,*(Eds: R. Pfeifer, Z. Schreter, F. Fogelman, L. Steels), Elsevier, Zuich, Switzerland, 1989.

[17] L. Bottou, O. Bousquet, *The Tradeoffs of Large Scale Learning: Advanced in Neural Information Processing Systems 20,*(Eds: J. C. Platt, D. Koller, Y. Singer, S. Roweis), The MIT Press, Cambridge, MA, USA, 2007.

[18] G. Indiveri, B. Linares-Barranco, T. J. Hamilton, A. van Schaik, R.

Etienne-Cummings, T. Delbruck, S.-C. Liu, P. Dudek, P. Häfliger, S. Renaud, J. Schemmel, G. Cauwenberghs, J. Arthur, K. Hynna, F. Folowosele, S. SAÏGHI, T. Serrano-Gotarredona, J. Wijekoon, Y. Wang, K. Boahen, *Front. Neurosci.*, 5, 73 (2011).

[19] N. Qiao, H. Mostafa, F. Corradi, M. Osswald, F. Stefanini, D. Sumislawska, G. Indiveri, *Front. Neurosci.*, 9, 141 (2015).

[20] M. D. Pickett, G. Medeiros-Ribeiro, R. S. Williams, *Nat. Mater.*, 12, 114 (2012).

[21] A. Chanthbouala, V. Garcia, R. O. Cherifi, K. Bouzehouane, S. Fusil, X. Moya, S. Xavier, H. Yamada, C. Deranlot, N. D. Mathur, M. Bibes, A. Barthélémy, J. Grollier, *Nat. Mater.*, 11, 860 (2012).

[22] Y. Nishitani, Y. Kaneko, M. Ueda, T. Morie, E. Fujii, *J. Appl. Phys.*, 111, 124108 (2012).

[23] Min Y. Sung, Eisuke Tokumitsu, Hiroshi Ishiwara, *Jpn. J. Appl. Phys.*, 38, 2289 (1999).

[24] D. Kuzum, R. G. D. Jeyasingh, B. Lee, H. S. P. Wong, *Nano Lett.*, 12, 2179 (2011).

[25] M. Suri, O. Bichler, D. Querlioz, B. Traoré, O. Cueto, L. Perniola, V. Sousa, D. Vuillaume, C. Gamrat, B. DeSalvo, 112, 054904 (2012).

[26] P. Krzysteczko, J. Münchenberger, M. Schäfers, G. Reiss, A. Thomas, *Adv. Mater.*, 24, 762 (2012).

[27] W. Xiaobin, C. Yiran, X. Haiwen, L. Hai, D. Dimitrov, *IEEE Electron Device Lett.*, 30, 294 (2009).

[28] T. Chang, S.-H. Jo, W. Lu, *ACS Nano*, 5, 7669 (2011).

[29] S. H. Jo, T. Chang, I. Ebong, B. B. Bhadviya, P. Mazumder, W. Lu, *Nano Lett.*, 10, 1297 (2010).

[30] Q. Lai, L. Zhang, Z. Li, W. F. Stickle, R. S. Williams, Y. Chen, *Adv. Mater.*, 22, 2448 (2010).

[31] T. Ohno, T. Hasegawa, A. Nayak, T. Tsuruoka, J. K. Gimzewski, M.

Aono, 99, 203108 (2011).

[32] T. Ohno, T. Hasegawa, T. Tsuruoka, K. Terabe, J. K. Gimzewski, M. Aono, *Nat. Mater.*, 10, 591 (2011).

[33] Y. Shimeng, W. Yi, R. Jeyasingh, D. Kuzum, H. S. P. Wong, *IEEE Trans. Electron Devices*, 58, 2729 (2011).

[34] M. Ziegler, R. Soni, T. Patelczyk, M. Ignatov, T. Bartsch, P. Meuffels, H. Kohlstedt, *Adv. Funct. Mater.*, 22, 2744 (2012).

[35] R. Waser, R. Dittmann, G. Staikov, K. Szot, *Adv. Mater.*, 21, 2632 (2009).

# 2. Resistive switching systems for neuromorphic engineering

## 2.1. Introduction

Resistive switching phenomena have been attracted great interest for an application of the next-genration non-volatile memory.[1, 2] For instance, two-dimensional crossbar array resistive switching memories have been popularly investigated for the practical use as a random access memory (RAM).[3, 4] Generally, cell selectors such as diodes or TSs are employed to prevent the sneak current path in the passive crossbar array structure.[3, 4] The TS is known to exhibit a monostable resistance state, so that TS works as a 'resistance-switch' rather than a memory.[5, 6] Regarding the polarity-independent switching behavior, the TS has an advantage for being embedded into the crossbar array structure with both unipolar-and bipolar-type resistive switching memories.

Recently, neuromorphic engineers pay attention to resistive switching phenomena in light of electronic replica of the biological neural system. For instance, a synapse is known to have an analog-type information memory. Therefore, the memory effect of the resistive switching system could be one of the prospective candidates of electronic replica.[7] On the other hand, the biological neuron generates spike, i.e. action potential, which is the result of 'elastic' conductance fluctuation of the membrane rather than 'plastic'. Therefore, non-memory resistive switching phenomenon, e.g., threshold switching, is more promising phenemenon than the memory switching for emulating spike firing of the bilogical neuron.

Reflecting the well-known resistive switching features, $TiO_2$ mixed ionic-electronic conductor (MIEC) was chosen in this study. Electrode materials

may also affect point defect migration in an MIEC, as the boundary conditions of point defect dynamics greatly rely on the reactivity of the electrode material. Here, Pt was employed as the material for a bottom electrode (BE) for two reasons: (i) an inert Pt electrode most likely forms a blocking contact (no redox reaction) with the MIEC in the overpotential range that was chosen in this study, thus simplifying the boundary conditions and (ii) Pt significantly lowers dc electronic conduction due to either its high work function, which causes resulting in a high Schottky barrier, or its chemical inertness that prevents the reduction, i.e. self-doping, of $TiO_2$. Both inert (Pt) and reactive (Cr, Ni, Ti) electrodes were employed for Top electrode (TE). In Pt/$TiO_2$/Pt cell, redox reaction at both MIEC-electrode junction might be hindered by the blocking-contact so that we named the cell as a 'non-faradic' type, whereas 'faradaic' type (Cr, Ni, Ti)/$TiO_2$/Pt cells might undergo redox reaction at TE-MIEC junction. Note that, since reactive electrodes were used, the two-terminal systems in this study are hypothesized to be 'electrochemical capacitors' (ECs).

Higher chalcogenides are known to represent the threshold switching phenomenon. In this study, an amorphous $GeSe_x$ layer was employed for both single- and dual-layered TSs. The threshold switching phenomenon was demonstrated by employing both a quasi-static measurment and a short-pulse measurement. Phenomenolgical differesistnace of monostable resistance switching between two TSs will be introduced in terms of s-shaped negative differential resistance (NDR) phenomenon.

## 2.2. Resistive switching systems based on $TiO_2$

### 2.2.1. Experimental

***$TiO_2$-based cell fabrication***: The non-faradaic and faradaic type cells were TE/$TiO_2$/BE stacks. A schematic of the cross-section of the cell is shown in Figure 2.1a. Inert Pt electrodes were used as BEs. A 50 nm thick Pt blanket BE was deposited onto a thin Ti blanket film (10 nm) formed on a thermally oxidized Si wafer using electron-beam evaporation at room temperature. Then, deposition of 50 and 75 nm $TiO_2$ blanket films using rf reactive sputtering at room temperature followed for non-faradaic and faradaic type cell, respectively. Finally, circle-shaped 50 nm thick reactive TEs (Pt, Cr, Ni, and Ti) were formed on top of the $TiO_2$ film using electron-beam evaporation and patterned using a shadow mask. (see Figure 2.1b) 50 nm thick Pt layers were in situ deposited on top of the TEs (Cr, Ni, and Ti) to avoid the oxidation of the reactive electrodes by oxygen gas in air. For convenience, the Cr/$TiO_2$/Pt, Ni/$TiO_2$/Pt, and Ti/$TiO_2$/Pt faradaic type cells are named as CTP, NTP, and TTP, respectively.

***Quasi-static measurments*:** The measurements on the fabricated non-faradiac type cell was performed using a CHI700 potentiostat at different voltage sweep rates in various voltage ranges. A voltage was applied to the top electrode while the bottom electrode was grounded. The current density-voltage (J-V) loops shown in this paper were taken from consecutive J-V loops, excluding the first-cycle loops. The first-cycle loops always started from a zero current. Current-voltage (I-V) measurements on the faradaic type cells was conducted by using a Keithley 236 Source Measurement Unit.

***Short-term memory effect measurements*:** The short-term memory (STM) behavior was measured on the faradaic type cells by applying voltage pulse trains using a Tektronix AFG3101 and reading the response using a Tektronix TDS5104 oscilloscope. In the measurements, a voltage was applied to the TE while the BE was grounded.

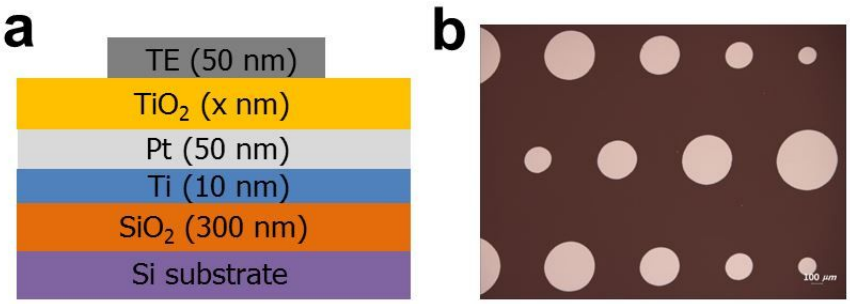


Figure 2.1 (a) A schematic of the cross-section of the $TiO_2$-based cell. (b) The optical image of the fabricated $TiO_2$-based cell from top view.

### 2.2.2. Non-faradaic type cell

A schematic diagram of the fabricated Pt/$TiO_2$/Pt junction sample is drawn in the top left inset of Figure 2.2. Insomuch as the fabricated cells are capacitor-shaped and believed to involve no redox reaction in the chosen voltage range, they could be regarded as non-faradaic capacitors. Consecutive current density-voltage (J-V) loops of the Pt/$TiO_2$/Pt capacitor are plotted in Figure 2.2a, measured by applying triangle-shaped voltage pulses at a voltage sweep rate of 0.1 V $s^{-1}$. The applied voltage pulses are shown in the bottom right inset of Figure 2.2a. The J-V loops represent reproducible 'clockwise' (CW) hysteresis with a reverse current flow (current flow in the opposite direction to the applied voltage) as can be more clearly seen in Figure 2.2b. It is observed that the current is reversed at approximately 0.4 V during the upward sweeps and at approximately 0.9 V during the downward sweeps. However, in the high voltage region, the J-V loci exhibit 'counter-clockwise' (CCW) hysteresis. Thus, the J-V loops show both CW and CCW hysteresis behaviors, crossing each other at a particular voltage (ca. 1 V). The J-V loops were found to scale with the TE area. Currents at a read-out voltage of 1 V for the capacitors with five different pad-sizes ($1.7 \times 10^{-4}$, $5.3 \times 10^{-4}$, $1.1 \times 10^{-3}$, $1.9 \times 10^{-3}$, and $2.6 \times 10^{-3}$ $cm^2$) are plotted in the inset of Figure 2.2b, showing linearity with respect to the pad-size. This suggests that the current shown in Figure 2.2 does not flow through localized current paths.

In order to fully observe the CW hysteresis in detail, a range of applied voltage was narrowed down to 0–0.6 V and the voltage sweep rate was varied from 0.001 to 1 V $s^{-1}$. The measured J-V loops are plotted in Figure 2.3. It can be seen that the measured current increases with the voltage sweep rate, which is a typical character of displacement current in highly resistive dielectric materials having very low dc electronic current. The

contribution of displacement current to the measured current can be confirmed by evaluation of the overall charge involved in the J-V loops, which can be performed by integrating the measured current over time. As can be seen in the inset of Figure 2.3a, the positive charge density attributed to the positive current at different voltage sweep rates (filled squares) is the same as the negative charge density (open squares), implying that the net charge change is zero regardless of the voltage sweep rates.

Unlike the CW hysteresis, the CCW hysteresis in the high voltage region was found to disappear at low voltage sweep rates as shown in Figure 2.4. The ratio of a current density at a particular voltage during a downward sweep ($J_{down}$) to that of the same voltage during an upward sweep ($J_{up}$) was taken as a parameter representing the CCW hysteresis. Ratios larger than unity, therefore, indicate CCW hysteresis. As shown in Figure 2.4, at a voltage sweep rate of 0.001 V $s^{-1}$, the CCW hysteresis fades away within the first three J-V cycles. If the current in this CCW is attributed to dc electronic current, the CCW hysteresis implies a resistance change rather than a time-dependent displacement current. Increasing the voltage sweep rate makes the CCW hysteresis remain for more cycles, as in the 0.01 and 0.1 V $s^{-1}$ cases, as shown in Figure 2.4. For the three rates, 0.1, 0.01, and 0.001 V $s^{-1}$, the time intervals between the current measurements at 1.5 V during the upward and downward sweeps are 10, 100, and 1000 s, respectively. Thus, one may estimate the CCW hysteresis to retain itself for at least 100 s, since the CCW hysteresis at 0.01 V $s^{-1}$ still somehow exists.

For the quantitative understanding of the J-V hysteresis behavior, numerical calculation of J-V behavior for a one dimensional electrode/MIEC/electrode non-faradaic capacitor was performed. In a non-faradaic capacitor, the interface between the MIEC and the electrode forms a blocking contact for oxygen vacancies so that their number is conserved within the capacitor. Time-dependent dc ionic conduction was calculated

using the drift–diffusion equation and Fick's second law with blocking contact boundary conditions. For dc electronic conduction, the drift-diffusion of electrons, i.e. band conduction, was taken as their conduction mechanism. The band offset at the interface, varying on the electric field assigned to the Helmholtz layer, was employed as the boundary conditions.[8] A quasi-static approximation was employed to simplify this calculation in a time domain. Considering the large diffusion coefficient difference between an electron and oxygen vacancy, the use of this approximation is reasonable. Finally, the total current including the aforementioned dc current and displacement current was evaluated as a function of time and voltage. Details of the calculation procedures are described in the Supplementary information. The configuration of the model system is schematically illustrated in Figure 2.5.

Oxygen vacancy migration coefficients, e.g. diffusion coefficient ($D_{Vo}$) and mobility ($\mu_{Vo}$), are critical parameters for the calculation. The areal density of oxygen vacancies ($\rho$) is also an important parameter. The geometries of the configuration, e.g. the thicknesses ($d_1$ and $d_3$) of the two Helmholtz layers and that ($d_2$) of the MIEC, as well as their relative permittivities ($\varepsilon_{r1}$, $\varepsilon_{r3}$, and $\varepsilon_{r2}$), serve as parameters as well. Electronic properties such as the Schottky barrier height ($\phi_b$) and the effective mass ($m_e$) of an electron are also of concern, and equivalent series resistance (ESR) and lattice temperature must also be taken into consideration.

The calculated J-V hysteresis loop at a voltage sweep rate of 0.1 V $s^{-1}$ is plotted in Figure 2.6a. The parameters used for this calculation are listed in Table 2.1, which, in fact, gave the best fitting results. The J-V loop was taken from consecutive J-V loops except the first-cycle one, and thus the initial conditions such as distributions of oxygen vacancies, electrons, and Galvani potential in the MIEC were not of equilibrium. However, the initial conditions of the first-cycle loop calculation were always of equilibrium so

that the calculated loop started from zero current. The calculated J-V loop is found to be in good agreement with the experimental J-V loops shown in Figure 2.2a, exhibiting CW and CCW hysteresis behaviors and their crossing at approximately 1 V. As explained in the Supplementary information, the calculated current density is attributed to four major contributions, i.e. dc ionic conductions (drift and diffusion of oxygen vacancies), displacement current, and dc electronic conduction. The first three contributions are position-dependent. The center point of the model system (at a distance of 25 nm from the left (right) interface), where the contribution of displacement current is minimum, was taken for the results shown in Figure 2.6b, so that the dc ionic conduction behavior can be clearly shown. The contributions of dc ionic and electronic conductions are separately plotted in Figure 2.6b as a function of time, so that their contributions to the total current at given times can be seen. Note that the dc electronic conduction and total current are position-independent as long as the number of oxygen vacancies is conserved (see Supplementary information)

In Figure 2.6b, it is observed that the CCW hysteresis in the high voltage region (>~1 V, which corresponds to ~12 to 30 s) is attributed to dc electronic conduction rather than the ionic current, whereas the CW hysteresis in the low V region is mainly due to the ionic current. Therefore, the experimental CCW hysteresis is most likely of dc electronic current, and thus the hysteresis implies 'resistance' hysteresis. In contrast, the CW hysteresis in the low voltage region does not signify hysteretic resistance because the current in that case is not of dc electronic conduction. In the low voltage region, the contribution of dc electronic current is negligible as can be seen in Figure 2.6b, however, the contribution is still positive as the slope of the Fermi level, for instance, at a time of 40 s, i.e. 0 V, is still negative (see Figure 2.6e). In fact, for the whole voltage range, the electronic current is positive.

From the aforementioned experimental features as well as calculation results, regarding the CW hysteresis in the low voltage region, it can be estimated that the CW hysteresis arises from the migration of charged point defects confined within the MIEC. The low diffusion coefficient or mobility of oxygen vacancies in $TiO_2$ may be the reason for voltage-sweep-rate-dependent CW hysteresis behaviors shown in Figure 2.3. Generally, in an electrolyte, the nonlinearity of current–voltage behavior in J-V measurements is evolved through the time-dependent redistribution of Galvani potential, and the redistribution arises from the migration of ions with a finite diffusion coefficient. Unless sufficient time for the ions to respond to an applied voltage is given, the redistribution of Galvani potential cannot be achieved. In that case, the average electric field matters in current measurements. Therefore, linear current–voltage behavior appears.[9] Moreover, as shown in Figure 2.3a, the net change in charge density for each J-V cycle is zero. This most likely means no change in the number of oxygen vacancies during each J-V cycle, i.e. the Pt/$TiO_2$/Pt capacitors are closed systems for oxygen vacancies with a blocking contact, which allows no redox reaction. That is, the oxygen vacancies related to the ionic current are confined within the MIEC, which is the crucial evidence supporting the blocking-contact-hypothesis.

It should be noted that the above-mentioned capacitive behavior differs from that of normal dielectrics whose dielectric constants are attributed to molecular polarizabilities. Otherwise, the displacement currents in Figure 2.3 approximately give dielectric constants of $TiO_2$ (>500), which are much higher than that of any possible $TiO_2$ phases.

Regarding the CCW hysteresis, the calculation results revealed that it is a result of the evolution of electromotive force (EMF) for electronic conduction. Voltage division in the model system at a given voltage identifies the EMF evolution for electronic conduction. Figure 2.6c and 2.6d

show hysteretic voltage division in three series capacitors, i.e. left and right Helmholtz layers and the MIEC in Figure 2.5. Insomuch as a positive voltage sweep was applied to the right electrode of the model system, the left Helmholtz layer is located at the cathode where electrons are injected into the MIEC. A higher voltage assigned to the left Helmholtz layer ($d_1$) leads to a higher electron injection. In fact, electronic current along the capacitor is most likely controlled by the electron injection through the cathode interface.[10] Regarding the quasi-static electronic current in the capacitor, a higher electron injection through the cathode interface leads to a higher electron ejection through the anode interface. Therefore, as the electron injection increases, the voltage division in the right Helmholtz layer ($d_3$) becomes larger, which increases the ejection current. As shown in Figure 2.6c, the voltage hysteresis is CCW, corresponding to the CCW J-V hysteresis. However, for oxygen vacancies, their drift–diffusion is a matter of the voltage assigned to the MIEC ($d_2$) since they are confined within the MIEC. This voltage represents the CW hysteresis shown in Figure 2.6c, so that ionic current density versus voltage hysteresis is CW.

The EMF evolution is likely attributed to the finite diffusion coefficient of oxygen vacancies in the MIEC, at high voltage sweep rates, oxygen vacancies hardly take enough time to achieve steady state concentration distribution as well as Galvani potential distribution. Consequently, during the downward sweep, i.e. the depolarization process, the capacitor keeps the electrical energy stored during the upward sweep to some extent. Then, the stored energy serves as EMF for electrons, leading to the positive $J_{down}/J_{up}$ ratio, as shown in Figure 2.4. In addition, decreasing a voltage sweep rate leads to the decrease of the EMF evolution owing to the increase of time given to oxygen vacancies. Therefore, the CCW hysteresis eventually disappears at low voltage sweep rates as experimentally identified (see Figure 2.4).

According to the calculation results, the intersection of CW and CCW hysteresis loops, shown in Figure 2.2, implies a transition between ionic and electronic conduction. While the number of oxygen vacancies is conserved in the non-faradaic system, their contribution to electric conduction is limited, as a large decrease in ionic contribution can be seen in the time range of approximately 16–25 s, in Figure 2.6b. For electrons, their reservoir is always connected to the capacitor under electrical measurements so that their number is not limited. Thus, at high electric fields, dc electronic conduction becomes prominent, showing an ionic-to-electronic conduction transition with an increase in voltage. In contrast, during the downward sweep, the reverse transition, i.e. electronic-to-ionic conduction transition, takes place at approximately 30 s as in Figure 2.6b.

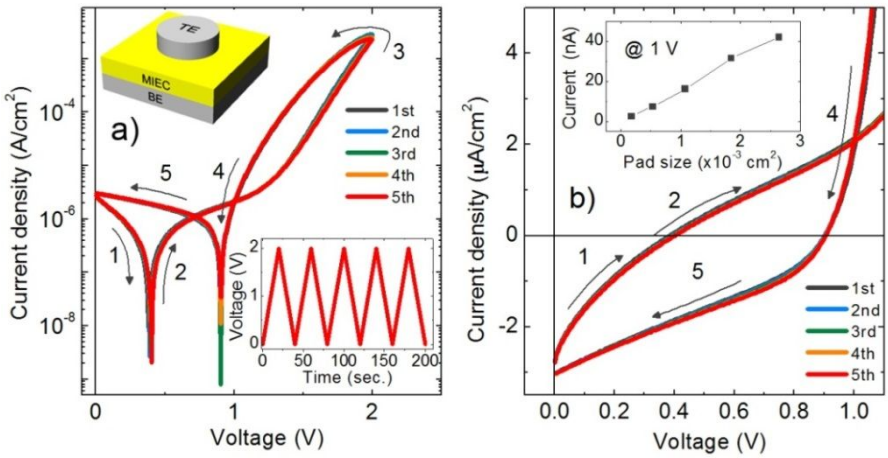


Figure 2.2 J-V characteristics. (a) Consecutive J-V loops, apart from the first-cycle loop, of the Pt/$TiO_2$/Pt capacitor under the applied voltage cycles shown in the bottom right inset. (b) J-V curves re-plotted on a linear scale. The inset denotes current values at 1 V of the capacitors with five different pad-sizes.

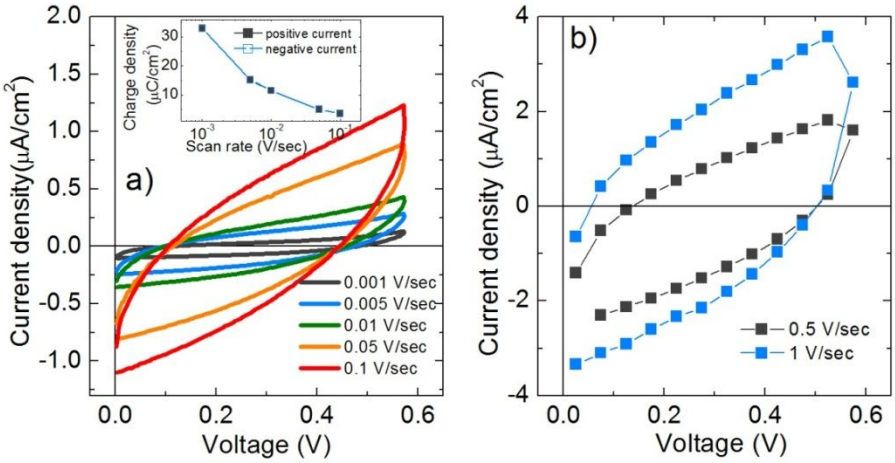


Figure 2.3 J-V hysteresis depending on a voltage sweep rate. (a) J-V loops of the capacitor at different voltage sweep rates. The inset denotes the charge density integrated over time periods in which positive currents flow (filled squares) and negative currents flow (open squares). (b) J-V loops at the higher voltage sweep rates.

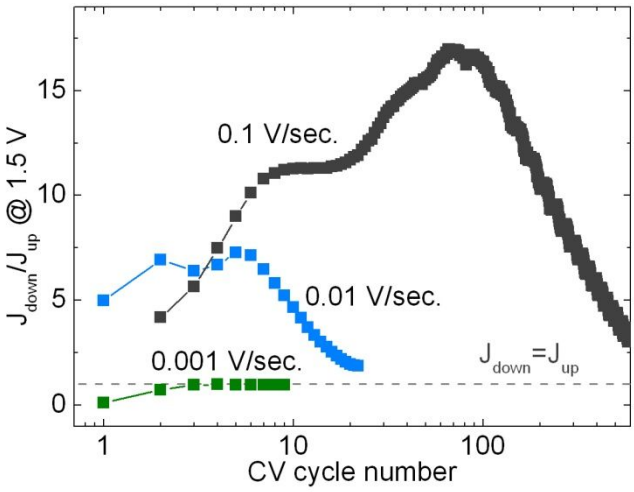


Figure 2.4 CCW hysteresis depending on a voltage sweep rate. Change of the CCW hysteresis in the high voltage region with respect to J-V cycle number at different voltage sweep rates.

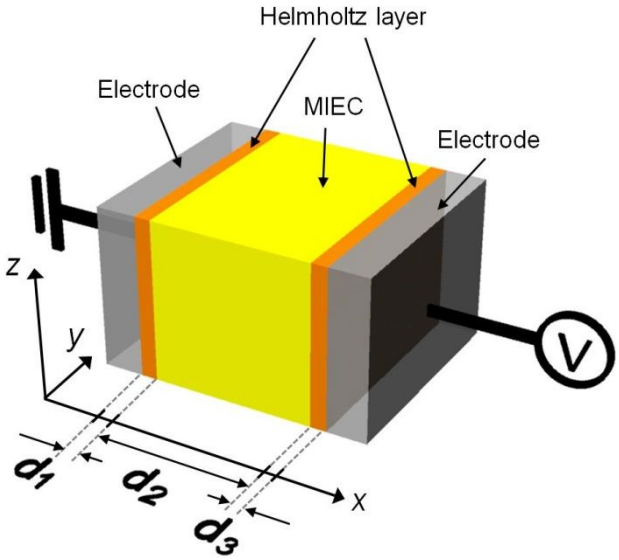


Figure 2.5 Schematic of a non-faradaic capacitor model system.

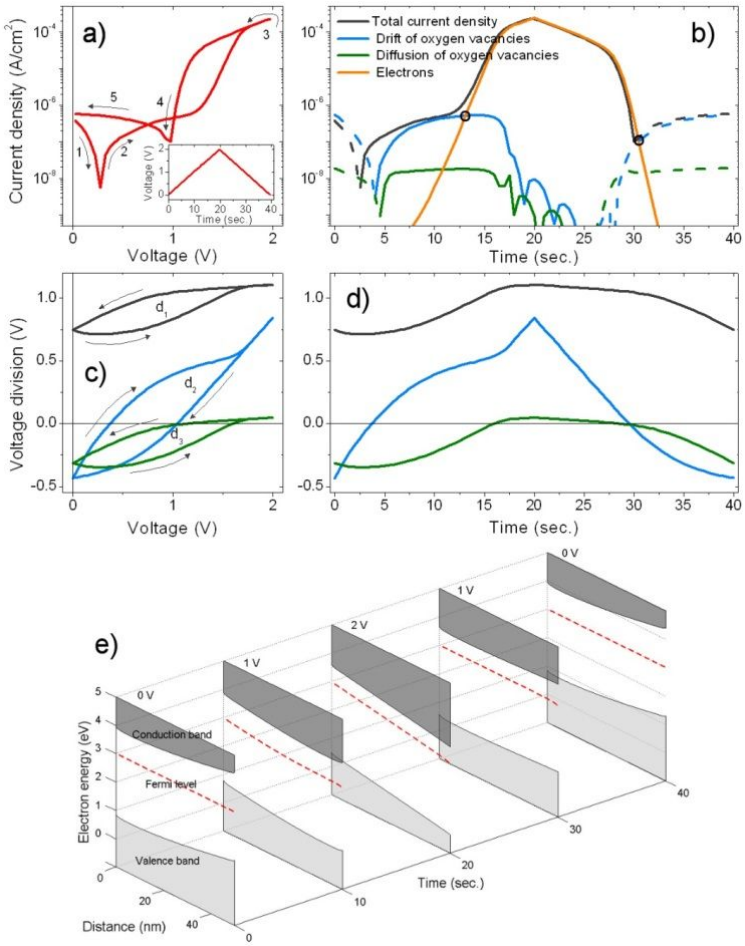


Figure 2.6 Calculation results. (a) Calculated J-V loop under the voltage-time profile shown in the inset. (b) At the center of $TiO_2$ in the model system, the contributions of each component, e.g. drift and diffusion of oxygen vacancies, and dc electronic conduction, to the total current density are, respectively, plotted. The solid and dashed lines denote positive and negative current density, respectively. The circles indicate transitions between ionic and electronic conduction. The voltages assigned to the left Helmholtz layer (cathode), the MIEC, and the right Helmholtz layer (anode) are plotted with respect to (c) the applied voltage and (d) time. (e) The calculated electron band profiles with time are shown.

Table 2.1 Parameters used in the J-V calculation

| $D_{Vo}$ [cm$^2$/s] | $\mu_{Vo}$ [a] [cm$^2$/V·s] | $d_1$ [nm] | $d_2$ [nm] | $d_3$ [nm] | $\varepsilon_{r1}$ [b] | $\varepsilon_{r2}$ [b] | $\varepsilon_{r3}$ [b] |
|---|---|---|---|---|---|---|---|
| $5\times10^{-13}$ | $1.93\times10^{-11}$ | 0.2 | 50 | 0.2 | 3.07 | 43.02 | 3.07 |

| $\phi_b$ [eV] | $m_e$ [kg] | $\rho$ [c] [cm$^{-2}$] | ESR [d] [ohms] | $z$ [e] | Temperature [K] |
|---|---|---|---|---|---|
| 1.7 | $9.11\text{x}10^{-31}$ | $4.5\times10^{13}$ | 10 | 2 | 300 |

[a]This quantity is reliant on the diffusion coefficient through the Einstein equation, $\mu_{V_O}=qD_{V_O}/k_BT$, where $k_B$ and $T$ denote the Boltzmann constant and temperature, respectively. [b]The relative permittivity values of these three layers were indeed evaluated from the overall relative permittivity of the capacitor, which was measured to be approximately 39. This value was obtained from the admittance spectra of the capacitors. The admittance spectra will be discussed in detail in Supplementary Information. [c]Areal density of oxygen vacancies. [d]Equivalent series resistance. [e]Charge number of an oxygen vacancy.

### 2.2.3. Faradaic type cell

Resistance switching behavior of the fabricated faradaic type cells was confirmed by current-voltage (I-V) measurements. Figure 2.7 shows the I-V measurement results of the three faradaic cells: CTP, NTP, and TTP. A set of ten consecutive triangle-shaped (stairwise increasing and decreasing) voltage pulses was applied at one polarity, followed by another set of ten consecutive triangle-shaped voltage pulses at the other polarity. Although the measured I-V loops are complicated, the three samples exhibit the common tendency that pulse-number-dependent increases in the read current, i.e. set switching, occur at negative voltage polarity whereas decreases in the current, i.e. reset switching, are observed at positive voltage polarity. It turned out that the measured I-V hysteresis represents the STM effect rather than the LTM effect since the history- or experience-dependent hysteretic loops were found to recover their initial hysteretic loop shape within a few seconds.

The I-V hysteretic loops were measured without electroforming. Thus, the current during the I-V measurements does not appear to flow through localized conduction pathways, i.e. conducting filaments, embedded in the insulating $TiO_2$ matrix. As a matter of fact, the I-V loops were found to scale with the TE area (data not shown here). As shown in Figure 2.7, the I-V loops significantly vary on the TE material. Considering that the same Pt BE and $TiO_2$ MIEC layers were used in the three different ECs, the significant difference is estimated to arise from the electrical and chemical properties of the TE materials and their interfaces. Detailed discussions will be given later.

The kinetics of resistance switching phenomena of the EC was identified by measuring the current response of the EC to well-designed voltage pulse trains. The voltage pulse trains consist of periodic square-shaped voltage pulses ($V_{ap}$), i.e. programming voltage pulses, and periodic square-shaped read-out voltage pulses ($V_r$) between the programming pulses. In the

measurements, the current level at the read-out voltage was taken as the read-out current ($I$). Read-out current changes ($\Delta I$) during voltage pulse train application were defined as the deviations of the read-out currents from the initially read-out current ($I_0$), i.e. $\Delta I_n = I_n - I_0$ and $n$ = 1, 2, 3, . . ., where $n$ denotes the number of read-out voltage pulses. Moreover, we define set switching and reset switching as the increase and the decrease of the read-out current, respectively.

Figure 2.8a shows set switching behaviors of the three ECs (CTP, NTP, and TTP), measured by applying voltage stimuli (90.9 Hz, Vap = −3 V, 40 stimuli) and reading currents ($V_r$ = −2.3, −0.8, and −0.7 V for CTP, NTP, and TTP, respectively). The different read-out voltages were employed because of the minimum detectable current of the oscilloscope. Also, the I-V relationship significantly depends on the TE material, as shown in Figure 2.7. For each EC, the periodic stimuli led to a gradual decrease in resistance. However, after the train of voltage stimuli terminated (the arrow in Figure 2.8a), the resistance underwent relaxation, as can be seen in Figure 2.8a. During this relaxation period, only read-out voltage pulses were applied to each EC to read the resistance relaxation. All ECs therefore represented the STM effect, rather than the LTM effect. As shown in Figure 2.8a, a read-out current change rate constant in set switching relies on the TE material. The reset switching behavior was also found to undergo relaxation, as shown in Figure 2.8b.

A set of external stimuli of positive polarity, following periodic negative polarity stimuli, was found to lead to gradual reset switching rather than additional set switching, as plotted in Figure 2.8c. The polarity alternation point is indicated by the arrow in Figure 2.8c. During the positive polarity stimulation, the read-out current gradually dropped below the initial read-out current, and thus the read-out current change ($\Delta I$) dropped below zero, implying reset switching. These measurement results justify the bipolar

resistive switching behavior of the ECs in the short-time period.

The aforementioned differences in SET switching behavior between the three ECs most likely arise from the effect of the interface between the TE and MIEC on electronic and/or ionic transport and the related electrochemical reactions. We can rule out the BE and the MIEC layer's bottom-interface and bulk as factors determining the SET switching difference, insomuch as they are barely influenced by the TE materials. Furthermore, electric-field-driven redistribution of self-dopants, i.e. probably oxygen vacancies[11-14] 'confined' within the $TiO_2$ MIEC, does not appear to explain the bipolar resistive switching behavior. That is, blocking interfaces sandwiching the oxygen-vacancy-including MIEC layer, i.e. a non-faradaic capacitor configuration, cannot account for the observed SET switching phenomena. Oxygen vacancies in the MIEC migrate (drift) depending on the electric field direction and are piled up at the cathode interface, leading to enhancement of electron injection through the cathode interface.[8, 15, 16] If this were the case, the polarity reversal would result in polarity-independent switching, i.e. unipolar switching. This is definitely inconsistent with the observations shown in Figure 2.7. The Pt BE can be regarded to be inert, such that it forms blocking contact for oxygen vacancies. Thus, it is perhaps reasonable to estimate the reactive TE to result in partially non-blocking contact, enabling oxygen-vacancy-related electrochemical reactions to be activated. Therefore, oxygen vacancies are not confined within the MIEC, so that their number varies according to the polarity of the applied electric field.

As shown in Figure 2.7, the RESET (SET) switching is caused by a positive (negative) voltage applied to the TE. Regarding the positive-voltage-induced RESET switching, anodizing the TE appears to increase the resistance. Anodizing the reactive TE may lead to oxidation of the electrode. Insomuch as the anodized metal is either insulating/semiconducting, or at least more resistive than the metal, due to an increase in the effective

thickness of the non-metallic layer, the oxidation most likely increases the resistance. A mechanism for metal anodization is thought to involve the following three processes: (i) oxidation of the metal (M), i.e. $M \rightarrow M^{z+} + ze^{-}$, (ii) drift of oxygen ions towards the anode, and (iii) oxide formation, i.e. $M^{z+} + z/2O^{2-} \rightarrow MO_{z/2}$.[17, 18] However, it should be noted that the measured reset switching may lack the third process, resulting in the formation of energetically stable oxide phases. This estimation is quite obvious, taking into account the synaptic weight relaxation, i.e. the STM effect. If stable oxide phases were formed, no relaxation would proceed, i.e. the LTM effect, when the external stimulation is removed.

As Jeong et al have pointed out, the STM effect in nanoionic systems can be understood in terms of detailed balance between paired electrochemical reactions, i.e. forward and backward reactions.[7] In a nanoionic system without a sink of active ions/defects, a reaction driven by an external stimulus is thought to trigger the evolution of the restoring force, serving as a driving force of the paired backward reaction. When the stimulus terminates, the backward reaction prevails over the forward reaction, recovering the initial configuration of ions/defects, i.e. relaxation. However, if an energetically stable sink of ions/defects is evolved as a result of a third reaction, e.g. the third process in metal anodization, independent of the paired reactions satisfying the detailed balance, LTM can be achieved; i.e. relaxation can be avoided.[7, 19, 20]

A mechanism for potentiation can be guessed as the reversal of the aforementioned RESET switching mechanism. With negative voltage application, an overpotential for the metal oxidation is probably negative so that metal ions are reduced. This reduction may cause a decrease in the effective thickness of the interfacial non-metallic layer, i.e. an increase in the thickness of the TE layer, and the consequent decrease of resistance. It is probable that there is an equilibrium concentration of the metal ions at the

ground state (no external stimulation). The equilibrium concentration may be determined by the Galvani potential distribution through the EC junction, where the overpotential for the metal redox reaction and the equilibrium concentration are self-consistent.[8] A decrease in metal ion concentration arising from the application of a negative stimulus therefore leads to the evolution of a restoring force and, when the stimulus terminates, the junction recovers the basal level of metal ion concentration, i.e. equilibrium concentration. That is, relaxation of resistance occurs.

One may guess that the oxygen ion drift towards the anode, involved in the metal anodization, results in the top-electrode-dependent STM effect. As Yang et al have indicated, the oxygen vacancy concentration in $TiO_2$ MIEC may vary in TE materials.[10] However, we should concern ourselves with oxygen ions rather than vacancies, since they are the species involved in anodization. Insomuch as the concentration of possibly included oxygen vacancies is much lower than the oxygen ion concentration in $TiO_2$, e.g. $6.4 \times 10^{22}$ $cm^{-3}$ in single crystalline rutile $TiO_2$, the oxygen ion concentration barely depends on TE. Therefore, the oxygen ion drift towards the anode may not play an important role in the top-electrode-dependent STM effect.

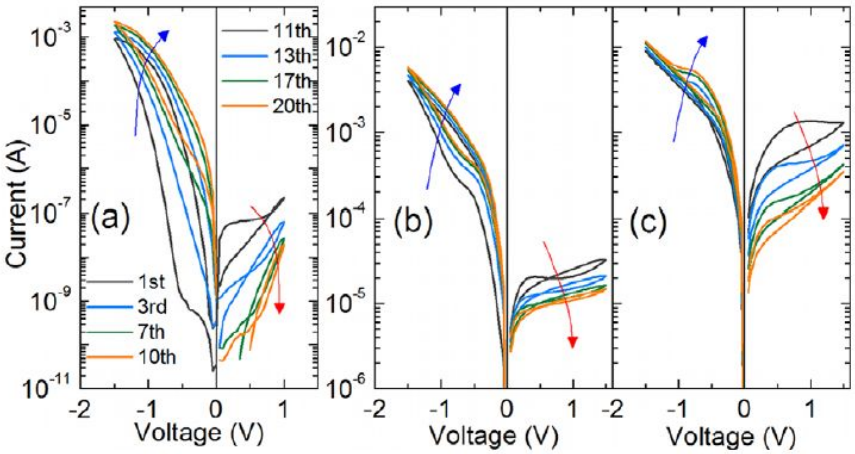


Figure 2.7 Consecutively measured I-V loops of the (a) CTP, (b) NTP, and (c) CTP. For each EC, the first ten loops were measured by applying triangle-shaped negative voltage pulses and the next ten loops by positive voltage pulses. The arrows indicate the tendencies of the loop shift with consecutive voltage application.

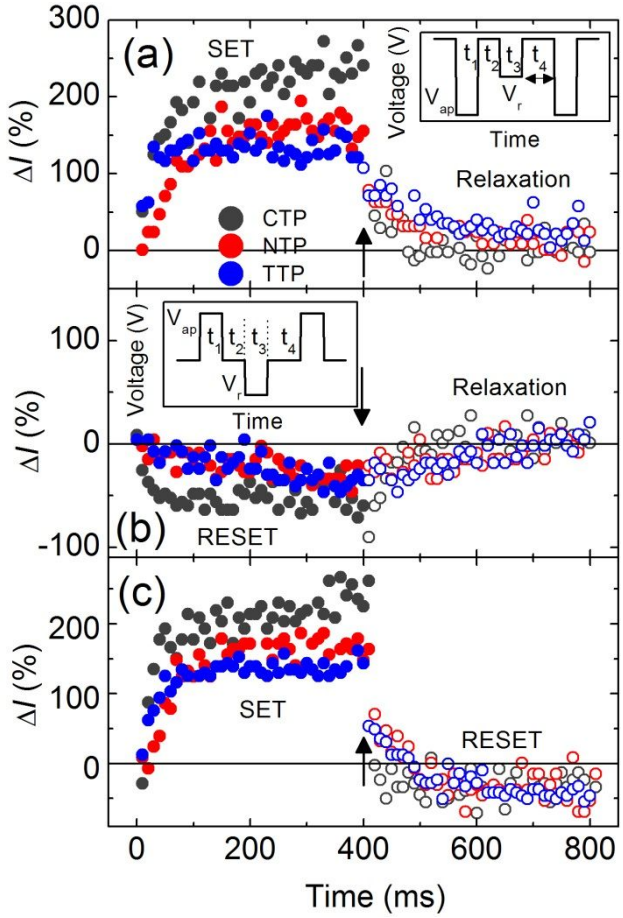


Figure 2.8 (a) SET behavior of the three ECs (CTP, NTP, and TTP) arising from external voltage stimuli (90.9 Hz, $V_{ap}$ = −3 V, 40 stimuli), applied up to the time indicated by the arrow, and the following relaxation of the synaptic weight. The read-out voltages for CTP, NTP, and TTP were −2.3, −0.8, and −0.7 V, respectively. The voltage stimuli are shown in the inset. The widths of both $V_{ap}$ and $V_r$, $t_1$ and $t_3$, respectively, were 1 ms. The time intervals between

$V_{ap}$ and $V_r$ ($t_2$) and between $V_r$ and the next $V_{ap}$ ($t_4$) were 2 and 7 ms, respectively. Thus, the stimulation frequency was $\left(\sum_{i=1}^{4} t_i\right)^{-1}$. (b) RESET and relaxation behaviors were also identified by applying voltage stimuli (90.9 Hz, $V_{ap}$ = 2 V, 40 stimuli) up to the time indicated by the arrow. (c) Transition from SET to RESET of resistance change, arising from the polarity alteration of external stimuli ($-V$ to $+V$).

## 2.3. Threshold switch based on GeSe

### 2.3.1. Experimental

***GeSe thin film deposition***: An amorphous GeSe layer was deposited by rf magnetron co-sputtering method. (deposition rate:12.2 nm/min) The rf-power of $Ge_4Se_6$ and Ge target, and working pressure under Ar atmosphere were maintained as 30 W, 20 W, and 0.5 mTorr, respectively during the deposition. The crystallization temperature was determined by the X-ray diffraction analysis of the annealed GeSe film as shown in Figure 2.9.[21]

***Threhold switch fabrication***: TS cells were formed in crossbar structure (see Figure 2.10) realized by following steps. i) The Pt BE was deposited on Ti adhesion layer by electron-beam evaporation and patterned using a standard photolithography technique. (photoresist: AZ5214, aligner: Karl Suss MA6) ii) The 100 nm GeSe layer was deposited onto the BE by rf magnetron co-sputtering method. iii) For the singl-layered TS, the Pt TE was deposited onto the GeSe layer by electron-beam evaporation and patterned in the same method for the BE. For the dual-layerd TS, the 20 nm $SiO_x$ (SO) layer was deposited onto the GeSe layer before the TE depostion. Then, the Cu TE was deposited onto the SO layer by electron-beam evaporation and patterend in the same method for the BE. The cross-point areas were set to 5×5 $\mu m^2$ for single-layered TS cells, whereas were set to varied from 5×5 to 50×50 $\mu m^2$ for dual-layered TS cells.

***Current-voltage measurments***: Two types of I-V measurements were conducted. i) I-V measurements on the dual-layered TS cells (Cu/SO/GeSe/Pt) were conducted by using a Keithley 236 Source Measurement Unit. ii) I-V behavior of the single-layered TS (Pt/GeSe/Pt) was measured by applying a

triangle voltage pulse using an Agilent 81110A pulse generator (PG). The response was simultaneously recorded by using a Tektronix TDS5104 oscilloscope. The measured I-V behavior revealed $V_{on}$, $V_{off}$, and $R_{on}$ other than $R_{off}$ that was barely readable due to the limited voltage resolution of the oscilloscope. The sub-threshold behavior including $R_{off}$ was alternatively evaluated by employing a Keithley 236 Source Measurement Unit. A voltage was applied to the TE while the BE was grounded for three cases.

***Potentiostatic measurements***: The voltage pulses were generated using an Agilent 81110A and applied to the BE of the cells. The responses of the cells to the voltage pulses were monitored using a Tektronix TDS 5104 oscilloscope having an internal resistance of 50 ohms.

***XPS characterization***: For the XPS characterization an additional type of cell was fabricated: unpatterned blanket Cu layer on blanket SO-GeSe dual-layer solide electrolytes that were formed on blanket Pt BE layers. The aforementioned cell was used for the XPS characterization. For evaluation of depth profile of each element the specimen was sputtered using Ar ions at 3 kV.

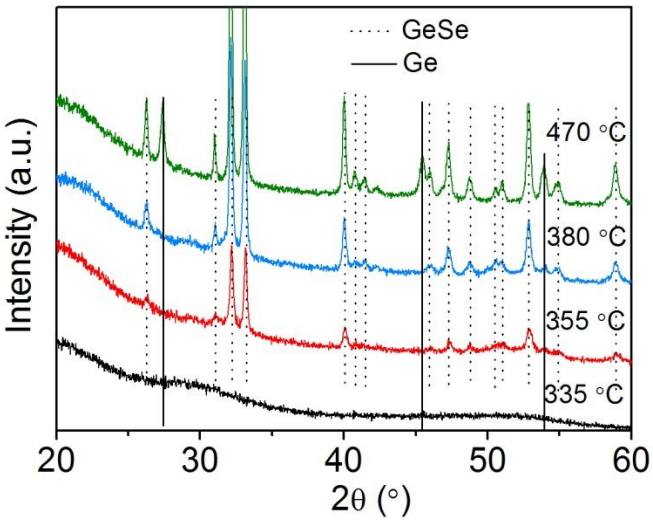


Figure 2.9 X-ray diffraction analysis of the annealed GeSe thin fim. The dot line and solid line indicate crystalline GeSe and Ge, respectively.[21]

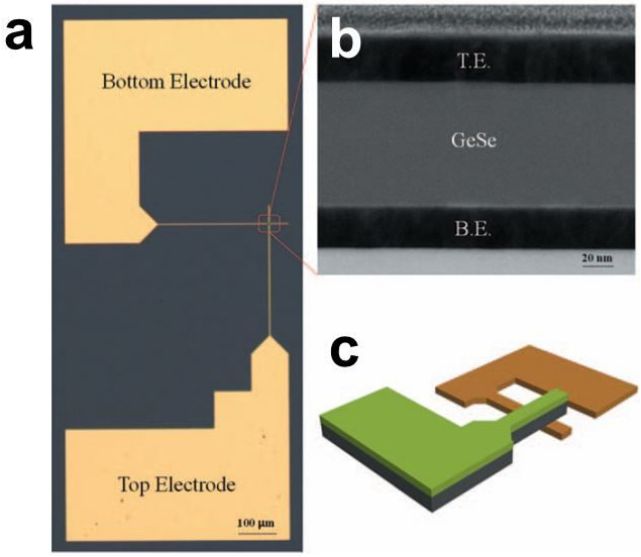


Figure 2.10 (a) The optical image of the fabricated crossbar-structred TS cell from top view. (b) A cross-sectional transmission electron microscope image of the single-layered TS (Pt/GeSe/Pt) cell. (c) A schematic of the TS crossbar structure.[5]

### 2.3.2. Threshold switch exhibiting s-shaped negative differential resistance

The Pt/GeSe/Pt TS is known to represent resistive switching of monostability – popularly referred to as threshold switching.[5, 6] The threshold switching differs from bistable resistive switching (memory switching) in light of lack of stability for the excited state (on-state) – featuring low resistance generally – without external perturbation.[4-6, 22] Typical I-V hysteretic loops of the TS are plotted in Figure 2.11a, which were measured by applying a triangular voltage pulse $V_{in}$ (shown in the inset of Figure 2.11a) to the circuit in Figure 2.11b. $V_{out}$ in Figure 2.11b was directly acquired from the oscilloscope. Given a known resistor $R_{load}$, the voltage across the TS ($V_{TS}$) was obtained, providing the I-V hysteretic loops in Figure 2.11a.

The characteristic threshold switching behavior can by and large be parameterized by four switching parameters: $R_{off}$, $R_{on}$, $V_{off}$, and $V_{on}$ denoting off- and on- resistance and threshold voltages for on-to-off and off-to-on switching, respectively.[5] The on-switching is known to be accompanied with s-shaped NDR.[22] s-shaped NDR following threshold switching has been observed in not only amorphous higher chalcogenides[4-6] but also various systems such as Mott insulators,[23, 24] open-base bipolar junctions,[25] Shockley diodes.[26, 27] The amorphous GeSe in the TS is an As-free chalcogenide material whose detail in film deposition can be seen elsewhere.[5] The s-shaped NDR that causes the on-state drives large current flow, and thus high power dissipation (Joule heat). Fortunately, the crystallization temperature of GeSe is fairly high (~350 ℃) so that the memory switching − arising from phase-change − could be prevented.[6] A mechanism for threshold switching in amorphous chalcogenide is still controversial between two plausible models: the thermal model[28, 29] and

purely electronic model.[30-32] The former elucidates the thermal activation of electronic carriers in the chalcogenide in which the number of electrons exponentially varies upon the lattice temperature.[28, 29] The purely electronic model such as double injection model[30, 31] a priori rules out such thermal activation and, instead, concerns the electric field re-distribution and resulting change in the band structure within the chalcogenide. In the double injection model, the electric field re-distribution is mediated by the time-dependent interaction between electronic carriers and charge traps.[30, 31]

Variability in the threshold switching parameters was unavoidable as for resistive switching devices.[33, 34] As seen in Figure 2.11c – e, there exist remarkable distributions of $V_{on}$, $V_{off}$, and $R_{off}$, which by and large follow a normal distribution. The data fitting reveals standard deviations of 7, 5, and 5% for $V_{on}$, $V_{off}$, and $R_{off}$, respectively. Variability in $R_{on}$ could not be evaluated in view of the difficulty in the parameter evaluation, though it is most likely present (see Experimental). These variations were seen after each switching cycle, and thus most likely driven by each switching-cycle.

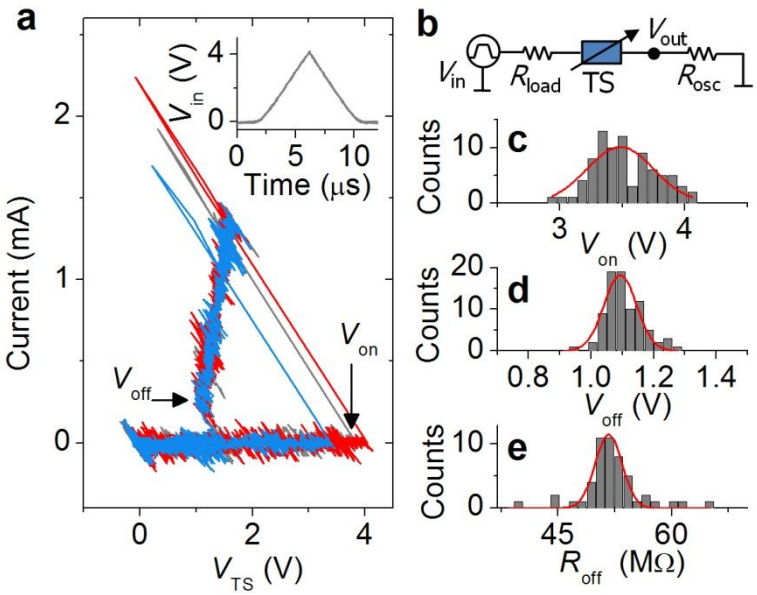


Figure 2.11 (a) Threshold switching *I-V* loops of the TS in the circuit configuration in (b). The inset in a) shows the applied triangular voltage pulse. Variability in threshold switching parameters, (c) $V_{on}$, (d) $V_{off}$, and (e) $R_{off}$, is shown in the histrogram. $R_{off}$ was measured at a $V_{TS}$ of 0.5 V.

### 2.3.3. Threshold switch without s-shaped negative differential resistance

The behavior of dual-layered TS cells, (or could be referred to as electrochemical metallization (ECM) cells) under negative voltage with a compliance current is examined. The negative voltage application in a quasi-static voltage sweep mode with a compliance current leads to monostable resistive switching behavior, which is popularly referred to as threshold switching, as can be seen in Figure 2.12a. Here, the bias was applied to Cu TE while the Pt BE was grounded. This is a somewhat surprising result considering the fact that a typical memory switching could be generally achieved when the Cu electrode was positively biased, and the threshold-type switching would be expected when a limited switching power was applied by adopting a low level of compliance current. Threshold switching is of volatility rather than non-volatility, that is, it does not represent memory effect. In Figire 2.9a, a sudden increase in current at approximately -0.9 V is noticed, reaching the compliance current (50 μA). This voltage is defined as on-switching voltage ($V_{on}$). While the down sweep towards zero voltage, current starts dropping at approximately -0.25 V and the cell eventually recovers its original, i.e. pristine, resistance. This voltage is defined as off-switching voltage ($V_{off}$). This threshold switching behavior is quite stable. However, there are distributions of switching parameters, e.g. $V_{on}$, $V_{off}$, and the resistances in the on- and the off-state, $R_{on}$ and $R_{off}$, respectively, as shown in Figures. 2.12b and 2.12c, respectively, during the repeated I-V sweeps.

The threshold switching behavior was double-checked by employing a potentiostatic measurement method (voltage pulse application). Here, the bias was applied to Pt BE while the Cu TE was grounded. A schematic of the measurement setup is illustrated in Figure 2.13c. The detail of the setup can be seen found elsewhere.[6] While application of the voltage pulses shown in

Figure 2.13b, the ECM cell underwent the threshold switching in case that the applied voltage was larger than a threshold voltage for the threshold switching (red line in Figure 2.13a).

The threshold switching kinetics was identified by monitoring the response of the maximum current flowing through the ECM cell to the applied voltage pulses of different heights and widths. A current map with respect to voltage height and width is shown in Figure 2.13d. It is noticed that turning on the switch requires a certain time, i.e. incubation time denoted in Figure 2.13a, and a certain voltage, which are not independent of each other. The higher the applied voltage pulse height, the smaller the pulse width is to obtain the similar amount of current. This relationship can be obviously seen in that between the incubation time and voltage pulse height as plotted on the current map using open circles in Figure 2.13d. The incubation time largely relies on the voltage pulse height, in particular, at lower heights (ca. < 1.7 V) whereas very weak dependence is shown at the high heights, e.g. 1.8 and 1.9 V. Thus, a transition of threshold switching mechanism with respect to the voltage height tends appears to occur in a similar way as shown in the on-switching kinetics of ECM memory cells.[35] A note should be placed on the fact that the off-switching is not accompanied with s-shaped NDR. During off-switching period in Figure 2.12a, resistance of the ECM cell is not abruptly but gradually recovered back to $R_{off}$. Regarding the quasi-static I-V measuremnt, it is plausible that multiple resistance states could be existed between $R_{on}$ and $R_{off}$ during off-switching.

The overall current conduction through the cell is found to be non-uniform over the electrode area, regardless of the cell's resistance state. The current barely scales with the electrode area in both on- and off-states as plotted in Figure 2.13e. The off-state currents were evaluated from the quasi-static I-V measurements and the on-state currents from the potentiostatic voltage pulse measurements. This most likely implies that current paths, having non-

uniform distribution over the electrode area, were inherently embedded in the solid electrolyte in the pristine state. Note that these current paths do not necessarily mean conducting filaments as the term includes all factors that possibly lead to the non-uniform conductance distribution. The current paths perhaps result from spontaneous Cu ion migration through the dual-layer solid electrolyte, which was indeed identified in SO-based ECM cells.[36, 37]

The XPS measurement was performed on a large blanket specimen. This specimen was also placed in deionized water before the XPS measurements to impose the same condition. The measured spectra are shown in Figure 2.14. Given the high signal-to-noise ratio, the valence state of Cu in the GeSe layer could be identified; it turned out to be $Cu^0$. That is, Cu stays neutral in the GeSe layer, whereas Cu in the SO layer in this blanket specimen is ionized. Given the measured XPS spectrum, the valence state of incorporated Cu in the pristine ECM cell is estimated to be twofold: neutral $Cu^0$ and in the lower GeSe and $Cu^{2+}$ in the upper SO. The standard chemical potential of Cu in SO is predicted to be lower than that in GeSe due to the higher Cu-O bonding energy than Cu-Se.[38] Thus, the SO layer perhaps serves as a chemical potential well for Cu, confining incorporated Cu atoms/ions in the well. Moreover, a much larger difference in electronegativity between Cu and O than that between Cu and Se leads to the stronger ionic bonding character of Cu-O than Cu-Se. Accordingly, the difference in the Cu valence state between SO and GeSe can be understood.

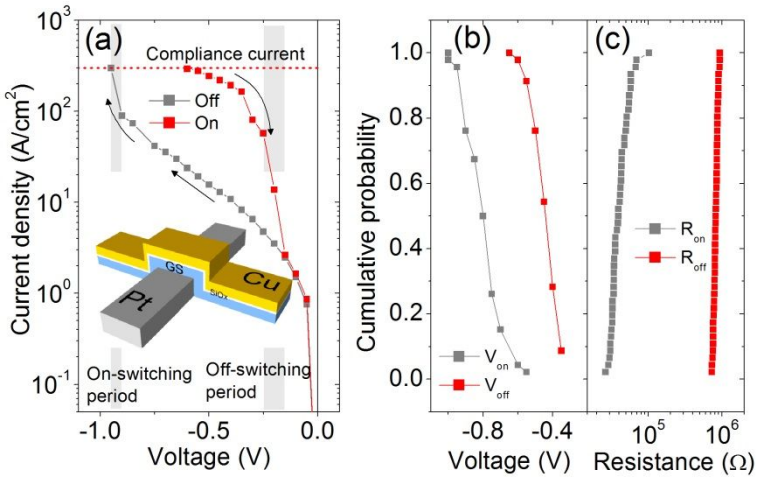


Figure 2.12 Threshold switching behavior of the ECM cell. (a) Typical I-V curve representing the threshold switching behavior. A schematic of the TS is drawn in the inset. Statistic data of switching parameters such as (b) $V_{on}$, $V_{off}$, (c) $R_{on}$, and $R_{off}$. $R_{off}$ was evaluated at a read-out voltage of -0.1 V in the upwards sweep, i.e. towards the maximum whereas $R_{on}$ at $V_{off}$-0.1 V due to the variation of $V_{off}$ a constant read-out voltage could not be used.

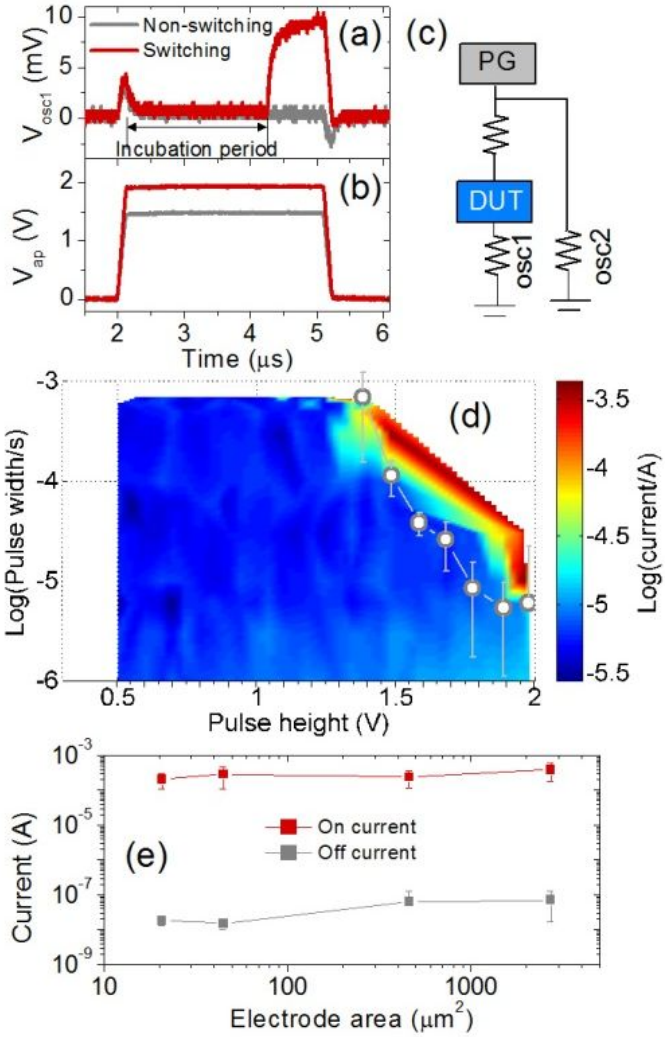


Figure 2.13 Response of the threshold switch to voltage pulses. (a) Threshold switching response of the ECM TS to (b) applied voltage pulses. The measurements were conducted using a setup whose schematic is illustrated in (c). PG, DUT, osc1, and osc2 denote the pulse generator, device

under test, oscilloscope channels whose internal resistance is 50 ohms, respectively. The incubation time indicated in a) means a time required to turn on the switch. (d) A current map of the same switch, measured by applying voltage pulses of different widths and heights. The average incubation times under the various pulse heights are denoted by the circle symbols on the current map. (e) The currents in the off-state (at a read-out quasi-static voltage of -0.1 V) and the on-state (obtained from the current response to the voltage pulse) are plotted with respect to the electrode area.

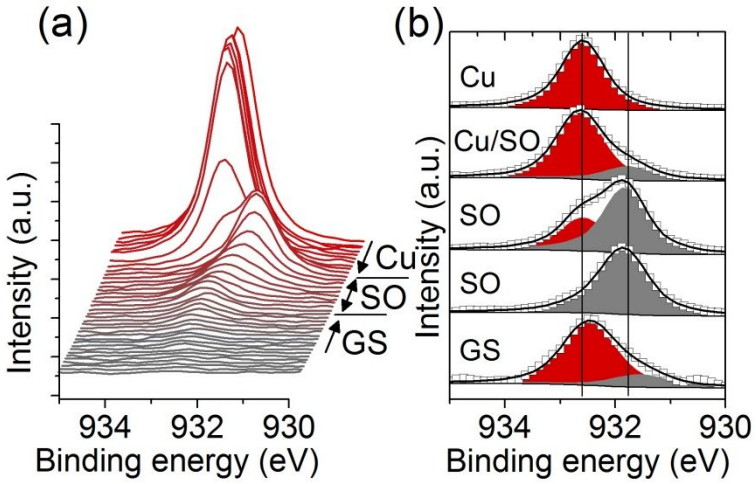


Figure 2.14 (a) Photoelectron spectra of Cu $2p_{3/2}$ emission at given depths from the top Cu layer surface in the blanket structure. (b) Several sampled spectra at each layer. (GS short for GeSe)

## 2.4. Conclusions

J-V behaviors of pristine Pt/$TiO_2$/Pt non-faradaic capacitors were characterized; complex and dynamic hysteretic behaviors were found. The complex hysteresis represented a transition of electric conduction. By means of time-dependent defect migration calculations, the transition was found to be attributed to a transition between ionic and electronic conduction behaviors. The electronic conduction is much more sensitive to an applied voltage than the ionic conduction so that, after transition into the electronic conduction regime, the non-faradaic capacitor shows a drastic increase in current with the voltage. Given that this transition is caused by oxygen vacancy migration kinetics, i.e. dynamics, a threshold voltage for the transition depends not only on input voltage pulse height but also on its pulse width.

Provided the both polarity-dependent SET and RESET phenomena and reactive TE (no Pt TE) of ECs, it is most likely that redox reaction at the interface between the TE and the MIEC layer might be the major resistive switching mechanism of ECs. At present, the role of the interface between the TE and the MIEC layer in electronic transport is not clear. We will leave this relationship as an open question.

Both GeSe-based single- and dual-layered TSs exhibited monostable switching. One of the distinct phenomenological switching characteristics between two TSs was s-shaped NDR, which was clearly demonstrated in Pt/GeSe/Pt TS. (see Figure 2.10) Provided the quasi-static measurement in Figure 2.11, however, off-switching period of Cu/SO/GeSe/Pt was unlikely accompanied with s-shaped NDR. Later on, s-shaped NDR will be revisited when TS is embedded in the oscillatory circuit is Section 6.3.2.

## 2.5. Bibliography


[1] R. Waser, M. Aono, *Nat. Mater.*, 6, 833 (2007).

[2] R. Waser, R. Dittmann, G. Staikov, K. Szot, *Adv. Mater.*, 21, 2632 (2009).

[3] G. H. Kim, J. H. Lee, Y. Ahn, W. Jeon, S. J. Song, J. Y. Seok, J. H. Yoon, K. J. Yoon, T. J. Park, C. S. Hwang, *Adv. Funct. Mat.*, 23, 1440 (2013).

[4] M. J. Lee, D. Lee, S. H. Cho, J. H. Hur, S. M. Lee, D. H. Seo, D. S. Kim, M. S. Yang, S. Lee, E. Hwang, M. R. Uddin, H. Kim, U. I. Chung, Y. Park, I. K. Yoo, *Nat. Commun.*, 4, 2629 (2013).

[5] H.-W. Ahn, D. S. Jeong, B.-k. Cheong, S.-d. Kim, S.-Y. Shin, H. Lim, D. Kim, S. Lee, *ECS Solid State Lett.*, 2, N31 (2013).

[6] D. S. Jeong, H. Lim, G.-H. Park, C. S. Hwang, S. Lee, B.-k. Cheong, *J. Appl. Phys.*, 111, 102807 (2012).

[7] D. S. Jeong, I. Kim, M. Ziegler, H. Kohlstedt, *RSC Adv.*, 3, 3169 (2012).

[8] D. S. Jeong, H. Schroeder, R. Waser, *Phys. Rev. B*, 79, 195317 (2009).

[9] H. Wang, L. Pilon, *Electrochim. Acta*, 64, 130 (2012).

[10] J. J. Yang, J. Strachan, F. Miao, M.-X. Zhang, M. Pickett, W. Yi, D. A. Ohlberg, G. Medeiros-Ribeiro, R. S. Williams, *Appl. Phys. A*, 102, 785 (2011).

[11] U. Balachandran, N. G. Eror, *J. Mater. Sci.*, 23, 2676 (1988).

[12] P. Kofstad, *J. Phys. Chem. Solids*, 23, 1579 (1962).

[13] J.-F. Marucco, J. Gautron, P. Lemasson, *J. Phys. Chem. Solids*, 42, 363 (1981).

[14] C. Meis, J. L. Fleche, *Solid State Ionics*, 101–103, Part 1, 333 (1997).

[15] D. S. Jeong, R. Thomas, R. S. Katiyar, J. F. Scott, H. Kohlstedt, A.

Petraru, C. S. Hwang, *Rep. Prog. Phys.*, 75, 076502 (2012).

[16] A. Sawa, *Mater. Today*, 11, 28 (2008).

[17] N. Cabrera, N. F. Mott, *Rep. Prog. Phys.*, 12, 163 (1949).

[18] N. F. Mott, *Trans. Faraday Soc.*, 35, 472 (1940).

[19] T. Chang, S.-H. Jo, W. Lu, *ACS Nano*, 5, 7669 (2011).

[20] T. Ohno, T. Hasegawa, T. Tsuruoka, K. Terabe, J. K. Gimzewski, M. Aono, *Nat. Mater.*, 10, 591 (2011).

[21] H.-W. Ahn, Ph.D. dissertation, *A study of the materials and device characteristics of Ge-doped Sb-Te and Ge-Se chalcogenides for high density phase change memory*, Korea University, 2014.

[22] M. D. Pickett, R. S. Williams, *Nanotechnology*, 23, 215202 (2012).

[23] A. Crunteanu, J. Givernaud, J. Leroy, D. Mardivirin, C. Champeaux, J. C. Orlianges, A. Catherinot, P. Blondy, *Sci. Technol. Adv. Mat.*, 11, 065002 (2010).

[24] M. D. Pickett, G. Medeiros-Ribeiro, R. S. Williams, *Nat. Mater.*, 12, 114 (2012).

[25] J. W. Han, Y. K. Choi, *Symp. VLSI Technol., Dig. Tech. Pap.*, 171 (2010).

[26] X. Tong, J. Luo, H. Wu, Q. Liang, H. Zhong, H. Zhu, C. Zhao, *J. Vac. Sci. Technol. B*, 32, 021205 (2014).

[27] X. Tong, H. Wu, L. Zhao, H. Zhong, *ECS Trans.*, 52, 105 (2013).

[28] D. M. Kroll, M. H. Cohen, *J. Non-Cryst. Solids*, 8–10, 544 (1972).

[29] C. Popescu, *Solid-State Electron.*, 18, 671 (1975).

[30] H. K. Henisch, E. A. Fagen, S. R. Ovshinsky, *J. Non-Cryst. Solids*, 4, 538 (1970).

[31] N. F. Mott, *Contemp. Phys.*, 10, 125 (1969).

[32] A. Pirovano, A. L. Lacaita, F. Pellizzer, S. A. Kostylev, A. Benvenuti, R. Bez, *IEEE Trans. Electron Devices*, 51, 714 (2004).

[33] S. B. Long, X. J. Lian, T. C. Ye, C. Cagli, L. Perniola, E. Miranda,

M. Liu, J. Sune, *IEEE Electron Device Lett.*, 34, 623 (2013).

[34] J. H. Yoon, S. J. Song, I.-H. Yoo, J. Y. Seok, K. J. Yoon, D. E. Kwon, T. H. Park, C. S. Hwang, *Adv. Funct. Mater.*, 24, 5086 (2014).

[35] S. Menzel, S. Tappertzhofen, R. Waser, I. Valov, *Phys. Chem. Chem. Phys.*, 15, 6945 (2013).

[36] D.-Y. Cho, S. Tappertzhofen, R. Waser, I. Valov, *Nanoscale*, 5, 1781 (2013).

[37] S. Tappertzhofen, I. Valov, T. Tsuruoka, T. Hasegawa, R. Waser, M. Aono, *ACS Nano*, 7, 6396 (2013).

[38] R. Soni, P. Meuffels, A. Petraru, M. Hansen, M. Ziegler, O. Vavra, H. Kohlstedt, D. S. Jeong, *Nanoscale*, 5, 12598 (2013).

# 3. Artificial synapse

## 3.1. Introduction

Often, mammalian brains are compared with central processing units (CPUs) when the role of the brain is simply explained. Similar to CPUs, mammalian brains are able to carry out deterministic calculations, i.e. solving problems having fixed solutions. In these calculations, CPUs are much more reliable than brains in terms of speed, accuracy, and the scale of calculation. However, the function of mammalian brains that differentiates them from CPUs is 'learning'. Brains are able to learn, so that they can solve problems having unfixed solutions, i.e. nondeterministic calculations. This fascinating functionality is a subject that a number of non-biology researchers (electrical engineers, computer scientists, materials scientists, etc) have attempted to emulate by means of non-biological systems. This research field is referred to as neuromorphic engineering, coined by Mead.[1] The hippocampus of a mammalian brain is known to be responsible for learning and memory. The basic building blocks of the hippocampus are the neuron and the synapse (chemical synapse).

To realize the ambitious goal of neuromorphic engineering, it is necessary to build up complex ANNs using the basic building blocks, i.e. artificial neurons and synapses. As mentioned above, the higher-level functionalities of the hippocampus, e.g. learning and memory, must be understood at the network (collective) level rather than at the building block level. Nevertheless, considering that the collective behavior reflects a single building block's behavior, it is of great importance to successfully realize artificial synapses and neurons that meet the requirements as building blocks of complex neural networks. In particular, learning and memory directly

involve the activity-dependent plasticity of chemical synapses, and thus particular emphasis needs to be placed on the achievement of artificial synapses. Recently, a number of attempts have been made to realize artificial synapses by means of various physical concepts.[2]

In this study, we demonstrated the STM effect of two-terminal passive VCM systems utilizing $TiO_2$ MIEC, which is well known as a typical VCM material.[3] In fact, $TiO_2$ has attracted considerable attention for its application in resistive switching RAMs and memristors.[4-7] Note that the STM effect differs from the resistive switching effect representing LTM. The difference most likely arises from electroforming. In the STM effect measurements, electroforming procedures were not employed. Moreover, different 'reactive' metals such as Cr, Ni, Ti, rather than inert metals such as Pt, Au, were used as TEs to identify the dependence of STM effects on the reactive electrode. Note that, hereafter, conductance of ECs is termed as a synaptic weight, $w$. Likewise, read-out current change, i.e. $\Delta I$ of Figure. 2.7, can be termed as $\Delta w$. Finally, the observed STP behavior was described by a mathematical formula. By comparing the equation and experimental data, critical parameters determining the STP behavior were extracted, and a relationship between the parameters and electrode materials was addressed.

## 3.2. Results and discussions

When potentiated, the synaptic weight change did not show unlimited growth. Instead, it converged towards a certain value, as shown in Figures 3.1a and c. The Hebb rule is described by $\tau_w \, d\Delta w/dt = u_{pre} u_{post}$, where $w$, $u_{pre}$, and $u_{post}$ denote a time constant of potentiation, presynaptic activity, and postsynaptic activity, respectively. According to the Hebb rule, sustained activities on both sides of a synapse lead to the unlimited increase of the synaptic weight with time. Thus, the Hebb rule cannot directly be employed to

describe the measurement results. Not only these artificial synapses but also biological synapses are known to behave differently from the Hebb rule when potentiated.[8, 9] That is, similar to the EC artificial synapses, biological synapses represent the saturation of their synaptic weight. Several mathematical formulae have been suggested to take into account the synaptic weight convergence (saturation), e.g. the Bienenstock–Cooper–Munro (BCM) rule[8] and the Oja rule.[9]

The stimulation frequency is regarded as a crucial variable in synaptic plasticity. For instance, Dudek and Bear reported stimulation-frequency-dependent plasticity of synapses in the CA1 of the hippocampus.[10] In their study, it was found that there is a threshold frequency for potentiation; i.e. the stimulation frequency should be larger than the threshold for potentiation, otherwise the stimuli lead to depression instead of potentiation. It is therefore worth checking the effects of the stimulation frequency on the STM behavior of the ECs. We varied the stimulation frequency from 9.9 to 90.9 Hz at a fixed stimulation voltage. The frequency was varied by changing the time interval between a read-out voltage pulse and the next voltage stimulus, i.e. $t_4$ as shown in the insets of Figure 2.7. The intervals for 90.9, 66.7, 47.6, 30.3, and 9.9 Hz were 7, 11, 17, 29, and 97 ms, respectively. This stimulation-frequency-dependent potentiation behavior was measured on the three ECs and the results are plotted in Figure 3.1. It can be seen that the potentiation behavior relies significantly on the stimulation frequency and the synaptic weight change increases as increasing frequency. Apart from CTP, the potentiation behaviors of the other ECs exhibited synaptic weight convergence towards certain levels during the stimulation (220, 160, 115, 75, and 25 stimuli at 90.9, 66.7, 47.6, 30.3, and 9.9 Hz, respectively). Thus, the basic Hebb rule, predicting uncontrolled growth of synaptic weight, cannot be employed to describe the potentiation behavior without taking into account the stimulation frequency.

The synaptic weight of each EC, averaged over the time period (2 ± 0.1 s), are plotted with respect to stimulation frequency in Figure 3.1d. In Figure 3.1d, in not only the time domain but also in the frequency domain, the potentiation behaviors of NTP and TTP tend to converge towards high-frequency limit values. That is, saturation of synaptic weight of these capacitors appears to occur at higher frequencies. However, in the case of CTP, the synaptic weight hardly exhibits a tendency to saturation, at least at the given frequencies. Instead, the synaptic weight at the highest frequency (90.9 Hz) is significantly larger than the other weight values. Considering that synaptic weight saturation most likely implies no further learning and memory, it is perhaps favored to widen the stimulation frequency range where synaptic weight saturation does not show up. Thus, the larger range of stimulation frequency perhaps enables the artificial synapses to realize a high degree of potentiation at various frequencies, as shown in CTP. In fact, repeated tetanization in the hippocampus of a mouse was found to lead to saturation of the synaptic weight of hippocampal synapses, and thus no new encoding of spatial information, which results in blocking the mouse's spatial learning.[11, 12]

It is worth deriving an empirical equation describing the potentiation behavior of the EC artificial synapses by which the top-electrode-dependent potentiation behaviors can be parameterized. A comparison between the three different ECs can therefore be made more easily. The synaptic weight change of the EC artificial synapses may be viewed as a continuous transition between fully potentiated and ground states. The fully potentiated state was regarded as being reached when the EC's synaptic weight reaches its maximum ($w_{max}$), as shown in Figure 3.2. That is, saturation, rather than unlimited growth, of synaptic weight was basically assumed, which is realistic, considering biological synapses' potentiation behavior as discussed earlier. At a given time, the synaptic weight value $w$ lies between $w_0$ and $w_{max}$,

corresponding to the ground state and the fully potentiated state, respectively. For simplicity, the relative synaptic weight $\Delta w$, $\Delta w = w - w_0$, can be defined, and thus the value lies between 0 and $\Delta w_{max}$ ($\Delta w_{max} = w_0$). It is perhaps proper to employ a time-dependent state variable ($\theta_t$) that determines the kinetics of synaptic weight change. Let us suppose that the time-derivative of the synaptic weight change is proportional to the difference between the strength of dthe external stimulus ($v$) and the state variable ($\theta_t$), i.e.

$$\frac{d\Delta w}{dt} = k(v - \theta_t), \tag{3.1}$$

where $k$ is a positive constant. In deriving the empirical equation, a firing-rate model, rather than a spiking model, was employed for simplicity.[13] The external stimulus strength $v$ is therefore given by a firing rate, i.e. stimulation frequency. When the time-varying state variable $\theta_t$ becomes close to, but still below, the stimulus strength $v$, the rate of synaptic weight change decreases with time and a rate of zero is eventually achieved if $\theta_t$ reaches $v$.

Equation 3.1 is basically borrowed from the BCM rule that was briefly discussed earlier. In the BCM rule, the state variable $\theta_t$ is referred to as a sliding threshold for potentiation.[8] The difference is that the BCM rule describes LTP, so that $\theta_t$ is a sliding threshold for LTP, whereas Equation 3.1 deals with STP, thus its threshold is for STP. The sliding threshold is assumed to be given by the logisticdifferential equation:

$$\frac{d\theta_t}{dt} = a\theta_t(b - \theta_t), \tag{3.2}$$

where $a$ and $b$ denote positive constants. The logistic function as a solution to the logistic differential equation accounts for the behavior of $\theta_t$ in the time domain, initially the rate of $\theta_t$ change is zero and increases, and thus $\theta_t$ increases, until $\theta_t$ reaches $b$. That is, $\theta_t$ converges towards $b$. The solution of Equation 3.2 is expressed as

$$\theta_t = \frac{1}{1+ce^{-t/\tau_\theta}}, \tag{3.3}$$

where $c = [b-\theta_t(0)]/\theta_t(0)$ and $\tau_\theta = (ab)^{-1}$. $\theta_t(0)$ means the initial value of the sliding threshold. The smaller the constant $\tau_\theta$ is, the steeper the threshold change is.

Substituting Equation 3.2 into Equation 3.1 and solving the first-order differential equations gives

$$\Delta w = k\left\{vt + b\tau_\theta \ln\left[\frac{e^{-t/\tau_\theta}(c+1)}{ce^{-t/\tau_\theta}+1}\right]\right\}. \tag{3.4}$$

Fitting of the measured potential behaviors shown in Figure 3.1 using Equation 3.4 was performed and the results are plotted in the same figure. The data fitting was done using the steepest gradient method and the parameters leading to the best fitting results were obtained. Two critical parameters, $\tau_\theta$ and $k$, with respect to frequency for each EC are shown in Figures 3.3c and d. As aforementioned, what determines the potentiation kinetics is the sliding threshold with time.

The fitting results identify different sliding threshold behaviorr against time, depending on the sample (see Figures 3.3a and b). In particular, the threshold increase rate during potentiation shows distinctive features depending on the TE materials. TTP exhibits the steepest threshold increase rate out of the three ECs, whereas NTP exhibits the smallest rate. Accordingly, the time constant of the threshold change ($\tau_\theta$) with time for TTP is smallest and that for NTP is largest, as shown in Figure 3.3d. On the other hand, the synaptic weight change during potentiation, shown in Figure 3.1, was maximized in CTP. This is attributed to the larger constant $k$ for CTP than the other ECs, as the comparison can be seen in Figure 3.3c. Moreover, the constant $k$ for CTP increases with respect to the stimulation frequency, unlike the other ECs, so that the synaptic weight change for CTP does not converge with frequency (see Figure 3.1d).

Taking into account the redox-based mechanisms of ECs, the meaning of the sliding threshold for potentiation can accordingly be interpreted as follows.

The time constant $\tau_\theta$ in Equations 3.3 and 3.4 may reflect the kinetics of the top-electrode-related reduction reaction, for instance, a redox reaction rate constant. Then, a higher reaction rate constant is supposed to increase a threshold change rate, so that the higher the reaction rate constant is, the lower the time $\tau_\theta$ constant is. Possible reduction reactions are as follows: $Ni^{2+} + 2e^- \rightarrow Ni$, $Cr^{3+} + 3e^- \rightarrow Cr$, and $Ti^{4+} + 4e^- \rightarrow Ti$ for NTP, CTP, and TTP, respectively. These reduction reactions are perhaps not spontaneous, as their standard electrode potentials in aqueous solutions are −0.23, −0.74, and −0.86 V, respectively.[14, 15] A critical factor determining the redox reaction rate constant is an overpotential-dependent change in the free energy with respect to the reaction coordinate. On the assumption of the same symmetry for the above-mentioned three reduction reactions, the free energy change on the overpotential is proportional to the number of electrons involved in the reduction reaction. Therefore, at the same negative overpotential for the three ECs, the free energy change of TTP is estimated to be largest, since the reduction of a single $Ti^{4+}$ ion involves the transfer of four electrons, so that the change of the reduction rate constant $k^r_{\mathrm{Ti}^{4+}}$ from the equilibrium value (in case of no external stimulation) is also estimated to be largest. Since the reduction reactions of $Cr^{3+}$ and $Ni^{2+}$ involve the transfer of three and two electrons, respectively, $k^r_{\mathrm{Cr}^{3+}} > k^r_{\mathrm{Ni}^{2+}}$ is estimated, i.e. $k^r_{\mathrm{Ti}^{4+}} > k^r_{\mathrm{Cr}^{3+}} > k^r_{\mathrm{Ni}^{2+}}$.

Accordingly, the time constant $\tau_\theta$ of NTP is estimated to be largest and those of CTP and TTP follow in turn. This estimation is in agreement with the experimental data shown in Figure 3.3d. In spite of this agreement, one should note that this suggested mechanism is based on speculation, since no detailed information on redox reactions related to the STM effect has been revealed, e.g. valence states of metal ions.

As discussed in before, the reason for the highest $\Delta w$ for CTP out of the three ECs is attributed to the parameter $k$ in Equations 3.1 and 3.4. In fact, $k$ is a parameter defining a relation between 'electronic conduction' through the junction and the 'sliding threshold', perhaps determined by the aforementioned reduction kinetics. The read current in the whole measurements is most likely the 'electronic' one rather than an ionic or displacement current. Basically, what is suggested as mechanisms for the STM effect is electronic conductance modulation by the redox reactions. Thus, a higher $k$ value denotes a more significant dependence of the electronic conductance on the redox reactions. To understand top-electrode-dependent $k$ better, one needs to figure out electronic transport behavior through the EC junction.

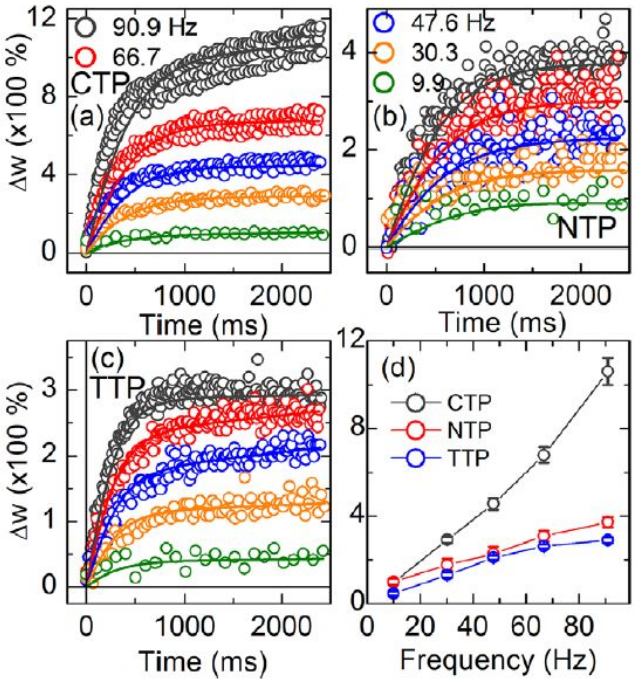


Figure 3.1 Potentiation with respect to time for (a) CTP, (b) NTP, and (c) TTP at various stimulation frequencies (90.9, 66.7, 47.6, 30.3, and 9.9 Hz). The open circles are the measured data. The solid lines were calculated by using the empirical equation, explained in Section 3.2. (d) The $\Delta w$ values, averaged over the time period ($2 \pm 0.1$ s), with respect to the stimulation frequency.

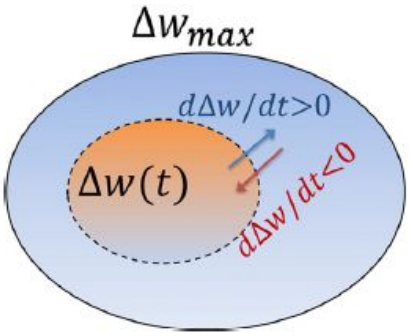


Figure 3.2 Schematic diagram of the synaptic weight change $\Delta w$ at a given time $t$. $\Delta w_{\max}$ means the maximum synaptic weight change, and thus the saturation of synaptic weight is basically assumed.

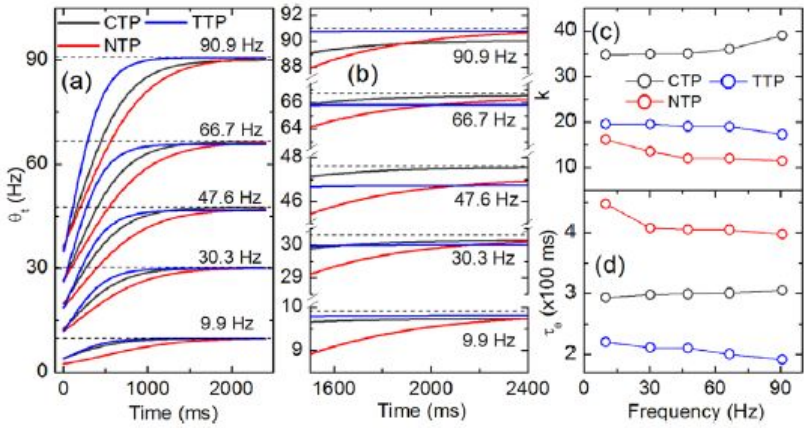


Figure 3.3 (a) Calculated sliding threshold for potentiation as a function of time for the ECs at five different frequencies (90.9, 66.7, 47.6, 30.3, and 9.9 Hz). The dashed lines denote external stimuli. (b) The sliding threshold behaviors are enlarged in the time range 1.5–2.4 s. The critical parameters determining the potentiation behaviors (c) $k$ and (d) $\tau_\theta$ were plotted with respect to stimulation frequency.

## 3.3. Conclusions

$TiO_2$ MIEC layers sandwiched between asymmetric BE and TE (inert BE and redox-reactive TEs) were identified to represent the unidirectional STM effect. In all CTP, NTP, and TTP ECs, negativeand positive-stimulus-induced potentiation and depression, respectively, were observed. Both potentiated and depressed states could not last for a long time, but instead both states underwent relaxation towards the initial state. The three different ECs represented differences in their potentiation behaviors; for example, the much larger change in synaptic weight of CTP than the others. These differences arising from TE materials were parameterized by means of employing an empirical equation including the concept of a 'sliding threshold' for potentiation, as does the BCM rule. Several important parameters in the empirical equation were understood in relation to top-electrode-related redox reactions.

## 3.4. Bibliography


[1] C. Mead, *Analog VLSI and Neural Systems*, Addison-Wesley, Reading, MA, USA 1989.

[2] D. S. Jeong, I. Kim, M. Ziegler, H. Kohlstedt, *RSC Adv.*, 3, 3169 (2012).

[3] R. Waser, R. Dittmann, G. Staikov, K. Szot, *Adv. Mater.*, 21, 2632 (2009).

[4] B. J. Choi, D. S. Jeong, S. K. Kim, C. Rohde, S. Choi, J. H. Oh, H. J. Kim, C. S. Hwang, K. Szot, R. Waser, B. Reichenberg, S. Tiedke, *J. Appl. Phys.*, 98, 033715 (2005).

[5] D. S. Jeong, H. Schroeder, R. Waser, *Electrochem. Solid-State Lett.*, 10, G51 (2007).

[6] D. S. Jeong, R. Thomas, R. S. Katiyar, J. F. Scott, H. Kohlstedt, A. Petraru, C. S. Hwang, *Rep. Prog. Phys.*, 75, 076502 (2012).

[7] J. J. Yang, M. D. Pickett, X. Li, A. A. OhlbergDouglas, D. R. Stewart, R. S. Williams, *Nat. Nano.*, 3, 429 (2008).

[8] E. Bienenstock, L. Cooper, P. Munro, *J. Neurosci.*, 2, 32 (1982).

[9] E. Oja, *J. Math. Biol.*, 15, 267 (1982).

[10] S. M. Dudek, M. F. Bear, *Proc. Natl. Acad. Sci. USA*, 89, 4363 (1992).

[11] E. I. Moser, K. A. Krobert, M.-B. Moser, R. G. M. Morris, *Science*, 281, 2038 (1998).

[12] E. I. Moser, M.-B. Moser, *Neurosci. Biobehav. Rev.*, 23, 661 (1999).

[13] P. Dayan, L. F. Abbott, *Theoretical Neuroscience*, The MIT Press, Cambridge, MA, USA 2001.

[14] A. J. Bard, R. Parsons, J. Jordan, *Standard potentials in aqueous solution*, Marcel Dekker, New York, NY, USA 1985.

[15] D. D. Ebbing, S. D. Gammon, *General chemistry*, Houghton Mifflin, Boston, MA, USA 2009.

# 4. Emulating spiking phenomenon based on non-faradaic Pt/$TiO_2$/Pt

## 4.1. Introduction

Recently, the analog-type resistance plasticity of a metal–insulator–metal capacitor has been utilized in the creation of artificial synapses, based on various physical concepts such as phase-change in higher chalcogenides, ferromagnetism, and nanoionics.[1-14] Not only capacitor-type but also transistor-type artificial synapse has been recently demonstrated.[15] Nanoionics-based artificial synapses can be further classified as anion-migration type, often based on transition metal oxide (TMO) MIEC, and as cation-migration type.[5-14] The plasticity of synaptic weight change in the former type may be attributed to the electrical-stimulus-induced formation of low resistive phases, e.g. lower oxide or metal phases, while that in the latter type may be attributed to metal precipitation. These phases are energetically meta-stable, and thus can be retained for a long time.[10, 11, 16, 17] Several capacitor-like systems exhibiting plastic resistance are popularly referred to as memristors.[18, 19] Because the resistance of artificial synapses defines the degree of association between neighboring artificial neurons, the plasticity of resistance of memristors forms the basis for artificial synapses, and thus denotes the plasticity of neurons' association.

Compared with artificial synapses, artificial neurons emulating action potential firing functions appear to draw little attention despite their importance in communication within neural networks. The reason is most likely that the recent attention to neuromorphic systems is due to their plasticity, i.e. non-volatile, resistance switching phenomenon, which can be utilized in non-volatile memories, e.g. resistive RAMs and phase-change

RAMs.[20-25] Nevertheless, attempts to realize lossless signal transmission and action potential firing by circuit engineering can be found in old publications, for instance, the neuristor concept suggested by Crane in 1962.[26, 27] Krzysteczko et al. had a breakthrough in realizing action potential firing in MgO-based magnetic tunnel junctions, using the spin-transfer-torque-induced mono-stable switching of magnetic state configuration.[4] Recently, the neuristor concept has been revisited: scalable neuristors have been realized using a set of Mott memristors and parallelconnected capacitors, where action potential firing was successfully emulated.[28, 29]

In this study, an attempt is made to realize the 'elastic', i.e. short-lasting, resistance change of an MIEC and to identify its similarities with the action potential firing behavior of a neuron. In this work, $TiO_2$ was chosen as an MIEC, which is estimated to be one of the most promising materials for realization of artificial synapses as well as resistive RAMs. [19, 30-33] The defect structure of hypo-stoichiometric $TiO_2$ was controversial for a long time, concerning whether the major defect type is oxygen vacancy or titanium interstitial.[34-38] Marucco et al. demonstrated that the major defect type is determined by temperature; therefore, oxygen vacancy and titanium interstitial are low- and high-temperature-stable defect types, respectively.[37] Since $TiO_2$ film deposition and electrical characterization in this work were conducted at room temperature, oxygen vacancy was considered as the dominant defect type in this $TiO_2$ MIEC.

## 4.2. Results and discussions

The electric conduction behavior of the Pt/$TiO_2$/Pt capacitor was investigated with applying square-shaped voltage pulses. The width of voltage pulses varied from sub-ms to 100 ms. By utilizing a voltage divider, the response current was converted into response voltage, i.e. output voltage $V_{out}$.

In this manner, the output voltage responding to the input voltage $V_{in}$ pulses was evaluated. Two different schemes of voltage application were employed: (i) polarization voltage $V_{pol}$ pulses with a background dc voltage of zero, i.e. $V_{in} = V_{pol}$, and (ii) depolarization voltage $V_{depol}$ pulses superimposed on a background dc $V_{pol}$, i.e. $V_{in} = V_{pol} - V_{depol}$. In the former case, the used circuit diagram is shown in the inset of Figure 4.1a. A voltage divider $R_0$ (1 kohm) was connected in series to the Pt/$TiO_2$/Pt capacitor $R_{MIEC}$. Figure 4.1a and b show the square-shaped input voltage pulses, with four different heights (1, 2, 3, and 4 V) and a 10 ms pulse width, and the output voltage pulses, respectively. The abrupt increase in the output voltage with the input voltage is shown in Figure 4.1b, suggesting that voltage spikes are generated, i.e. voltage spike firing, relying on the magnitude of external stimulation. Figure 4.1c shows output voltage with respect to input voltage pulse height (0.2–4 V) and width (0.2–100 ms). In the figure, it can be noticed that increasing the input voltage pulse width leads to a decrease in the height required for a particular output voltage. This implies that the voltage spike firing is a function of, at least, two independent variables, i.e. voltage and time. Thus, the aforementioned magnitude of external stimulation should include the quantities of these two variables. In fact, it is found that input voltage pulses of 4 V height and 100 ms width result in the largest output voltage spike.

In the latter case, i.e. application of $V_{depol}$ pulses superimposed on a background dc $V_{pol}$, the employed circuit diagram is depicted in the inset of Figure 4.1d. In the circuit, a voltage divider (also 1 kohm) was ahead of the capacitor. A dc $V_{pol}$ of 3 V was applied to the circuit and $V_{depol}$ pulses of different heights (0.4, 0.8, 1.2, 1.6, and 2.0 V) and a 10 ms width were superimposed on the $V_{pol}$. The $V_{depol}$ pulses and consequent $V_{in}$ pattern, i.e. $V_{pol}$–$V_{depol}$, are plotted in Figure 4.1d. At a 3 V dc $V_{pol}$, the $V_{out}$ was approximately 1.6 V, implying that the capacitor's resistance becomes

comparable to that of the voltage divider (1 kohm) at the given $V_{in}$. In this study, this output voltage is termed as the 'resting potential'.

Insomuch as the Pt/$TiO_2$/Pt capacitor is a passive element, the $V_{depol}$ pulses imposed on the capacitor reduce the output voltage as shown in Figure 4.1e. However, when a $V_{depol}$ pulse ends, i.e. re-polarization starts, a voltage-spike is generated and its height is larger than the resting potential. Voltage-spike height can be defined as the deviation of the voltage spike maximum from the resting potential level ($\Delta V_{out}$). The voltage spike height with respect to the height and width of the $V_{depol}$ pulses is plotted in Figure 4.1f. It turns out that the voltage spike height relies on both $V_{depol}$ pulse height and width and it increases with the $V_{depol}$ pulse height and width. In fact, $V_{depol}$ pulses of the largest height (3 V) and width (60 ms) give rise to the largest output voltage as can be seen in Figure 4.1f.

The ionic-to-electronic conduction transition was also observable in the case of application of square-shaped voltage pulses. In Figure 4.1b, the abrupt increase in the output voltage with the input voltage is attributed to the decrease of the capacitor's resistance with the input voltage, which results from the ionic-to-electronic conduction transition and non-linear J-V relation. At 1 V, the output voltage decreases during single pulse application, implying the electrical charging due to the polarization of oxygen vacancy distribution, and thus negligible electronic current (see the inset of Figure 4.1b). However, at 2 V, it can be seen that the output voltage increases during single pulse application, suggesting a gradual decrease in the capacitor's resistance, which results from the evolution of EMF for electronic conduction. Accordingly, the threshold voltage for ionic-to-electronic conduction transition is between 1 and 2 V.

Keeping in mind that the ionic-to-electronic conduction transition as well as EMF evolution arises from oxygen vacancy migration, it is estimated that the polarization-induced voltagespike firing behavior shown in Figure 4.1b is

controlled by the kinetics of oxygen vacancy migration. The ionic-to-electronic conduction transition and EMF evolution occur while the capacitor is polarized, i.e. the distribution of oxygen vacancies is polarized, so that the kinetics of oxygen vacancy 'drift' is of great importance in the phenomenon. The output voltage-spike of the circuit in the inset of Figure 4.1a therefore varies on voltage, a driving force for oxygen vacancy 'drift', and time as plotted in Figure 4.1c. Increasing oxygen vacancies' drift time, i.e. input voltage pulse width, and low driving force for oxygen vacancy drift, i.e. voltage height, are required for a particular polarization and the consequent output voltage.

The above-mentioned voltage-spike firing behavior arises from the polarization of the non-faradaic capacitor that is depolarized in its resting state. In contrast, in a neuron, due to the presence of the resting potential (−70 mV), the membrane is polarized (depolarized) in the resting (excited) state. As briefly mentioned earlier, this polarized resting state is attributed to $Na^+/K^+$-ATPase ion pumps serving as a power source by converting chemical energy into electrical energy, i.e. Nernst potential.[39] These ion pumps therefore let the cell membrane be an "active element", and thus act as a lossless cable transmitting action potentials. In this sense, the depolarization-induced voltage-spike firing behavior shown in Figure 4.1e shares some common aspects with the action potential firing behavior in neurons. The polarization voltage (3 V) results in the resting potential (ca. 1.6 V) and serves as an additional energy source as ATPase ion pumps. The polarization voltage was found to be above a threshold for the ionic-to-electronic conduction transition, so that the capacitor's resistance was comparable to that of the voltage divider. During the depolarization period, the capacitor's resistance increases. Especially, if the depolarization voltage is high enough to lower the input voltage below a voltage for the electronic-to-ionic conduction transition, a

very large decrease in the capacitor's resistance takes place. Thus, the subsequent re-polarization period begins with a high output voltage that decreases with time, due to the decrease of the capacitor's resistance with time during the polarization period. What matters in the depolarization-induced voltage-spike firing is the kinetics of oxygen vacancy redistribution by 'diffusion' rather than drift. Thus, it is expected that output voltage-spike is significantly affected by the height and width of depolarization voltage pulses. Figure 4.1f identifies this relationship, where voltage-spike height is defined as the deviation of the voltage-spike height from the resting potential level ($\Delta V_{out}$). It can be seen that the voltagespike increases with the height and width of the depolarization voltage pulses since the decrease of the capacitor's resistance becomes larger when depolarized by larger and wider depolarization voltage pulses.

Compared to the polarization-induced voltage-spike firing, the depolarization-induced voltage-spike firing is perhaps favorable because of the presence of a polarization voltage source. The polarization voltage source enables the circuit to be active, and thus the continuous loss of output voltage-spike, while the voltage-spike travels along passive circuit elements, is likely to be avoided. Of course, how to implement this concept in integrated circuits is an open question at this moment.

Comparing the non-faradaic capacitor with several TMO MIEC systems mimicking the artificial synapses with plasticity, one may guess that the nature of the electrode–MIEC interface is a lasting-time-determining factor. For instance, Pd/$WO_x$/W artificial synapses that Chang et al. reported may represent a relationship between non-blocking contact and plasticity.[8] Possible redox reactions at the $WO_x$–W interface may provide a non-blocking contact nature and thus the reactions impede depolarization, consequently giving plasticity. Moreover, redox reactions at the metal–MIEC interface

perhaps lead to phase transition into low resistive phases, e.g. lower oxide phases and metal phases, which are energetically meta-stable.

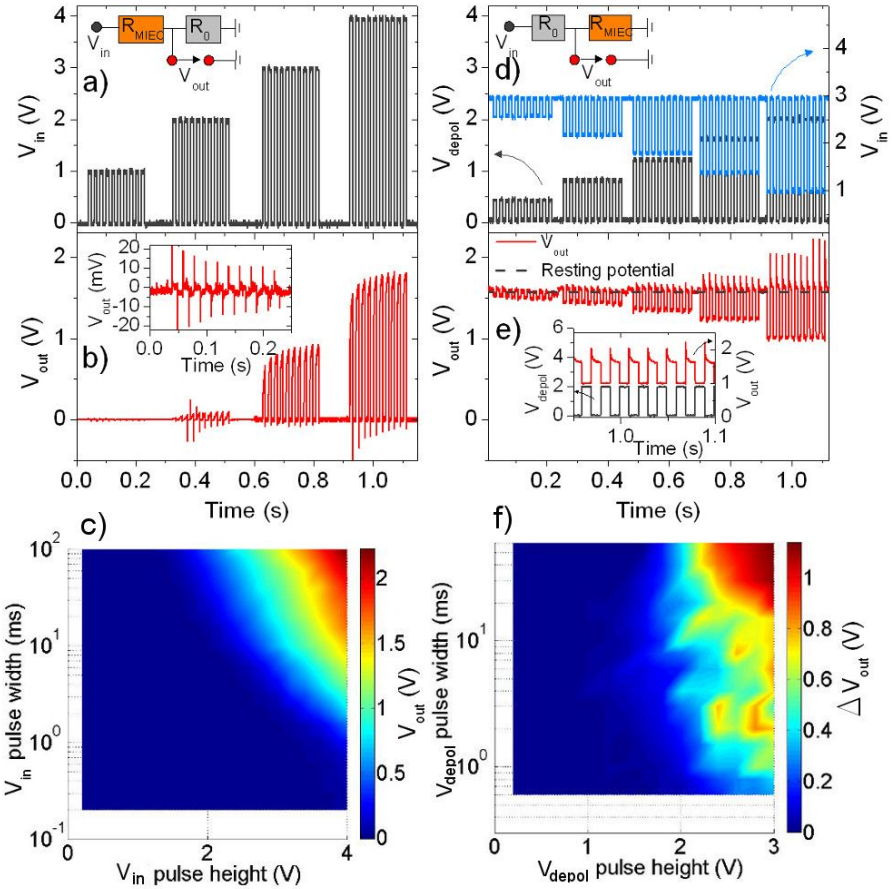


Figure 4.1 Voltage-spike firing in the non-faradaic capacitor. (a) Square-shaped voltage pulses applied to the circuit depicted in the inset for observing polarization-induced voltage-spike firing. (b) Resulting $V_{out}$ pulses. An enlarged $V_{out}$ pattern in the time period 0 – 0.25 s is plotted in the inset. (c) A $V_{out}$ map against $V_{pol}$ ($V_{in}$) pulse height and width. (d) $V_{depol}$ pulses and the net $V_{in}$ pattern, applied to the circuit shown in the inset, for depolarization-induced voltage-spike firing. (e) Resulting $V_{out}$ pulses. The $V_{depol}$ and $V_{out}$ profiles in the time period 0.95 – 1.1 s are plotted in the inset. (f) A map of $\Delta V_{out}$, against $V_{depol}$ pulse height and width.

## 4.3. Conclusions

In this study, the current–voltage hysteresis of $TiO_2$-based non-faradaic capacitors is investigated to primarily focus on the correlation between the blocking contact and the elasticity, i.e. non-plasticity, of the capacitors' resistance change, in experimental methods. The similarity between the action potential firing behavior in neurons and the elasticity of the non-faradaic capacitors is addressed. The electronic conduction is much more sensitive to an applied voltage than the ionic conduction so that, after transition into the electronic conduction regime, the nonfaradaic capacitor shows a drastic increase in current with the voltage. Given that this transition is caused by oxygen vacancy migration kinetics, i.e. dynamics, a threshold voltage for the transition depends not only on input voltage pulse height but also on its pulse width. That is, both types of input information, i.e. pulse height and width, can be encoded, generating output voltage pulses as long as the input quantities exceed thresholds for the transition.

Although the aforementioned circuits including the non-faradaic capacitor represent similarities to biological neurons, there are a few features of the biological neuron's spiking behavior which are difficult to be emulated by employing the non-faradaic capacitor. For instance, (i) repetitive spike generation, i.e. spike train, under a constant stimulus instead of repetitive stimuli, and (ii) the existence of refractory periods. These features contribute to encoding the constant input stimulus into spiking activity, i.e. analog-to-analog type information encoding. The analog type encoding process will be explained and determined in next sections based on the oscillatory circuit composed by TS and passive circuit elements.

## 4.4. Bibliography


[1] D. S. Jeong, I. Kim, M. Ziegler, H. Kohlstedt, *RSC Adv.*, 3, 3169 (2012).

[2] M. Suri, O. Bichler, D. Querlioz, B. Traoré, O. Cueto, L. Perniola, V. Sousa, D. Vuillaume, C. Gamrat, B. DeSalvo, 112, 054904 (2012).

[3] D. Kuzum, R. G. D. Jeyasingh, B. Lee, H. S. P. Wong, *Nano Lett.*, 12, 2179 (2011).

[4] P. Krzysteczko, J. Münchenberger, M. Schäfers, G. Reiss, A. Thomas, *Adv. Mater.*, 24, 762 (2012).

[5] Y. Shimeng, W. Yi, R. Jeyasingh, D. Kuzum, H. S. P. Wong, *IEEE Trans. Electron Devices*, 58, 2729 (2011).

[6] Y. Liu, T. P. Chen, Z. Liu, Y. F. Yu, Q. Yu, P. Li, S. Fung, *Appl. Phys. A*, 105, 855 (2011).

[7] T. Chang, S. H. Jo, K. H. Kim, P. Sheridan, S. Gaba, W. Lu, *Appl. Phys. A: Mater. Sci. Process.*, 102, 857 (2011).

[8] T. Chang, S.-H. Jo, W. Lu, *ACS Nano*, 5, 7669 (2011).

[9] Z. Q. Wang, H. Y. Xu, X. H. Li, H. Yu, Y. C. Liu, X. J. Zhu, *Adv. Funct. Mater.*, n/a (2012).

[10] T. Ohno, T. Hasegawa, T. Tsuruoka, K. Terabe, J. K. Gimzewski, M. Aono, *Nat. Mater.*, 10, 591 (2011).

[11] T. Hasegawa, T. Ohno, K. Terabe, T. Tsuruoka, T. Nakayama, J. K. Gimzewski, M. Aono, *Adv. Mater.*, 22, 1831 (2010).

[12] M. Ziegler, R. Soni, T. Patelczyk, M. Ignatov, T. Bartsch, P. Meuffels, H. Kohlstedt, *Adv. Funct. Mater.*, 22, 2744 (2012).

[13] S. H. Jo, T. Chang, I. Ebong, B. B. Bhadviya, P. Mazumder, W. Lu, *Nano Lett.*, 10, 1297 (2010).

[14] A. V. Avizienis, H. O. Sillin, C. Martin-Olmos, H. H. Shieh, M. Aono, A. Z. Stieg, J. K. Gimzewski, *Plos One*, 7, e42772 (2012).

[15] M. Ziegler, M. Oberländer, D. Schroeder, W. H. Krautschneider, H. Kohlstedt, *Appl. Phys. Lett.*, 101, 263504 (2012).

[16] D.-H. Kwon, K. M. Kim, J. H. Jang, J. M. Jeon, M. H. Lee, G. H. Kim, X.-S. Li, G.-S. Park, B. Lee, S. Han, M. Kim, C. S. Hwang, *Nat. Nanotechnol.*, 5, 148 (2010).

[17] J. P. Strachan, M. D. Pickett, J. J. Yang, S. Aloni, A. L. David Kilcoyne, G. Medeiros-Ribeiro, R. Stanley Williams, *Adv. Mater.*, 22, 3573 (2010).

[18] L. O. Chua, *IEEE Trans. Circuit Theory*, 18, 507 (1971).

[19] D. B. Strukov, G. S. Snider, D. R. Stewart, R. S. Williams, *Nature*, 453, 80 (2008).

[20] D. S. Jeong, R. Thomas, R. S. Katiyar, J. F. Scott, H. Kohlstedt, A. Petraru, C. S. Hwang, *Rep. Prog. Phys.*, 75, 076502 (2012).

[21] R. Waser, M. Aono, *Nat. Mater.*, 6, 833 (2007).

[22] R. Waser, R. Dittmann, G. Staikov, K. Szot, *Adv. Mater.*, 21, 2632 (2009).

[23] M. Wuttig, N. Yamada, *Nat. Mater.*, 6, 824 (2007).

[24] Y. Yang, P. Gao, S. Gaba, T. Chang, X. Pan, W. Lu, *Nat. Commun.*, 3, 732 (2012).

[25] Y. Yang, P. Sheridan, W. Lu, *Appl. Phys. Lett.*, 100, 203112 (2012).

[26] H. D. Crane, *Proc. IRE*, 50, 2048 (1962).

[27] R. D. Parmentier, *Proc. IEEE*, 58, 1829 (1970).

[28] M. D. Pickett, G. Medeiros-Ribeiro, R. S. Williams, *Nat. Mater.*, 12, 114 (2012).

[29] M. D. Pickett, R. S. Williams, *Nanotechnology*, 23, 215202 (2012).

[30] B. J. Choi, D. S. Jeong, S. K. Kim, C. Rohde, S. Choi, J. H. Oh, H. J. Kim, C. S. Hwang, K. Szot, R. Waser, B. Reichenberg, S. Tiedke, *J. Appl. Phys.*, 98, 033715 (2005).

[31] D. S. Jeong, H. Schroeder, R. Waser, *Electrochem. Solid-State Lett.*,

10, G51 (2007).

[32] C. Nauenheim, C. Kuegeler, A. Ruediger, R. Waser, *Appl. Phys. Lett.*, 96, 122902 (2010).

[33] J. J. Yang, M. D. Pickett, X. Li, A. A. OhlbergDouglas, D. R. Stewart, R. S. Williams, *Nat. Nano.*, 3, 429 (2008).

[34] U. Balachandran, N. G. Eror, *J. Mater. Sci.*, 23, 2676 (1988).

[35] J. F. Baumard, D. Panis, A. M. Anthony, *J. Solid State Chem.*, 20, 43 (1977).

[36] P. Kofstad, *J. Phys. Chem. Solids*, 23, 1579 (1962).

[37] J.-F. Marucco, J. Gautron, P. Lemasson, *J. Phys. Chem. Solids*, 42, 363 (1981).

[38] C. Meis, J. L. Fleche, *Solid State Ionics*, 101–103, Part 1, 333 (1997).

[39] J. Astrup, P. M. Sørensen, H. R. Sørensen, *Stroke*, 12, 726 (1981).

# 5. Neuristor-based leaky integrate-and-fire neuron

## 5.1. Introduction

The human brain—three pounds of matter between our ears—has not yet been understood completely because of its complexity. For many decades, researchers have focused on understanding the principles and detailed actions of the human brain and, in general, the mammalian brain.[1-4] The unique functionalities of the mammalian brain, such as parallel information processing, low power consumption, and learning capacity, make it fascinating. These unique functionalities are of great interest to not only neuroscientists but also physicists and electrical/materials engineers. There have been many attempts to realize 'artificial brains' either by hardware- or software-based techniques.[5-10]

The basic elements in a mammalian brain—a complex neural network—are neurons and synapses; synapses define the connectivity between neighboring neurons, and function as local memories.[11] Synapses and neurons are the basic elements in SNNs as well. Neurons are of significant importance as they generate action potentials (also known as spikes), and work as information units in neural networks.[2]

As discussed in Section 4.3, there are several limitations for employing single Pt/$TiO_2$/Pt non-faradaic capacitor as a spiking neuron: (i) a spike train generation under a constant input instead of repetitive sets of input stimuli and (ii) refractory periods. However, various types of artifical neuron models can represent aformentioned characterisitcs. That is due to the fact that artifical neuron models sufficiently reflect oscillating nature of membrane potential of the biological neuron.

Various types of artificial neuron models can be employed in SNNs, such as leaky integrate-and-fire (LIF) neuron,[1-3] Hodgkin-Huxley neuron,[12] and Izhikevich neuron models.[13, 14] Among these, the LIF neuron is the simplest model and can be easily implemented in SNNs.[1-3] An example of artificial hardware neurons by employing functioning resistive switching system that could partly replace CMOS-based elements is a recent breakthrough by Pickett et al., who achieved the LIF neuron by using two pairs of a Mott insulator and a capacitor.[15] Basically, the neuristor concept introduced by Crane[16] in 1962 was employed in the LIF neuron model; hence this LIF neuron is termed as neuristor-based LIF (NLIF) neuron in this study so as to differentiate it from the standard LIF neuron.

Mott insulators are known to undergo temperature-driven insulator-to-metal transitions, so that the conductivity abruptly increases when the lattice temperature exceeds the transition temperature.[17] This transition is reversible, that is, the initial conductivity is recovered when the lattice temperature again falls below the threshold for the reverse transition, i.e., metal-to-insulator transition. As the lattice temperature change is due to Joule heating, the current-voltage (I-V) behavior of the Mott insulator is estimated to be volatile, i.e., threshold switching.[18-20] Threshold switching plays a key role in the functioning of the NLIF neuron.[15, 20] Other than the Mott insulator, amorphous higher chalcogenides,[21-24] Si n+/p/n+ junctions,[25] and particular TMOs such as NbOx[20, 26] are also known to exhibit volatile threshold switching.

Regardless of the type of threshold switch (TS) in the NLIF neuron, the variability of threshold switching behavior cannot be completely avoided. It is, therefore, required to determine the effect of this variability on the neuronal behavior of the NLIF neuron that often leads to neuronal noises. The quantitative understanding of the noise is of significant importance when employing the NLIF neuron in both in silico and hardware-based ANNs

because some noise properties are acceptable in ANNs insomuch as the noise does not cause serious errors during information processing.[27]

In this study, we conducted simulation on the NLIF neuron so as to identify its neuronal behavior, in particular, its possible noise and information representation in the presence of noise. Indeed, the employed analysis methods are widely used in characterization of other neuron models[1, 3, 28, 29] so that one can readily compare the characteristics of the NLIF neuron model with those of other models.

We first attempted to find optimized operational windows for the variables in the NLIF neuron model. It was indeed not an easy task to find the windows owing to the many variables involved simultaneously. We suggest a method to find successful spike firing conditions by conducting static and dynamic calculations on the NLIF neuron circuit. The acquired windows should be narrowed down by taking into account the optimal selectivity of individual NLIF neurons for stimulation. The neuronal selectivity is one of the essential functions of neurons, given that they work as information encoders, in particular, in the presence of noise. Next, we assumed the variability of the TS in an individual NLIF neuron under optimal firing conditions. Such variability is most likely seen every switching cycle[23, 30] i.e. switching-event-driven variability. Insomuch as threshold switching events occur in succession in the entire period of external stimulation, the variability of the TS leads to a noise in the neuron's response. By analyzing the noise property, the relationship between the distribution and the consequent noise is understood and compared with the noise present in biological neurons. A question arising from the analysis on individual NLIF neurons is "Can conveying information, such as encoding and decoding, be achieved in a reliable manner by a population of these individual NLIF neurons?" This question is related to neuronal behavior at a higher dimension, i.e., the group, rather than at the individual neuronal level. The Bayesian decoder is employed so as to examine the reliability of

the information conveyed by a population of NLIF neurons. As a result, the reliability is evaluated by means of "uncertainty."

## 5.2. Results

### 5.2.1. Optimal firing conditions of individual NLIF neurons

In a single NLIF neuron circuit, standard circuit elements such as resistors ($R_1$, $R_2$, and $R_L$), capacitors ($C_1$ and $C_2$), and TSs ($S_1$ and $S_2$) are in use, as shown in Figure 5.1a.[15] When it comes to a network of NLIF neurons, $V_2$ in Figure 5.1a is relayed to a neighboring neuron through synapse, so that $V_2$ is the output voltage, corresponding to membrane potential. To generate a positive spike $V_2$, $V_{dc2}$ and $V_{dc1}$ need to be positive and negative, respectively. For simplicity, it is assumed that $V_{dc2} = -V_{dc1} = V_d$. The two dc voltage sources ($V_{dc1}$ and $V_{dc2}$) effectively supply power, enabling active operation, and determine the spike firing dynamics including the spike's height and the level of undershoot following the spike. The spike firing dynamics will be accounted for in detail later. The key component in the NLIF neuron is the TS that performs monostable switching. The monostability of a TS can be understood from the schematic of current-voltage (I-V) hysteresis of the TS illustrated in Figure 5.1b. The behavior of the TS is described by four parameters: $R_{on}$, $R_{off}$, $V_{on}$, and $V_{off}$, which denote the on- and off-state resistances and threshold voltages for off-to-on and on-to-off switching, respectively. The assumption of linear I-V behaviors in both the states allows constant $R_{on}$ and $R_{off}$ in a given operational voltage range. For simplicity, switches $S_1$ and $S_2$ are assumed to be identical.

The NLIF neuron fires spikes only when switch $S_2$ flickers at a given input current ($I_{in}$). Note that the term "flicker" means completing a threshold switching cycle, for instance, a cycle along the arrows in Figure 5.1b. To meet

this requirement, the five standard circuit components ($R_1$, $R_2$, $R_L$, $C_1$, and $C_2$), the four operational parameters of the TS ($R_{on}$, $R_{off}$, $V_{on}$, and $V_{off}$), and the dc voltage ($V_d$), i.e., ten variables in total, should be optimized. Owing to the difficulty in optimizing such a large number of variables, it is required to rule out several variables, in particular the operational parameters of the TS, that are most likely estimated from available experimental data. In this calculation, $R_{off}$ and $V_{on}$ were set to 1 Mohm and 1 V, respectively, so that only two variables ($R_{on}$ and $V_{off}$) of the TS remain. They were converted to the following normalized variables: $R_{off}/R_{on}$ and $V_{off}/V_{on}$. These threshold switching parameters are summarized in Table 5.1. Note that these ratios often are employed in characterizing resistive switching devices. A further reduction in the number of variables was made by setting $R_d$ and $V_d$ to 1 Gohm and 0.9 V, respectively. $R_L$ works as a voltage divider in this single neuron; it is desired to be large. $V_d$ needs to be close to, but smaller than, $V_{on}$ so as to turn on switch $S_2$ with a small input current $I_{in}$; 90 percent of $V_{on}$, i.e., 0.9 V, was taken as $V_d$.

To arrive at a condition of flickering switch $S_2$ at a given $I_{in}$, time-independent calculations were performed with capacitors $C_1$ and $C_2$ ruled out (see Figure 5.2a). The calculations provided $R_1$ and $R_2$ windows for spike firing at given $R_{off}/R_{on}$ and $V_{off}/V_{on}$ values. The condition drawn from these static calculations is a "prerequisite" for successful spike firing in the time domain. This is because the capacitors only determine the rate of voltage redistribution in the NLIF neuron upon switching of $S_1$ and $S_2$, and the voltages across the two switches will eventually reach $V_d$. Meeting the four requirements, shown in Figure 5.2b and described below, allows $S_2$ to flicker. Note that on-switching of switch $S_1$ is a necessary condition for that of switch $S_2$, but off-switching of switch $S_1$ is unnecessary for that of switch $S_2$. **Requirement i**: setting $R_{off}$ for both switches in the circuit results in a voltage across switch $S_1$ ($|V_1+V_d|$) that is larger than $V_{on}$, leading to the off-to-on

switching of switch $S_1$, given the aforementioned necessary condition for on-switching of switch $S_2$. **Requirement ii**: setting $R_{on}$ and $R_{off}$ for switches $S_1$ and $S_2$, respectively, results in a voltage across switch $S_2$ ($|V_2-V_d|$) that is larger than $V_{on}$, leading to off-to-on switching of switch $S_2$. **Requirement iii**: setting $R_{off}$ and $R_{on}$ for switches $S_1$ and $S_2$, respectively, allows on-to-off switching of switch $S_2$ by decreasing $|V_2-V_d|$ below $V_{off}$. **Requirement iv**: setting $R_{on}$ for both switches allows on-to-off switching of switch $S_2$ regardless of on- or off-switching of switch $S_1$, given that off-switching of switch $S_1$ is not a necessary condition for that of switch $S_2$. Satisfying these requirements, $R_2$ windows with respect to input current $I_{in}$ (1 μA) and combinations of $R_{off}/R_{on}$ (5, 10, 20, and 50) and $V_{off}/V_{on}$ (0.3, 0.5, and 0.7) values were obtained as indicated using the grey zones in Figure 5.2c. The white zones correspond to the failure of spike firing. Insomuch as a current rather than a voltage is applied, $R_1$ and $R_2$ are independent variables as can be seen in Figure 5.2c. It is noticed that the higher $R_{off}/R_{on}$ and the lower $V_{off}/V_{on}$ ratio are, the wider $R_2$ window is. For the following calculations, we chose moderate parameters of the TS ($R_{off}/R_{on}$ = 20 and $V_{off}/V_{on}$ = 0.5) and $R_1$ and $R_2$ of 100 kohm.

As mentioned earlier, the windows drawn from the static calculations serve as necessary, rather than sufficient, conditions for successful firing of the NLIF neuron in a time domain; therefore, capacitors $C_1$ and $C_2$ need be optimized as well. The only concern in spike firing in due course would be the sequential on-switching events of switches $S_1$ and $S_2$ when both are in the off-state, i.e., aforementioned Requirements i and ii are met in consecutive order. The major role of capacitors $C_1$ and $C_2$ in spike firing is time-dependent redistribution of $V_1$ and $V_2$ upon switching of $S_1$ and $S_2$. The capacitors determine the rate of the redistribution. That is, the higher the capacitance, the lower the rate. To satisfy the above-mentioned requirements, the time required for the evolution of $V_2$—eventually leading to $|V_2-V_d| > V_{on}$, i.e., on-switching of switch $S_2$ upon the on-switching of switch $S_1$—should be sufficiently short

to hinder the off-switching of switch $S_1$ in the meantime. Otherwise, an increase in $|V_2-V_d|$ in due course, owing to the on-switching of switch $S_1$, would be abruptly diminished before $V_{on}$ is reached. Note that it was assumed that the switching times of $S_1$ and $S_2$ are sufficiently short to have a negligible impact on the time-dependent voltage redistribution. In addition, regarding the off-switching of switch $S_2$, the static calculations basically assume the instability of the on-state of switch $S_2$ (see Requirements iii and iv), and thus off-switching occurs regardless of capacitances of $C_1$ and $C_2$.

Given the above-mentioned requirements, a capacitance window for spike firing at an input current of 1 μA is obtained as shown in Figure 5.3a. The input current profile with respect to time is plotted in Figure 5.3d. The maximum capacitance of $C_2$ for successful spike firing at a given capacitance of $C_1$ tends to increase monotonically with that of $C_1$. A higher capacitance of $C_1$ allows a longer discharging time of $C_1$; the discharging arises from the on-switching of switch $S_1$ and continues as far as $|V_1+V_d| > V_{off}$, i.e., off-switching of switch $S_1$. A higher capacitance of $C_2$ allows the charging time of $C_2$ to be longer; the charging arises from an increase in $|V_2|$ ($V_2 < 0$) occurring upon the prior on-switching of switch $S_1$ and continues until $|V_2-V_d| > V_{on}$, i.e., on-switching of switch $S_2$. Thus, a higher capacitance of $C_1$ enables the capacitance range of $C_2$ to widen, leading to the formation of the capacitance window shown in Figure 5.3a. To highlight the capacitance dependence, four $C_1$ and $C_2$ pairs, denoted by α, β, γ and δ in Figure 5.3a, were sampled and for each pair a "membrane potential," i.e., $V_2$, the profile with respect to time was evaluated for the given input current $I_{in}$. The results plotted are shown in Figures 5.3b and 5.3c. In case of δ, the charging period of capacitor $C_2$ is longer than the discharging period of capacitor $C_1$, and thus switch $S_1$ recovers its off-state before a transition of switch $S_2$ into the on-state. Therefore, no spike firing is observed (see Figure 5.3c). To closely look at the evolution of $V_1$, $V_2$ $R_{S1}$ ($R$ of $S_1$), and $R_{S2}$ ($R$ of $S_2$) for β case, their time-dependent

behaviors are zoomed in in Figures 5.3e and 5.3f. These variables are self-consistent, which will be dealt with in detail below.

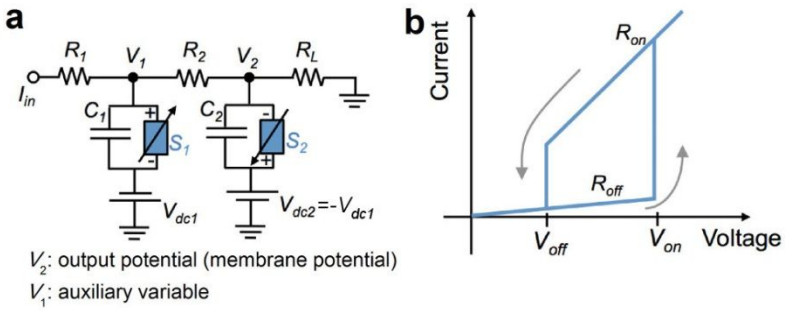


Figure 5.1 Circuitry of NLIF neuron and threshold switching behavior. (a) Circuitry of the NLIF neuron. (b) A schematic of *I*–*V* behavior of a TS.

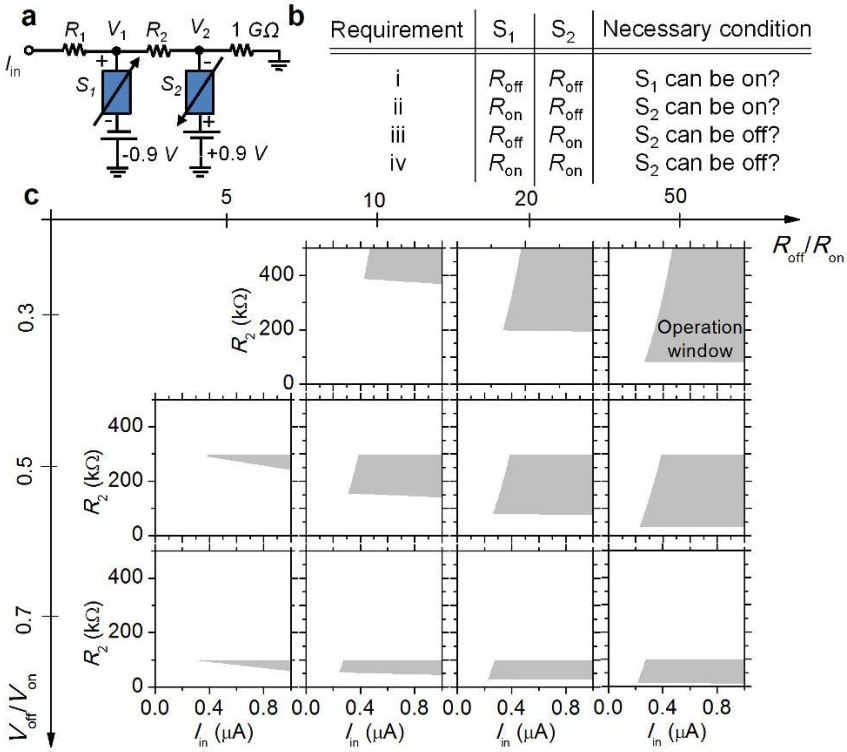


Figure 5.2 Operational windows of series resistance. (a) Circuitry of the NLIF neuron for static calculations. $R_L$, $V_d$, and $I_{in}$ are set as 1 Gohm, 0.9 V, and 1 μA, respectively. (b) A table of requirements for successful spike firing. (c) Acquired operational windows (gray zones) of $R_1$ and $R_2$ for successful spike firing at given ratios of $R_{off}/R_{on}$ and $V_{off}/V_{on}$.

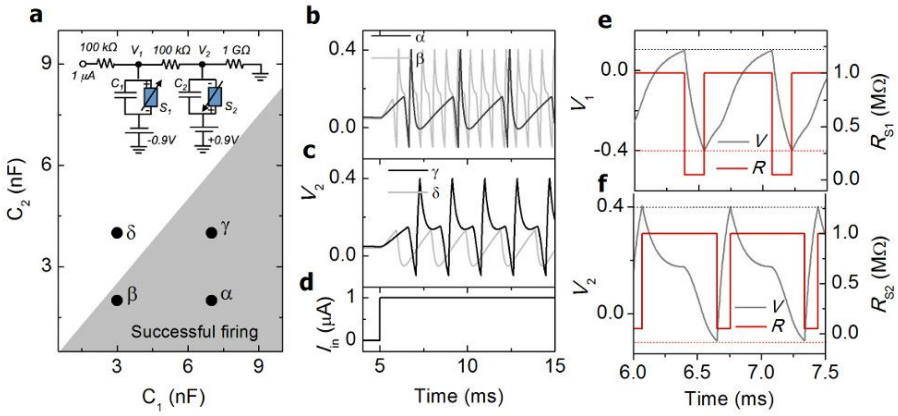


Figure 5.3 Operational windows of capacitance. (a) Window of $C_1$ and $C_2$ (gray zone) for successful spike firing in due course, evaluated by time-dependent calculation. The inset shows the NLIF neuron circuit with parameters used in this calculation. Four combinations of $C_1$ and $C_2$, α (3 nF, 2 nF), β (7 nF, 2 nF), γ (7 nF, 4 nF), and δ (3 nF, 4 nF), are sampled and voltage-time behaviors of NLIF neurons with the capacitance combinations are plotted in (b) and (c). Input current $I_{in}$ is shown in (d). For β case, the evolution of $V_1$, $V_2$ $R_{S1}$ ($R$ of $S_1$), and $R_{S2}$ ($R$ of $S_2$) is zoomed in in (e) and (f) to identify the self-consistent relation between them. The black and the red dashed line denote thresholds for on- and off-switching, respectively.

Table 5.1 Parameters used in the optimization of the operational window.

| Symbol | Note | Value | Reference |
|---|---|---|---|
| $R_{off}$ [a] | Parameter | 1 MΩ | [21, 22] |
| $R_{on}$ | Variable | - | |
| $V_{off}$ | Variable | - | |
| $V_{on}$ | Parameter | 1.0 V | [23, 26] |

### 5.2.2. Spiking dynamics of the NLIF neurons

The spike firing dynamics is described by the membrane potential $V_2$ and the auxiliary variable $V_1$ as follows:

$$C_1 \frac{dV_1}{dt} = I_{in} - \frac{1}{R_{S1}}(V_1 - V_{dc1}) - \frac{1}{R_2}(V_1 - V_2) \tag{5.1}$$

and

$$C_2 \frac{dV_2}{dt} = \frac{1}{R_2}(V_1 - V_2) - \frac{1}{R_{S2}}(V_2 - V_{dc2}) - \frac{1}{R_L}V_2, \tag{5.2}$$

where $R_{S1}$ and $R_{S2}$ denote the resistance of $S_1$ and $S_2$, respectively. The NLIF neuron model is similar to the LIF neuron model regarding such that capacitor $C_2$ integrates potential and fires a spike when the threshold for the on-switching of $S_2$ is reached. However, a difference lies in the auxiliary variable $V_1$ and switch $S_1$, which are self-consistently related to each other according to Eqaution 5.1. Thus, the spike firing dynamics is mapped onto a $V_1$-$V_2$ phase plane, which is analogous to two-dimensional, i.e. simplified, Hodgkin-Huxley neuron models such as FitzHugh-Nagumo model.[31, 32] According to Equations 5.1 and 5.2, $V_1$- and $V_2$-nullcline are defined by the following linear equations,

$$V_1 - \frac{R_{S1}}{R_2+R_{S1}}V_2 - \frac{R_2 V_{dc1}}{R_2+R_{S1}} - \frac{R_2 R_{S1}}{R_2+R_{S1}}I_{in} = 0, \tag{5.3}$$

and

$$V_1 - R_2\left(\frac{1}{R_2} + \frac{1}{R_{S2}} + \frac{1}{R_L}\right)V_2 + \frac{R_2 V_{dc2}}{R_{S2}} = 0, \tag{5.4}$$

respectively. Given the history- and voltage-dependence of $R_{S1}$ and $R_{S2}$, these nullclines are history- and voltage-dependent. If i) $|V_1 - V_{dc1}| \leq |V_{off}|$ or ii) $|V_{off}| < |V_1 - V_{dc1}| < |V_{on}|$ and $|V_1\text{-}V_{dc1}|$ immediately before entering into this voltage region in time was smaller than $V_{off}$, $V_1$-nullcline is given by

$$V_1 - \frac{R_{off}}{R_2+R_{off}}V_2 - \frac{R_2 V_{dc1}}{R_2+R_{off}} - \frac{R_2 R_{off}}{R_2+R_{off}}I_{in} = 0, \tag{5.5}$$

and if i) $|V_1 - V_{dc1}| \geq |V_{on}|$ or ii) $|V_{off}| < |V_1 - V_{dc1}| < |V_{on}|$ and $|V_1\text{-}V_{dc1}|$ immediately before entering into this voltage region in time was larger than $V_{on}$, the nullcline is given by

$$V_1 - \frac{R_{on}}{R_2+R_{on}} V_2 - \frac{R_2 V_{dc1}}{R_2+R_{on}} - \frac{R_2 R_{on}}{R_2+R_{on}} I_{in} = 0. \tag{5.6}$$

Likewise, $V_2$-nullcline is expressed as

$$V_1 - R_2\left(\frac{1}{R_2} + \frac{1}{R_{off}} + \frac{1}{R_L}\right) V_2 + \frac{R_2 V_{dc2}}{R_{off}} = 0, \tag{5.7}$$

if i) $|V_2 - V_{dc2}| \leq |V_{off}|$ or ii) $|V_{off}| < |V_2 - V_{dc2}| < |V_{on}|$ and $|V_2\text{-}V_{dc2}|$ immediately before entering into this voltage region in time was smaller than $V_{off}$, and

$$V_1 - R_2\left(\frac{1}{R_2} + \frac{1}{R_{on}} + \frac{1}{R_L}\right) V_2 + \frac{R_2 V_{dc2}}{R_{on}} = 0, \tag{5.8}$$

if i) $|V_2 - V_{dc2}| \geq |V_{on}|$ or ii) $|V_{off}| < |V_2 - V_{dc2}| < |V_{on}|$ and $|V_2\text{-}V_{dc2}|$ immediately before entering into this voltage region in time was smaller than $V_{on}$.

When $I_{in}$=0, $V_1$ and $V_2$ stay at a stable fixed point ($V_2$=0.044, $V_1$=-0.042) that is indicated in Figure 5.4a. The parameters used in the phase analysis are listed in Table 5.2, which correspond to case β shown in Figure 5.3. Upon the application of a constant current, $V_1$-nullcline rises by $\frac{R_2 R_{S1}}{R_2+R_{S1}} I_{in}$ on the phase plane so that the fixed point moves far in the above-threshold region as shown in Figure 5.4b. Consequently, the ($V_2$, $V_1$) point flows towards the fixed point in due course as seen in Figure 5.4b. The flow encounters the on-switching condition for $S_1$, $V_1 \geq |V_{on}| + V_{dc1} = 0.1$ V, which leads to the emergence of the different $V_1$-nullcline given by Eqation 5.6. As a result, the flow alters the path towards a new fixed point that is again out of the sub-threshold region (see Figure 5.4c). On the way, the flow reaches the off-switching condition for $S_1$, $V_1 \leq |V_{off}| + V_{dc1} = -0.4$ V, leading to the recovery of the sub-threshold $V_1$-nullcline (Equation 5.5), and thus a path change (Figure 5.4d). The path

undergoes another change when it reaches the on-switching condition for $S_2$ $V_2 \leq -|V_{on}| + V_{dc2} = -0.1$ V, as a consequence of emergence of the above-threshold $V_2$-nullcline given by Equation 5.8 (Figure 5.4e). Encountering the off-switching condition for $S_2$, $V_2 \geq -|V_{off}| + V_{dc2} = 0.4$ V recovers the sub-threshold $V_2$-nullcline (Equation 5.7), so that the flow heads to a new fixed point as shown in Figure 5.4f. The subsequent firing dynamics follows the limit cycle that is indicated using a grey line in Figure 5.4f. The spike firing dynamics of the NLIF neuron differs from that of the Hodgkin-Huxley neuron mainly in the fact that a stable fixed point varies upon $V_1$ and $V_2$ on the phase plane as a result of $V_1$- and $V_2$-nullcline that are conditional on $V_1$ and $V_2$.

Notably, the limit cycle is confined in the area ($-|V_{on}| + V_{dc2} \leq V_2 \leq -|V_{off}| + V_{dc2}$ and $|V_{off}| + V_{dc1} \leq V_1 \leq |V_{on}| + V_{dc1}$) on the phase plane as seen in Figure 5.4. That is, the spike's height and the level of the following undershoot are determined by $V_{dc1}$, $V_{dc2}$, $V_{on}$, and $V_{off}$, so that they are important parameters in spike's shape design.

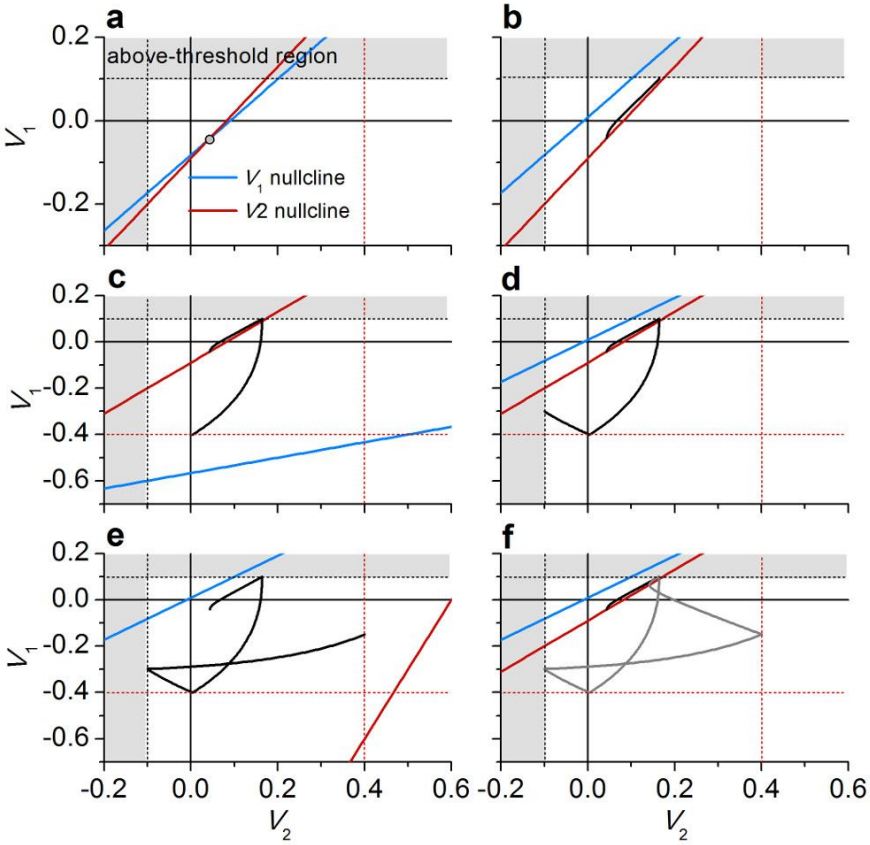


Figure 5.4 Spike firing dynamics on two-dimensional phase plane. (a) $V_1$- and $V_2$-nullcline and a stable fixed point (grey circle) when $I_{in}$=0. The white area denotes the sub-threshold region. (b)-(f) Changes in $V_1$- and $V_2$-nullcline upon threshold switching of $S_1$ and $S_2$ (the consequent changes in a fixed point) and the consequent trajectory of $V_1$ and $V_2$ on the phase plane. The grey cycle in (f) shows the corresponding limit cycle. The black and red dashed lines mean thresholds for on- and off-switching, respectively.

Table 5.2 Parameters used in the neuronal response function and tuning function simulation.

| $R_2$ [Ω] | $R_L$ [Ω] | $R_{on}$ [Ω] | $R_{off}$ [Ω] | $V_{on}$ [V] | $V_{off}$ [V] |
|---|---|---|---|---|---|
| 100 k | 1 G | 1 M | 50 k | 1.0 | 0.5 |
| $V_d$ [V] | $C_1$ [nF] | $C_2$ [nF] | $I_{in}^{max}$ [μA] | $\sigma_s$ [degree] | |
| 0.9 | 7 | 2 | 1 | 30 | |

### 5.2.3. Neuronal selectivity of the NLIF neuron

The circuit parameters of the NLIF neuron are required to be further optimized by taking into account the neuronal selectivity of the NLIF neuron for stimulation. As an information encoder, the NLIF neuron should be able to represent "distinguishable" responses to different stimuli. Neuronal responses are typically parameterized by the spike firing rate or the spike number in a given time period. Regarding the neuronal selectivity, the NLIF neuron needs to vary its firing rate upon input current $I_{in}$. In particular, the firing rate and the input current are expected to be in a one-to-one correspondence relationship. Otherwise, one can hardly estimate the stimulus by counting the number of spikes, implying difficulty in "decoding" neuronal information. This difficulty in decoding consequently reduces the amount of information conveyed by the neuron.[33] In general, a neuronal encoding process is described by $a = G[I_{in}(s)]$, where $a$ and $s$ denote activity and stimulus, respectively. In this study, we define neuronal "activity" denoting the number of spikes in a time period of 30 ms. The function $G$ in a biological neuron is nonlinear and exhibits a threshold value for activation, i.e., firing, of the neuron. This function is often referred to as the neuronal response function in which the activity is determined by input current $I_{in}$.

For cases of aforementioned α, β and γ, the neuronal response functions were simulated in the input current $I_{in}$ range (0–1.0 μA) and they are plotted in Figure 5.5a. The neuronal response functions tend to increase monotonically with input current $I_{in}$ as long as the current is larger than a threshold of approximately 0.25 μA. This threshold results from a threshold voltage for the on-switching of switches $S_1$ and $S_2$ ($V_{on}$). All these functions appear to fulfill the aforementioned requirements for successful neuronal encoding. Nevertheless, a higher $da/dI_{in}$ value is favorable considering the fact that it reduces the uncertainty in discrimination when "noisy" neuronal responses are

decoded. This issue will be revisited later when dealing with the noisy behavior of the NLIF neuron. Thus, case β appears to be most favorable and further discussion in this study will be narrowed down on this particular case. The corresponding parameters are listed in Table 5.2.

In biological neurons, the input current $I_{in}$ is understood to be determined by stimulus $s$, that is, $I_{in}$ is a function of stimulus $s$. Each individual neuron has a preferred stimulus $s_p$, at which $I_{in}$ injected into a given neuron becomes the maximum. Note that this is the case of controlled neurophysiology experiments. The corresponding neuronal in-vivo function works in the way that a sensory neuron transmits a spike train to a postsynaptic neuron, providing time-varying, rather than constant, synaptic current.[1] For simplicity, only one-dimensional stimuli are of concern in this study. For instance, stimulus $s$ can be a one-dimensional visual stimulus such as the orientation angle of a light bar for the primary visual cortex[34, 35] and a wind direction for the cricket cercal system[36]. For convenience, the orientation of a light bar is considered as a one-dimensional stimulus in this study. It is assumed that the input current is described by a Gaussian function whose maximum is placed at preferred stimulus $s_p$ as follows: $I_{in}(s) = I_{in}^{max} exp\left[-0.5\left(s - s_p\right)^2/\sigma_s^2\right]$, where $I_{in}^{max}$ and $\sigma_s$ are the maximum $I_{in}$ and the standard deviation, respectively. Figure 5.5b shows the assumed $I_{in}$ distribution with respect to stimulus, where $I_{in}^{max}$, $s_p$, and $\sigma_s$ are 1 μA, 0°, and 30°, respectively. Entering this $I_{in}(s)$ function into the neuronal response function $G[I_{in}]$ for β eventually gives the tuning curve shown in Figure 5.5c. This bell-shaped tuning curve appears consistent with that obtained for typical biological neurons. The response of the NLIF neuron shows its maximum at an orientation of 0°, corresponding to its preferred orientation, and tails around the preferred orientation. That is, stimuli within an orientation range of approximately –40° to 40° are able to activate the NLIF neuron although they are not exactly

coincident with the preferred orientation. As a matter of fact, this imperfect-looking tuning curve enables a population of neurons with the limited number of preferred orientations to encode continuous, i.e., analog, information.[29] If neurons represented delta-function-like tuning curves, then an infinite number of such neurons would be required for encoding analog orientation information.

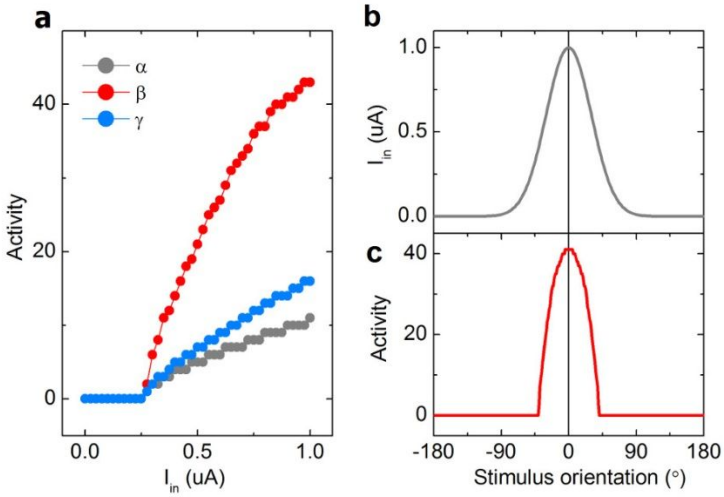


Figure 5.5 Tuning function of ideal NLIF neuron. (a) Neuronal response functions of the NLIF neuron with the three combinations of $C_1$ and $C_2$ (α, β, and γ). (b) A Gaussian distribution of input current $I_{in}$, centered at a preferred orientation of 0°. (c) An ideal tuning curve of the NLIF neuron corresponding to the β case with a preferred orientation of 0°.

### 5.2.4. Noisy NLIF neuron

The tuning curve shown in Figure 5.5c is of a perfectly working NLIF neuron. The orientation information encoded in the neuron can be decoded without uncertainty. Now, an arising question is "how large is the impact of imperfect behavior of the NLIF neuron on neuronal encoding and decoding?" Imperfect behavior is most likely caused by the variability of switching parameters of switches $S_1$ and $S_2$ ($R_{on}$, $R_{off}$, $V_{on}$, and $V_{off}$). For actual experimental NLIF neurons, variations in such parameters cannot be avoided. Thus, an attempt to determine the quantitative uncertainty in processing neuronal information, caused by such variations, was made by evaluating the neuronal encoding and decoding processes with varying switching parameters. Firing each spike in a spike train involves off → on → off switching of each $S_1$ and $S_2$ in a consecutive order. Given that the switching parameters in an experimental switch, in general, varies on each switching cycle[22, 37], it is rather natural to assign different switching parameters to each switch after each spike in the spike train. That is, such a random update of the parameters lasts for an entire spike firing period. In this regard, the switching-event-driven randomness leads to time-varying variability, and thus "noise" rather than heterogeneity.[38] Such variations lead to a change in the inter-spike interval (ISI) while a constant $I_{in}$ is applied for a given time period. Spike firing behavior of the NLIF neuron involving the variation is shown in Figure 5.6. For this simulation, $R_{on}$ and $R_{off}$ of switches $S_1$ and $S_2$ were randomly sampled using Gaussian PDFs centered at 50 kohm and 1 Mohm, respectively, with 10 percent resistance deviation. After each of on- and off-switching events a new resistance was assigned to the switches. The switching-event-driven update therefore lets $R_{on}$ and $R_{off}$ fluctuate over time as shown in Figures 5.6b and d, implying noise rather than heterogeneity.

It should be noted that the nullclines, Equations 5.5-5.8, are determined by $R_{on}$ and $R_{off}$ of $S_1$ and $S_2$, and thus variation in these resistance values essentially alters the nullclines and the corresponding fixed point. Given the switching-event-driven random update of $R_{on}$ and $R_{off}$, the nullclines vary, and thus the trajectory of ($V_2$, $V_1$) on the phase plane varies as well. The spike firing dynamics on the phase plane is shown in Figure 5.6f, corresponding to the time-domain analysis result in Figures 5.6a. In this regard, the noise of the NLIF neuron is distinguished from other noise models for LIF models, e.g. diffusive noise given white noise and/or noisy synaptic current,[39] and for conductance-based model such as Hodgkin-Huxley neuron[40, 41].

The noise characteristics were quantitatively analyzed by examining the relationship between the mean and the variance of the spike number for a time period of 30 ms. The data are plotted in Figure 5.6g. This relationship shows a type of a noise present. For instance, in some biological neurons, this relationship is often given by $\sigma_n^2 = A\langle n\rangle^B$ and $B \approx 1$, where $\sigma_n^2$ and $\langle n\rangle$ denote the variance and the mean of the spike number, respectively.[42] This type of noise is referred to as the Poisson noise because the spike generation satisfies the Poisson process.[1] The Poisson noise results in a linear line whose slope is unity as indicated with the dashed line in Figure 5.6g. As shown in Figure 5.6g, similar to the Poisson noise, the variance increases as the mean spike number increases except that the slope for all four standard deviations is larger than unity (ca. 1.3). The NLIF neuron shows a Poisson-like, rather than perfect Poisson, noise and the variance is larger than the Poisson noise at almost every mean spike number. Interestingly, for the 5 percent deviation case, the variance is much smaller than that of the Poisson neuron at mean spike numbers of approximately 30. This is attributed to the activity limit by the capacitors' charging and discharging times that restricts the integration time for spike firing (see Figure S4 in Supplementary Information).

The stochastic characteristics of this seemingly Poisson-like noise were further confirmed by analyzing the distribution of ISIs and the autocorrelation of the spikes in a given spike train: the results are shown in Figures 5.6h and i, respectively. In Figure 5.6h, the distribution is better fit by a Gamma, rather than exponential, function due to the effective refractory time caused by the finite recharging time of mainly capacitor $C_1$.[1] The evaluated autocorrelation data, shown in Figure 5.6i, show typical delta-function-like distribution, suggesting no correlation between spikes in a given spike train. These noise analyses, therefore, identify Poisson-like noise characteristics of the observed noise.

To achieve successful spike firing, the standard deviations of the switching parameters should be confined within particular ranges. Mostly, failure of spike firing takes place when switch $S_2$ becomes stuck to its on-state and high membrane potential ($V_2$) is maintained. Typical examples of successful spike firing and failure cases are seen in Figures 5.7c and 5.7d. Insomuch as switch $S_2$ keeps its on-state in case of failure, the membrane potential remains high, so that no further switching of switch $S_1$ occurs. The duration time of current application was 30 ms. The number of successful spike firing events was evaluated with separately varying the standard deviation of each switching parameter to determine its tolerance limit. The results are shown in Figures 5.7e-h. We varied input current $I_{in}$ (0.4, 0.6, 0.8, and 1.0 μA) so as to investigate its effect on success in spike firing. The tolerance for parameter variations differs; the tolerance limits for variations in $R_{on}$ and $R_{off}$ reach up to approximately 30 percent whereas the limit for variation in $V_{\mathrm{off}}$ is less than 20 percent as shown in Figures 5.7e-h. It should be noted that the current duration time raises the failure probability as the "$R_{\mathrm{on}}$-stuck" event can indeed occur with an increase in the number of switching events during the duration of input current. Thus, the longer the duration of current application, the lower the probability of successful firing at a given deviation.

The switching parameters were chosen in a random manner by employing a Gaussian probability density function (PDF) with particular standard deviations. The means of these distributions were placed at the values used in the calculation of the perfect tuning curve in Figure 5.5c ($R_{on}$: 50 kohm, $R_{off}$: 1 Mohm, $V_{on}$: 1 V, and $V_{off}$: 0.5 V, the other parameters are shown in Table 5.2). The encoding process of a noisy individual NLIF neuron was evaluated by calculating its tuning curve based on statistics. $R_{on}$ and $R_{off}$ simultaneously varied at different standard deviations and the mean activity at each orientation was obtained out of 100 trials. Given the very limited tolerance for $V_{on}$ variation, no variation in $V_{on}$ was taken into account. The calculated tuning curves for four different deviations (5, 10, 20, and 30 percent) are shown in Figure 5.8. The maximum activity tends to decrease with increasing standard deviation and unexpected spike firing events also take place, in particular, at orientations out of a range of approximately –40° to 40°. Unlike the ideal tuning curve in Figure 5.5c, a one-to-one correspondence relationship between orientation and activity is no longer satisfied. Therefore, a significant difficulty in decoding the neuronal information arises, consequently reducing the amount of information conveyed by the noisy neuron.[33]

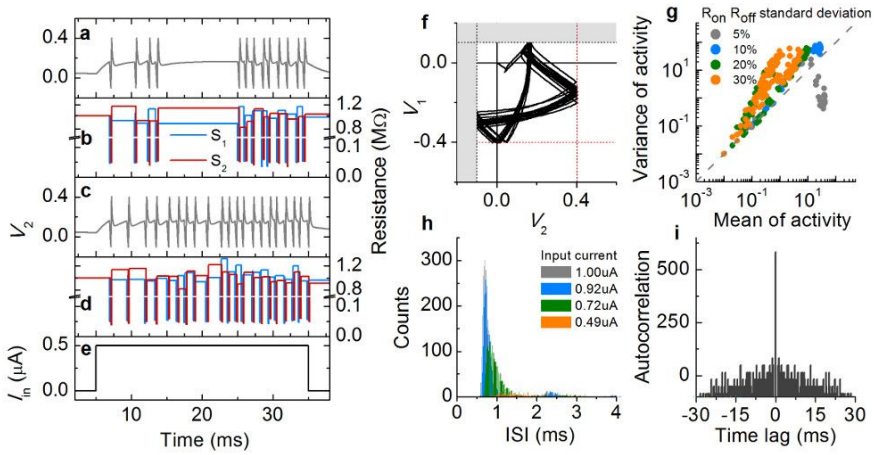


Figure 5.6 Poisson-like noise of NLIF neuron. (a) Noisy response of the NLIF neuron with 10 percent resistance deviation and (b) the corresponding fluctuation of resistance of TSs in time. (c) Another set of noisy response and (d) resistance fluctuation under the same condition. The input current is plotted in (e). (f) Spike firing dynamics mapped onto the phase plane for the dynamics shown in (a). (g) Variance of activity with respect to mean activity for the four different resistance deviations (5, 10, 20, and 30 percent). (h) ISI distribution for case of 10 percent of resistance deviation at given four different $I_{in}$ values (1.00, 0.92, 0.74, and 0.49 μA). (i) Autocorrelation of spikes in a train. The NLIF neuron, allowing 10 percent of resistance deviation, was subject to 0.5 μA.

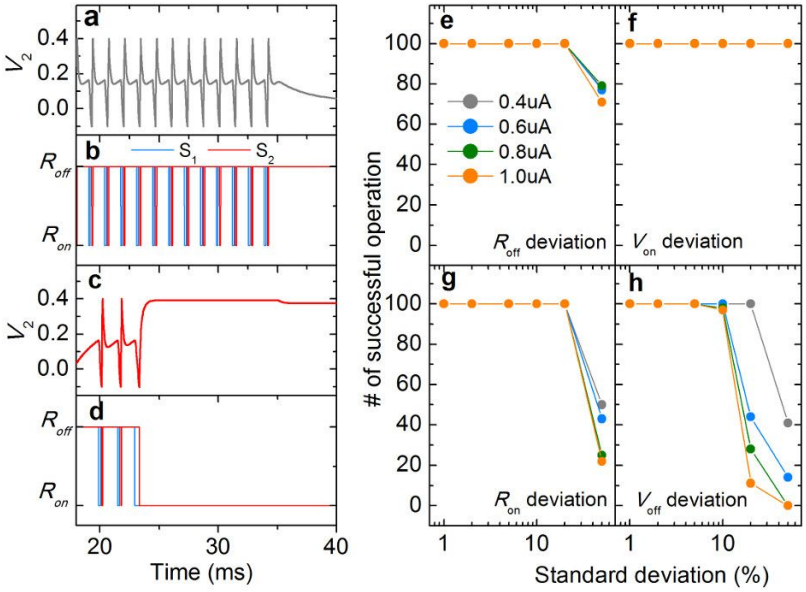


Figure 5.7 Failure of spike firing. (a) Successful spike firing example and (b) the corresponding variation of resistance of TSs. (c) Evolution of membrane potential in time in case of failure and (d) the corresponding change of resistance of TSs. This failure arises from switch $S_2$ stuck to its on-state. The number of successful spike firing events on 100 trials is evaluated at given standard deviation of each switching parameter while the other parameters are fixed: (e) $R_{off}$, (f) $V_{on}$, (g) $R_{on}$, and (h) $V_{off}$. The evaluation was done at four different input currents (0.4, 0.6, 0.8, and 1.0 μA)

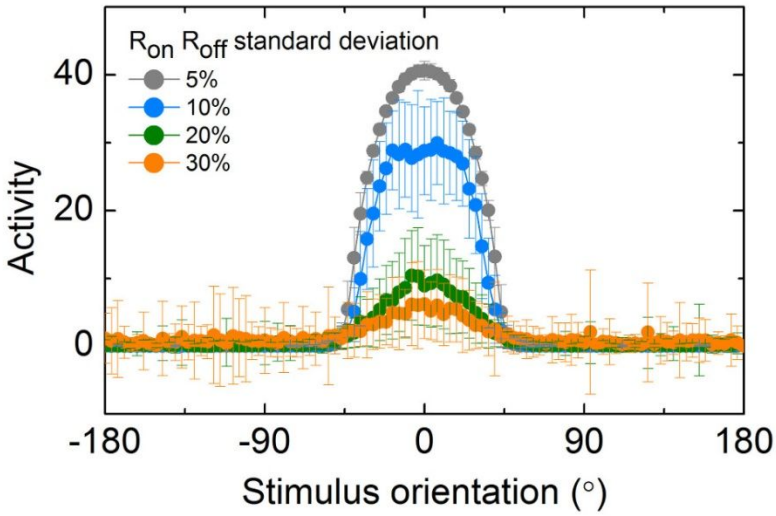


Figure 5.8 Variability effect on tuning function. Poisson-like-noise-including tuning curves of the NLIF neuron allowing 5, 10, 20, and 30 percent of resistance deviation.

### 5.2.5. Representation of a population of NLIF neurons

The noise in the individual NLIF neuron seems to be an obstacle to appropriate neuronal information processing because of the difficulty in decoding caused by the noise. Fortunately, neuronal information processing in the brain does not strongly rely on individual neurons; instead, the task is in general performed by a population of individual neurons.[29, 33, 43] Nevertheless, neuronal noise can still contaminate the population response. Some types of correlations between neurons in a population are known to reduce errors to some extent[33], but this does not seem to be the general case. A possible answer to the question "how do brains as groups of unreliable (noisy) neurons work reliably?" is that populations of neurons may encode and decode "probability distributions" rather than particular values.[44-46] In other words, encoding and decoding are viewed as processes retuning probability distributions over all possible values: response and stimulus distributions for encoding and decoding, respectively. Especially, decoding is most likely based on a statistical inference process, in particular, Bayesian inference.[28, 45, 47, 48] In fact, some psychophysical evidence for Bayesian inference have been found in, for instance, contrast-depending velocity perception.[45, 49] Given the role of the NLIF neuron in either hardware-based or *in silico* systems, it is then an important task to examine the NLIF neuron as a Bayesian decoder, quantitatively evaluating probability distributions over the orientation at given degrees of variability of the switching parameters.

According to the Bayes' rule, a posterior PDF $P[s|r]$ is given by the product of the likelihood function $P[r|s]$ and the prior PDF $P[s]$:

$$P[s|r] = P[r|s] \cdot P[s]/P[r], \tag{5.9}$$

where $s$ and $r$ denote stimulus and response, respectively. The notation $P[B|A]$ means the conditional probability of event $B$, given event $A$; the likelihood function $P[r|s]$ denotes the probability of observing response $r$,

given stimulus $s$. This function describes the variability of the response to a particular stimulus. Likewise, the posterior PDF $P[s|r]$ means the probability of stimulus $s$, given observation of response $r$. Insomuch as no condition is imposed on the prior and the response PDF, $P[s]$ and $P[r]$ are constant in ranges of stimulus $s$ and response $r$, respectively. Thus, the posterior can be evaluated if the likelihood is known; the maximum of the posterior PDF corresponds to the most probable stimulus $s$ estimated from the response observations. That is, the observed neuronal responses can be decoded in terms of probability. Note that $P[r|s]/P[r]$ denotes the normalized likelihood PDF.

Unfortunately, the NLIF neuron representing a Poisson-like noise does not allow an analytical description of its likelihood function unlike Poisson neurons.[1] The only way to obtain the likelihood is collecting the responses of a population of NLIF neurons statistically, given various stimuli acting on it. Statistics were made on 20 NLIF neurons of 20 different preferred stimuli $s_p$ that are homogeneously distributed in the orientation range −180° to 180°. Now, the response $r$ is a vector quantity $\vec{r}$ of 20 components: $\vec{r} = (r_1, r_2, r_3, \cdots, r_{20})$. The tuning curves of these 20 neurons on the assumption of no noise are shown in Figure S5 in Supplementary Information. No correlations between neighboring neurons are assumed and the firing event on each neuron is regarded to be independent, allowing the following simple calculation:

$$P(\vec{r}|s) = \prod_{i=1}^{20} P(r_i|s). \tag{5.10}$$

The likelihood function was acquired by repeating spike number evaluation over 1000 times at each stimulus $s$ and 300 stimuli were sampled between −180° and 180°. Given Equations. 5.9 and 5.10 and the constant PDFs $P[s]$ and $P[r]$, the posterior PDF satisfies the condition $P(s|\vec{r}) \propto \prod_{i=1}^{20} P(r_i|s)$. Thus, we can evaluate the probability of population representation of a particular pattern $\vec{r}$ when subject to a given stimulus $s$. We snapshotted $\vec{r}$

patterns of the population of NLIF neurons with resistance deviations of 5, 10, 20, and 30 percent at a stimulus of 0°, and the patterns are plotted in Figures 5.9a, 5.9b, 5.9c, and 5.9d, respectively. The different preferred orientations of the population let a few neurons preferring stimuli in the vicinity of 0° be activated despite the noise complicating the patterns.

Finally, the aforementioned Bayesian decoding was done for the patterns, leading the posterior PDFs shown in Figures 5.9e, 5.9f, 5.9g, and 5.9h, respectively. The posterior PDFs are more or less noisy showing data scattering; the larger the deviation, the larger the data scattering. This data scattering is also a matter of population size, i.e., the more neurons in the population, the less decoding error. Given a large increase in calculation time with increasing the number of neurons in the population, we placed 20 neurons in the population; however, the Bayesian decoding of larger population sizes definitely enables correct estimation. The calculated posterior PDFs were fitted using Gaussian PDFs so as to evaluate the center and standard deviation of each posterior PDF. As can be seen in Figure 5.9, the center of each PDF is found to be placed around 0°. This revealed that this Bayesian decoder most likely give a correct answer and a correct inference will be made if made by means of the Bayes' rule despite the present Poisson-like noise. Nevertheless, note that statistics cannot be free from error in any cases so that the Bayesian decoding can give a wrong answer at times. Besides, it turns out that the standard deviation in the decoding becomes larger as increasing the variability of $R_{on}$ and $R_{off}$ of the TSs (see Figure 5.9i).

The Bayesian decoding results were compared with the case of populations of Poisson neurons. The likelihood PDF as well as the posterior PDF of a population of independent Poisson neurons is given by a closed-form expression; an increase in the number of Poisson neurons in the population leads to a posterior PDF of a Gaussian form.[28] At a given stimulus, the likelihood PDF of each independent Poisson neuron was analytically

calculated with similar activity as that of the NLIF neuron at the same stimulus. As a result, the posterior PDF of a population of Poisson neurons with the four resistance deviations could be obtained from the population response patterns $\vec{r}$ shown in Figures 5.9a, 5.9b, 5.9c, and 5.9d; the calculated PDFs are plotted using dashed lines in Figures 5.9e, 5.9f, 5.9g, and 5.9h, respectively. In fact, the 20 Poisson neurons already provide a Gaussian PDF as shown in the figures. In comparison with the population of Poisson neurons, it is noticed that the Poisson-like NLIF neurons represent smaller maxima and larger deviations than the Poisson neurons under the same condition except the case of 5 percent deviation of TSs' resistance (see Figure 5.9a). A difference in the standard deviation of the posterior PDF between the NLIF neurons and the Poisson neurons is observed in Figure 5.9i. The larger uncertainty deviation of the Bayesian decoding for the NLIF neurons arises from the larger deviation of activity of the NLIF neuron than that of a Poisson neuron as shown in Figure 5.6g. Likewise, the larger maximum of posterior PDF of the NLIF neurons in Figure 5.9e than the Poisson neurons is understood in terms of the smaller variance of activity at 5 percent deviation of TSs' resistance at the high mean activities, shown in Figure 5.6g. The smaller variance is attributed to the activity limit by charging and discharging of the capacitors.

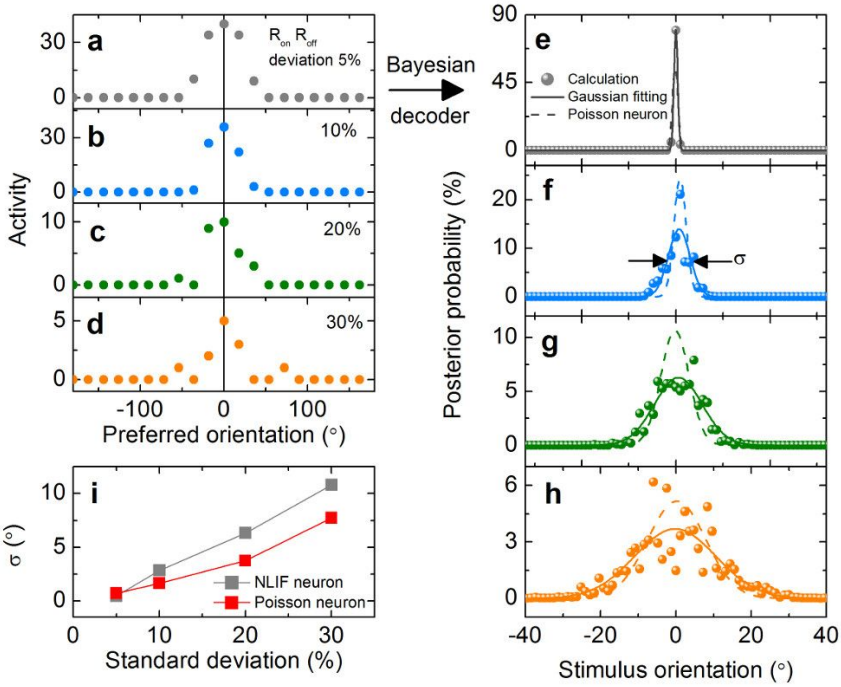


Figure 5.9 Bayesian decoding of population representation of NLIF neurons. Snapshotted activity patterns of a population including 20 NLIF neurons for (a) 5, (b) 10, (c) 20, (d) 30 percent resistance deviation cases at a stimulus of 0°. The results of the Bayesian decoding, i.e., posterior PDFs, for the patterns are shown in (e), (f), (g), and (h), respectively. The acquired posterior PDFs are compared with those of a population of 20 Poisson neurons (dashed lines). The standard deviations $\sigma$ of the posterior PDFs of the Poisson-like NLIF neurons for the different resistance deviations are shown in (i) in comparison with those of the Poisson neurons.

## 5.3. Discussions

The NLIF neuron studied in this work can serve as a prototypical *in silico* neuron model exhibiting a Poisson-like noise. The circuitry is simple and perhaps easy enough to be implemented in large-scale ANNs. In particular, as a result of this study, it is understood that the variability of the TSs' resistance leads to such a Poisson-like noise that the noise behavior of this prototypical *in silico* neuron needs to be under control and appropriately designed to meet the noise behavior required for ANNs built for specific purposes.

Nevertheless, when it comes to hardware realization of such NLIF neurons, there are several practical obstacles that should be overcome to realize the goal. What is of significant importance in the Poisson-like NLIF neuronal behavior is the minimum variability of $V_{on}$ of the TS in the NLIF neuron. As discussed earlier, the tolerance limit of $V_{on}$ is merely a few percent unlike that of the other switching parameters, i.e., $R_{on}$, $R_{off}$, and $V_{off}$. Thus, "reliability" of this unreliable neuron requires meeting this stringent requirement for ensuring reliable operation. Apart from this restriction, other requirements discussed earlier may be satisfied by appropriate choices of TS materials, systems, and their design. Another important issue that potentially hinders practical use of this type of neuron is the long-term reliability of switches $S_1$ and $S_2$, which are subject to the relatively high dc-voltage stress ($V_{dc1}$ and $V_{dc2}$). The dc voltages allow active operation of the NLIF neuron, working as effective power suppliers. Regarding the limit cycle confined in the area ($-|V_{on}| + V_{dc2} \leq V_2 \leq -|V_{off}| + V_{dc2}$ and $|V_{off}| + V_{dc1} \leq V_1 \leq |V_{on}| + V_{dc1}$) on the phase plane (see Figure 5.4), in order to realize spike firing at low $I_{in}$, dc voltages close to, but smaller than, $V_{on}$ need to be applied to switches $S_1$ and $S_2$, and thus the consequent electrical stress most likely affects the switches adversely. Eventually, it most likely leads to dielectric breakdown when a dielectric layer is in use as a TS material. This issue is also directly related to a high power

consumption problem. The constant application of dc voltages during the lifetime of the NLIF neuron gives rise to severe power consumption, which is definitely against one of the inherent advantages of neuromorphic systems over standard digital systems, i.e., low power consumption. Therefore, addressing these significant problems properly accelerates practical use of such NLIF neurons in hardware-based neuromorphic systems.

## 5.4. Conclusions

The most crucial conclusion drawn from this study is that the potential variability of behavior of the TS is allowed up to a certain level as long as the Bayesian decoder is able to discriminate the encoded information correctly. In addition, the uncertainty, i.e., standard deviation, of the posterior PDF shrinks when introducing a larger number of NLIF neurons in the population. In general, the statistical accuracy of a survey increases with the number of samples. Thus, the uncertainty of posterior and likelihood of individual NLIF neurons is compensated by the increase in accuracy. An increase in the number of neurons in the population, therefore, tolerates a larger variability of switching parameters of the TSs. Nevertheless, confining the variability within a tolerance range is still of significant importance, especially confining that of $V_{on}$.

## 5.5. Bibliography

[1] P. Dayan, L. F. Abbott, *Theoretical Neuroscience*, The MIT Press, Cambridge, MA, USA 2001.

[2] C. Eliasmith, C. H. Anderson, *Neural Engineering*, The MIT Press, Cambridge, MA, USA 2004.

[3] W. Gerstner, W. M. Kistler, *Spiking Neuron Models: Single Neurons,*

*Population, Plasticity*, Cambridge University Press, Cambridge, UK 2002.

[4] S. H. Seung, *Connectome: how the brain's wiring makes us who we are*, Houghton Mifflin Harcourt, Boston, MA, USA 2012.

[5] C. Eliasmith, T. C. Stewart, X. Choo, T. Bekolay, T. DeWolf, C. Tang, D. Rasmussen, *Science*, 338, 1202 (2012).

[6] G. Hinton, P. Dayan, B. Frey, R. Neal, *Science*, 268, 1158 (1995).

[7] Y. LeCun, K. Kavukcuoglu, C. Farabet, "Convolutional networks and applications in vision", presented at *Circuits and Systems (ISCAS), Proceedings of 2010 IEEE International Symposium on*, May 30 2010-June 2 2010, 2010.

[8] H. Markram, *Nat. Rev. Neurosci.*, 7, 153 (2006).

[9] C. Mead, *Proc. IEEE*, 78, 1629 (1990).

[10] P. Merolla, J. Arthur, F. Akopyan, N. Imam, R. Manohar, D. S. Modha, "A digital neurosynaptic core using embedded crossbar memory with 45pJ per spike in 45nm", presented at *Custom Integrated Circuits Conference (CICC), 2011 IEEE*, 19-21 Sept. 2011, 2011.

[11] A. Danchin, C. Médigue, O. Gascuel, H. Soldano, A. Hénaut, *Res. Microbiol.*, 142, 913 (1991).

[12] A. L. Hodgkin, A. F. Huxley, *J. Physiol.*, 117, 500 (1952).

[13] E. M. Izhikevich, *IEEE Trans. Neural Networ.*, 14, 1569 (2003).

[14] E. M. Izhikevich, *IEEE Trans. Neural Networ.*, 15, 1063 (2004).

[15] M. D. Pickett, G. Medeiros-Ribeiro, R. S. Williams, *Nat. Mater.*, 12, 114 (2012).

[16] H. D. Crane, *Proc. IRE*, 50, 2048 (1962).

[17] N. F. Mott, *Proc. Phys. Soc. Sect. A*, 62, 416 (1949).

[18] L. Cario, C. Vaju, B. Corraze, V. Guiot, E. Janod, *Adv. Mater.*, 22, 5193 (2010).

[19] D. S. Jeong, R. Thomas, R. S. Katiyar, J. F. Scott, H. Kohlstedt, A. Petraru, C. S. Hwang, *Rep. Prog. Phys.*, 75, 076502 (2012).

[20] M. D. Pickett, R. S. Williams, *Nanotechnology*, 23, 215202 (2012).

[21] H.-W. Ahn, D. S. Jeong, B.-k. Cheong, S.-d. Kim, S.-Y. Shin, H. Lim, D. Kim, S. Lee, *ECS Solid State Lett.*, 2, N31 (2013).

[22] D. S. Jeong, H. Lim, G.-H. Park, C. S. Hwang, S. Lee, B.-k. Cheong, *J. Appl. Phys.*, 111, 102807 (2012).

[23] M. J. Lee, D. Lee, S. H. Cho, J. H. Hur, S. M. Lee, D. H. Seo, D. S. Kim, M. S. Yang, S. Lee, E. Hwang, M. R. Uddin, H. Kim, U. I. Chung, Y. Park, I. K. Yoo, *Nat. Commun.*, 4, 2629 (2013).

[24] S. R. Ovshinsky, *Phys. Rev. Lett.*, 21, 1450 (1968).

[25] J. W. Han, Y. K. Choi, *Symp. VLSI Technol., Dig. Tech. Pap.*, 171 (2010).

[26] X. Liu, S. M. Sadaf, M. Son, J. Shin, J. Park, J. Lee, S. Park, H. Hwang, *Nanotechnology*, 22, (2011).

[27] S. Deneve, P. E. Latham, A. Pouget, *Nat. Neurosci.*, 2, 740 (1999).

[28] W. J. Ma, J. M. Beck, P. E. Latham, A. Pouget, *Nat. Neurosci.*, 9, 1432 (2006).

[29] A. Pouget, P. Dayan, R. Zemel, 1, 125 (2000).

[30] D. S. Jeong, I. Kim, M. Ziegler, H. Kohlstedt, *RSC Adv.*, 3, 3169 (2012).

[31] R. FitzHugh, *Biophys. J.*, 1, 445 (1961).

[32] J. Nagumo, S. Arimoto, S. Yoshizawa, *Proc. IRE*, 50, 2061 (1962).

[33] B. B. Averbeck, P. E. Latham, A. Pouget, 7, 358 (2006).

[34] D. H. Hubel, T. N. Wiesel, *J. Physiol.*, 195, 215 (1968).

[35] G. H. Henry, B. Dreher, P. O. Bishop, *J. Neurophysiol.*, 37, 1394 (1974).

[36] F. E. Theunissen, J. P. Miller, *J. Neurophysiol.*, 66, 1690 (1991).

[37] M.-J. Lee, D. Lee, S.-H. Cho, J.-H. Hur, S.-M. Lee, D. H. Seo, D.-S. Kim, M.-S. Yang, S. Lee, E. Hwang, M. R. Uddin, H. Kim, U. I. Chung, Y. Park, I.-K. Yoo, 4, 2629 (2013).

[38] T. J. Hamilton, S. Afshar, A. van Schaik, J. Tapson, *Proc. IEEE*, 102, 843 (2014).

[39] N. Brunel, F. Chance, N. Fourcaud, L. Abbott, 86, 2186 (2001).

[40] B. Gutkin, J. Jost, H. Tuckwell, *Naturwissenschaften*, 96, 1091 (2009).

[41] H. C. Tuckwell, J. Jost, 6, e1000794 (2010).

[42] W. H. Calvin, C. F. Stevens, *Science*, 155, 842 (1967).

[43] C. Eliasmith, C. H. Anderson, *Neural Engineering: Computation, Representation, and Dynamics in Neurobiological Systems*, MIT Press, Cambridge, MA 2003.

[44] C. Anderson, *Computational Intelligence Imitating Life*, IEEE Press, New York 1994.

[45] A. Pouget, P. Dayan, R. S. Zemel, 26, 381 (2003).

[46] Y. Weiss, D. J. Fleet, *Velocity Likelihoods in Biological and Machine Vision. In Statistical Theories of the Cortex*, MIT Press, Cambridge, MA 2002.

[47] D. C. Knill, W. Richards, *Perception as Bayesian Inference*, Cambridge Univ. Press, New York 1996.

[48] D. C. Knill, A. Pouget, *Trends Neurosci.*, 27, 712 (2004).

[49] Y. Weiss, E. P. Simoncelli, E. H. Adelson, *Nat. Neurosci.*, 5, 598 (2002).

# 6. Relaxation oscillator-realized leaky integrate-and-fire neuron

## 6.1. Introduction

To date, several prototypical neuron models have been proposed, which are mostly on the basis of integrate-and-fire behavior, for instance, the Axon-Hillock neuron,[1, 2] NLIF neuron,[3, 4] conductance-based neuron,[5, 6] and Izhikevich neuron models.[7, 8] Each model remarks neuronal behavior to within different accuracy. With that said, they should feature essential neuronal behaviors that play key roles in neuronal representation such as LIF behavior, gain function, and autocorrelated, i.e. random, neuronal noise.[4]

Towards this end, in this study we propose a spiking neuron model, based on a relaxation oscillator, and term it as a relaxation oscillator-based leaky integrate-and-fire (ROLIF) neuron. The ROLIF neuron model likely satisfies the aforementioned basic requirements for a hardware spiking neuron. We made use of a Pearson-Anson oscillator (PAO) – utilizing a TS based on amorphous higher chalcogenide – as a relaxation oscillator. A pair of the relaxation oscillator and *non-ideal* operational amplifier (op-amp) realizes the ROLIF neuron. Note that the op-amp is non-ideal considering the coupling between the input impedance of the op-amp and the adjacent circuit element, which is negligible in an *ideal* one. Neuronal noises in the ROLIF neuron – stemming from switching event-driven variability in threshold switching parameters – were experimentally addressed. This study covers a pair of ROLIF neurons in connection through a synapse in order to take into account synaptic transmission between them. Finally, the feasibility of more synaptic connections among ROLIF neurons was identified by simulating a small network of ROLIF neurons and synapses. An empirical formula of

spatial synaptic integration within the network was consequently acquired. In addition, a role of random neuronal noise in synaptic transmission is addressed. Hereafter, for simplicity 'neuron' refers to the ROLIF neuron unless otherwise stated.

## 6.2. Experimental

***Pearson-Anson oscillation characterization*:** The PAO encompassing the TS was characterized by applying a square voltage pulse using an Agilent 81110A PG and recording the response using a Tektronix TDS5104 oscilloscope. The recorded results revealed oscillation frequency of the PAO in terms of the number of spikes at the given pulse duration.

***Synaptic transmission characterization*:** A pair of the PAO and commercial LT1007 op-amp eventually realized an individual neuron – its neuronal behavior was identified in a pair of neurons, being connected through a synaptic resistor, by applying the same measurement method as for the PAO. All circuit parameters used in the measurements are listed in Table 6.1.

***Time-dependent circuit calculation***: The neuron circuit was generalized to instances of various non-ideal op-amps that feature different gains and slew rates. Feasible neuronal behaviors of such neurons were justified by means of circuit simulations. Towards a practical context, a single postsynaptic neuron in connection to many presynaptic neurons was theoretically taken into account and the proof-of-concept demonstration of unidirectional synaptic transmission through a simple synaptic resistor was followed. The variability in threshold switching was realized by randomly updating switching parameters ($R_{off}$, $R_{on}$, $V_{on}$, and $V_{off}$) for every switching event. Each parameter was normalized to have the experimental mean (52 MΩ, 1.5 kΩ,

3.5 V, and 1.1 V for $R_{off}$, $R_{on}$, $V_{on}$, and $V_{off}$, respectively) and standard deviation 5% of each mean.

Table 6.1 Parameters used in the measurements and calculations.

| $R_1$ [kΩ] | $R_2$ [kΩ] | $R_{load}$ [kΩ] | $R_{osc}$ [Ω] | $R_{amp1}$ [kΩ] | $C_1$ [pF] | $C_P$ [pF] |
|---|---|---|---|---|---|---|
| 50 | 1 | 1 | 50 | 1 | 10 | 10 |

## 6.3. Results

### 6.3.1. Equivalent circuit for neuron

To begin, it is worth listing important characteristics of biological neurons, which were implemented in our neuron: neuronal gain function, signal amplification, unidirectional synaptic transmission, and neuronal random noise.[9, 10] (i) The neuron was designed to enable the injective encoding of analog input into activity (output) without noise. That is, a single neuron is able to encode large bits unlike above-threshold-working transistors. Various input, e.g. synaptic current, values ideally evoke distinguishable output neuronal activities, so that the input quantity is successfully estimated from the output activity. This relation between synaptic current and activity is often referred to as gain function that is the substrate of a neuronal tuning function.[11] (ii) The biological neuron spontaneously produces and stores energy on its lipid membrane due to the ion pumps embedded in the membrane – this spontaneous energy storage makes the neuron electrically *active*.[12, 13] Projecting this feature onto its electrical replica, the neuron should be able to amplify spikes so that large attenuation of spikes merely within neighboring neurons can be prevented. (iii) Neighboring neurons communicate with each other by means of spikes that are transmitted through synapses. Chemical synapses – that are believed to render unique functionalities of the mammalian brain, e.g. memory and learning, possible – allow unidirectional synaptic transmission only from the pre to the postsynaptic neuron. In this regard, spiking postsynaptic neurons should not alter the membrane potential of the presynaptic neurons. (iv) Neuronal noise was realized on the substrate of variability in the switching parameters of the TS. Such variability alters the ISI in a spike burst, and thus neuronal activity that refers to the number of spikes in a given time period.

Figure 6.1 depicts the equivalent circuit of the ROLIF neuron. The input and output voltages are denoted by $V_{in}$ and $V_{out}$, respectively; $V_{out}$ corresponds to the membrane potential of the neuron. In connection of a pair of neurons through a synapse, $V_{out}$ of the presynaptic neuron is relayed to $V_{in}$ of the postsynaptic neuron via the synapse. The neuron consists of a non-ideal op-amp (grey dashed line) and PAO (orange dashed line) in Figure 6.1. Particular emphasis is placed on the non-ideality of the op-amp – parameterized by slew rate – as it likely becomes prominent in practice.

The aforementioned key features of the biological neuron are implemented in these two simple components. The non-ideal op-amp enables active operation in light of gain $G$ of the non-inverting op-amp, $G=1+R_{amp2}/R_{amp1}$. Thus, attenuated spikes along *passive* synapses can be re-amplified through the op-amp. Provided the very small output resistance on the op-amp, a change in $V_1$ in Figure 6.1 unlikely affects the behavior of the op-amp. Spike back-propagation is therefore hindered by the neuron itself. In addition, the op-amp in an individual neuron helps the individual neuronal behavior remain unchanged on the network level. Particularly, many presynaptic neurons connected to a postsynaptic neuron in parallel lead to a negligible change in the behavior of the postsynaptic neuron given the very high input resistance of the op-amp. The PAO is in charge of spiking in response to $V_{in}$, producing different spiking activities. That is, the PAO contributes to encoding the input voltage into spiking activity. Notably, the TS in the PAO exhibits switching event-driven variations in switching parameters and the resulting neuronal noise. It is noted that in Figure 6.1 a voltage, rather than a current, is taken as input, which allows a more intuitive understanding of the neuron.

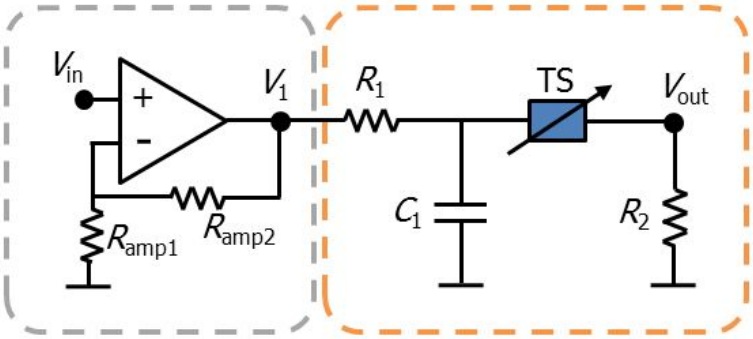


Figure 6.1 Equivalent circuit of the ROLIF neuron. The grey and orange boxes indicate a non-ideal op-amp and PAO, respectively.

### 6.3.2. Pearson-Anson oscillator

The PAO was built on the basis of the TS as illustrated in the inset of Figure 6.2c. Conditional on $V_{in}$, $V_{out}$ oscillates upon the threshold switching in conjunction with capacitor $C_1$ that significantly slows down a change in $V_{TS}$. $V_{out}$ is shown in Figure 6.2a, which was triggered by two different $V_{in}$'s (3.6 and 4.3 V) plotted in Figure 6.2b. Notably, the observed behaviors resemble the membrane potential of a spiking neuron, which in fact underlies spiking in the neuron. Provided that each spike in the oscillation is evoked by a single threshold switching cycle as for the NLIF neuron,[4] the seeming spike bursts at 3.6 and 4.3 V in Figure 6.2b involved four and ten switching cycles, respectively. A rapid rise in $V_{out}$ arises from the on-switching, and the consequent high $V_{out}$ immediately vanishes away upon the imminent off-switching. Thus, $V_{out}$ at the base level between neighboring spikes implies the TS in the off-state.

The number of spikes in a given time period parameterizes spiking activity $a$. The activity tends to increase with $V_{in}$ as already seen in Figure 6.2a. To highlight this, we further identified a change in the number of spikes upon $V_{in}$, providing the relationship shown in Figure 6.2c. First, there exists a threshold voltage for spiking (ca. 3.5 V) – determined by $V_{on}$. At $V_{in}$ below this threshold, $V_{TS}$ crossing $V_{on}$ remains out of reach so that no spiking is evoked. Second, the number of spikes gradually rises with $V_{in}$ in a wide $V_{in}$ range. This change in spike number is attributed to a decline in the ISI – corresponding to recharging time of $C_1$ – with $V_{in}$. The charging leads to $V_{TS}$ evolution in due course towards $V_{on}$. Therefore, the higher $V_{in}$ is given, the shorter time is required for recharging, so is for reaching $V_{on}$. Third, the activity is saturated at high $V_{in}$ (> ca. 5.2 V). The capacitor's charging and discharging as well as the kinetics of the threshold switching is in need of non-vanishing time.[14] Thus, this minimally required time delimits the

minimum ISI, i.e. maximum spike number.

The above-mentioned characteristics of the PAO offer notable similarities to the gain function of the biological neuron, encoding the analog-type input into output (activity) that is likewise analog. Nevertheless, there exist disparities such as an input type; the oscillation of the PAO in Figure 6.2 was triggered by input voltage dissimilarly to biological neuron whose membrane potential is generally perturbed by current rather than voltage. However, applying a current to the PAO barely causes a dramatic change in the neuronal behavior albeit different in detail. Provided that either input type seldom alters the essential features of the gain function-like behavior, chosen is the one suitable for operation in combination with artificial synapses. Later, the proof-of-concept demonstration of the neuron is done on a pair of neurons – connected through a synaptic resistor.

Each spike is evoked by a single threshold switching cycle, and the switching parameters vary upon each cycle. Considering that the ISI means a time required for $V_{TS}$ elevation up to $V_{on}$, the variation of the ISI ahead of each spike is inevitable. The main reason is a variability in $V_{on}$; the higher $V_{on}$, the longer the required ISI. The variability of the parameters therefore is the direct cause of the neuronal random noise. We set aside these noise characteristics until a pair of neurons – in connection through a synapse – are addressed in Section 6.3.5.

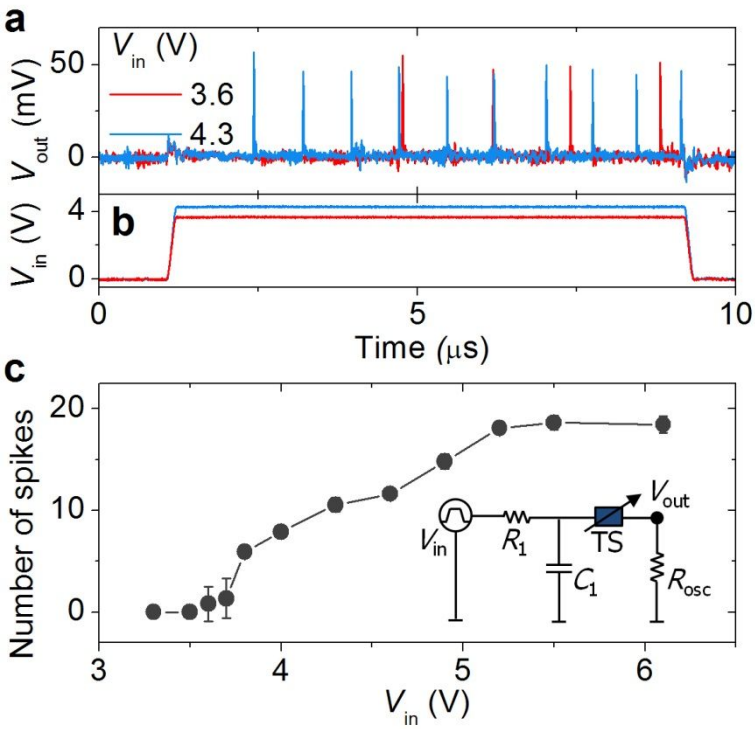


Figure 6.2 (a) Oscillating outputs of the PAO under square voltage pulses in (b). (c) A change in the number of spikes with the height of a voltage pulse applied to the PAO circuit in the inset. The average dataset was obtained out of 20 trials.

### 6.3.3. Non-ideal op-amp

The *non-ideal* op-amp in the neuronal circuit in Figure 6.1 enables spike amplification and unidirectional synaptic transmission. The non-ideality of concern encompasses finite input impedance $Z_{in}$ – described by $C_{in}$ and $R_{in}$ in parallel – and output resistance $R_{out}$ as shown in Figure 6.3a. This non-ideality is almost unavoidable in practice. In the ideal op-amp, $Z_{in}$ and $R_{out}$ are infinite (real) and zero, respectively. The complex $Z_{in}$ due to non-zero $C_{in}$ offers coupling between the op-amp and $R_{syn}$, causing RC delay in $V_{in}$. We make active use of this non-zero $C_{in}$ so as to realize synaptic transmission and the consequent excitatory postsynaptic potential (EPSP). These non-ideal features, however, do not remarkably degrade the aforementioned roles of the op-amp. For instance, unless $R_{out}$ is larger than or comparable to the following resistance in total, e.g. $R_1 + R_{TS} + R_2$ in Figure 6.3a, the op-amp only allows unidirectional synaptic transmission.

Alongside finite $R_{in}$ and $R_{out}$, the non-ideality includes a finite slew rate (a measure of the response rate to input).[15] The larger the slew rate, the more immediately $V_1$ responses to $V_{in}$. A low slew rate lets the op-amp work as a filtered amplifier (cutting off high $dV_{in}/dt$), and thus smoothing $dV_1/dt$ and reducing the actual gain.[15] Thus, such a low slew rate notably distorts output $V_1$ in comparison with input $V_{in}$. Figure 6.3b displays the output of the op-amp (LT1007) with an input spike train (Figure 6.3c) that was elicited from the PAO ahead. Indeed, a comparison between the input and output elucidates such a distortion attributed to a low slew rate. The output response rate of the non-ideal op-amp is given by the following differential equation[15]:

$$dV_1/dt = M_{SR} \cdot f\left(V_1^{ideal},\ V_1\right), \tag{6.1}$$

where $V_1^{ideal} = G \cdot V_{in}$ ($G$: gain), i.e. the ideal output. $M_{SR}$ denotes a maximum slew rate. $f\left(V_1^{ideal},\ V_1\right)$ stays between ±1 and describes a

change in the actual slew rate with time.[16] A heuristic estimation of $f\left(V_1^{ideal}, V_1\right)$ from the data in Figure 6.3b offers $f = tanh\{\alpha\left(V_1^{ideal} - V_1\right)\}$ in which the tangent hyperbolic term controls ramping-up and -down rates of $V_1$ ($\alpha$: positive constant). Equation 6.1 in conjunction with the heuristic equation well accounts for the measurement results as can be seen in Figure 6.3b. $M_{SR}$ was set to 2.5 V $\mu s^{-1}$ – the maximum slew rate of an LT1007. $G$ and $\alpha$ were set to 51 and 0.5 $V^{-1}$, respectively. The output on average points to an amplification of approximately merely 20 times, i.e. an actual gain of ca. 20, which indicates a large reduction in gain from the ideal one ($G$: 51). The non-ideal op-amp works as a low-pass filter whose cutoff 'rate' (input voltage change rate) is characterized by the maximum slew rate $M_{SR}$. The bandwidth is enlarged by adopting an op-amp with a larger maximum slew rate. Hereafter, we term a maximum slew rate $M_{SR}$ as a slew rate unless otherwise stated.

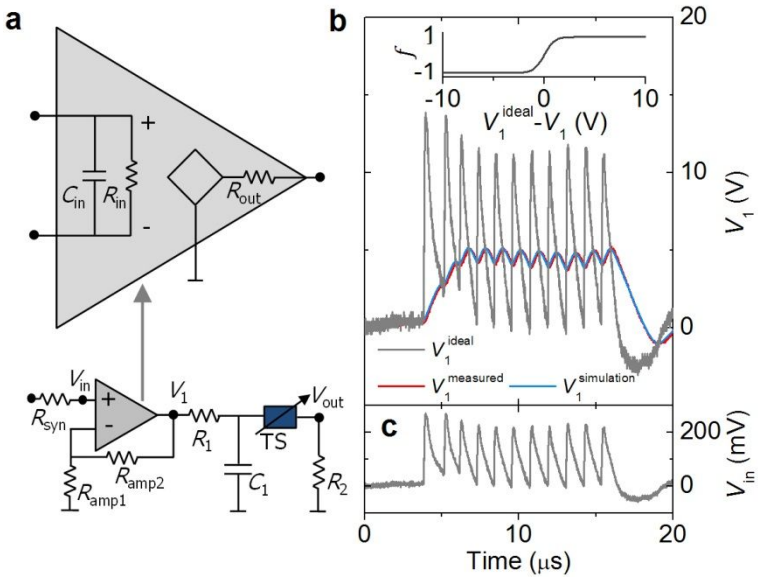


Figure 6.3 (a) Lumped circuit of the *non-ideal* op-amp in the ROLIF neuron circuit. (b) The response of the op-amp to the input spikes ($V_{in}$) plotted in (c). $V_1$ was measured (red solid line) and also calculated (blue solid line) using Equation 6.1 in conjunction with the tangent hyperbolic function plotted in the inset. $G$, $M_{SR}$, and $\alpha$ were set to 51, 2. 5 V $\mu s^{-1}$, and 0.5 $V^{-1}$, respectively.

### 6.3.4. Spiking neurons and synaptic transmission

In the SNN, spiking in a neuron is driven by a set of spikes – rather than constant input – from neighboring neurons. Thus, placing the neuron under practical conditions is required for a further justification of its neuronal behavior. Towards this end, we made a spiking analysis on a pair of neurons that were connected via a resistor $R_{syn}$ working as a synapse; the circuit is depicted in Figure 6.4a. The presynaptic neuron – subject to a sufficiently high constant voltage – was excited to spike, and the spikes were translated into EPSP ($V_1^{post}$) for the postsynaptic neuron through the aforementioned $R_{syn}$-$C_{in}$ coupling. In this regard, the postsynaptic neuron spikes in response to input spikes. Note that to avoid redundancy, we ruled out the op-amp in the presynaptic neuron insomuch as its only role is to amplify $V_{in}$. Instead, a sufficiently high voltage to require no amplification was applied to $V_{in}$.

Three different voltages (3.8, 4.6, and 5.2 V), applied to the presynaptic neuron, successfully evoked spikes and they consequently led the postsynaptic neuron to spiking as plotted in Figure 6.4b and 6.4c. $V_{out}^{pre}$ and $V_{out}^{post}$ were simultaneously acquired while applying the constant voltage. Recalling that the number of spikes parameterizes neuronal activity $a$, such measurements evaluate the activities of pre and postsynaptic neurons, $u$ and $v$, respectively. Reflecting the feature of the PAO in Figure 6.2, the presynaptic activity $u$ in Figure 6.4b tends to increase with $V_{in}$; likewise, so does the postsynaptic activity $v$ in Figure 6.4c. Notably, there exists a much longer latency for a first spike in the postsynaptic neuron than the presynaptic neuron. It points out that EPSP evolution upon the arrival of spikes in the postsynaptic neuron takes a longer time than the instance of constant voltage application to the presynaptic neuron. However, the latency becomes significantly shortened by multiple presynaptic neurons insomuch as the membrane potential of the postsynaptic neuron quickly rises amid

simultaneous input spikes through multiple synapses.

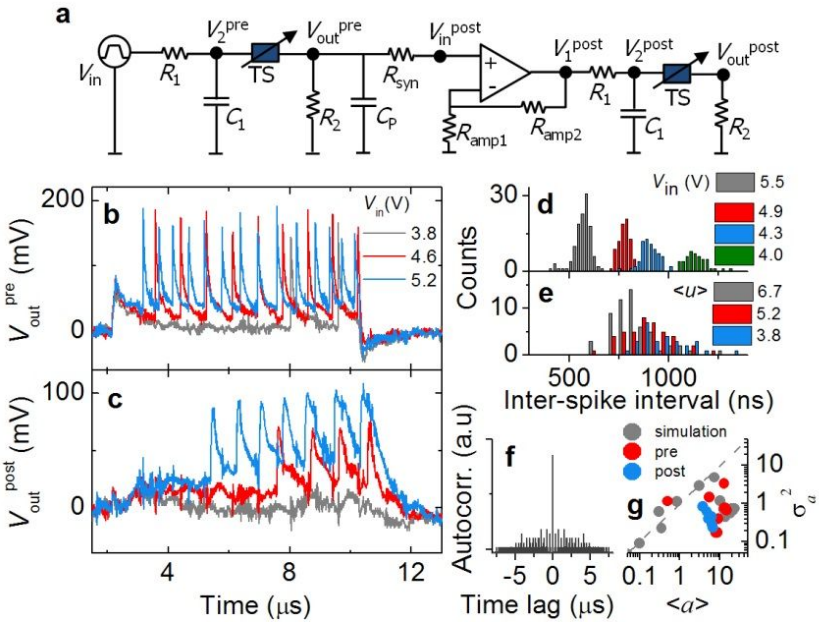


Figure 6.4 (a) Equivalent circuit of a pair of neurons that are connected through a synaptic resistor. ($R_{syn}$ = 1 kΩ and $R_{amp2}$ = 100 kΩ) $C_P$ indicates a parasitic capacitance originated from the connection. (b) Spike bursts in the presynaptic neurons at different constant voltages (3.8, 4.6, and 5.2 V) and (c) the consequent postsynaptic spike bursts. An ISI distribution for the (d) presynaptic and (e) postsynaptic spike bursts. (f) An autocorrelogram of the presynaptic spikes in the burst at 5.2 V. (g) A relationship between the measured mean $\langle a \rangle$ and variance $\sigma_a^2$ of neuronal activity. The dashed line indicates a theoretical relation for a Poisson neuron.

### 6.3.5. Neuronal noise and its randomness

The uncorrelated random variability in the threshold switching parameters is the direct cause of neuronal noise. Mapping such variability on the individual switch scale onto neuronal noise has recently been identified by theoretical means.[4] To verify this theoretical prediction, we made a statistical analysis on the neuronal noise that is represented by the variation of the ISI and the resulting spiking activity. The results are plotted in Figure 6.4d and 6.4e for pre and postsynaptic noises, respectively. The histograms for the presynaptic neuron in Figure 6.4d certainly evidence the normal distribution of the ISI, reflecting the distributional nature of the switching parameters (Figure 2.8). A note should be placed on the fact that such histograms do not necessarily justify the randomness of ISI variation; instead, a cross-correlation analysis on the ISI distribution provides clear evidence for randomness.[4, 10] For instance, the autocorrelogram in Figure 6.4f obviously visualizes no correlation within the spikes in the same burst other than self-correlation that is indicated by the peak at a time lag of zero (Figure 6.4f). The noise characteristics of the postsynaptic neuron in Figure 6.4e similarly feature to the presynaptic neuron albeit not as clear as the presynaptic neuron.

In order to compare the observed noise characteristics with the biological neuron, we further made statistics of the activity – resulting in mean activity $\langle a \rangle$ and variance $\sigma_a^2$ – on 20 spike bursts for both pre and postsynaptic neurons. The results are plotted on the $\langle a \rangle$ - $\sigma_a^2$ plane in Figure 6.4g. The dashed line denotes $\sigma_a^2 = A\langle a \rangle$ ($A$: constant), representing a Poisson noise.[10] The biological neuron often exhibits such a Poisson noise behavior.[10, 17, 18] The theoretical estimation of the neuron clearly follows the feature of a Poisson noise as shown in Figure 6.4g. A similar noise behavior is seen in the presynaptic neuron in spite of a deviation from the dashed line.

However, the postsynaptic neuron hardly uncovers the behavior in a wide activity range mainly in light of the aforementioned large latency for a first spike as seen in Figure 6.4c. Nevertheless, it appears in good agreement with the theoretical prediction in the limited activity range, so that we assume the consistency between the theoretical and experimental results.

Note that the finite impedance of the oscilloscope channel hinders us from acquiring the true $V_{out}$ for both pre and postsynaptic neurons. For instance, the spike-width widening in Figure 6.4b and 6.4c arises from the channel impedance as justified in comparison with circuit simulation results (not shown). In the following circuit simulations, we ruled out this channel impedance in the circuits so as to evaluate the true output.

### 6.3.6. Effect of op-amp on spiking dynamics of postsynaptic neuron

Provided that the gain of the op-amp varies upon the oscillation frequency of the PAO and slew rate, the spiking dynamics of the postsynaptic neuron significantly rests on the op-amp. Recall that, in Section 6.3.1, the experimental proof-of-concept demonstration of the neuron was conducted by using a commercialized op-amp. The op-amp in the neuron circuit needs to be generalized to various op-amps with different gains and slew rates so as to underpin the generalization of the circuit. Employing circuit calculations, postsynaptic neuron's spiking dynamics was examined with various gains in the 2 – 100 range and slew rates (0.1 – 20 V $\mu s^{-1}$). We also took into account random variability in the switching parameters. Each mean postsynaptic activity in the map was acquired out of 20 trials. The detail of the calculation is explained in Supplementary Information. The postsynaptic neuron's activity maps in Figure 6.5a – c were obtained at three different presynaptic neuron's activity (16.4, 17.7, and 19.6), respectively. Notably,

the slew rate has strong influence on the postsynaptic neuron's activity only when sufficiently small; for instance, Figure 6c succinctly shows a drastic change in the postsynaptic neuron's activity upon a slew rate (< 4 V $\mu s^{-1}$) at a gain of 100. The change is negligible, otherwise. The larger the slew rate, the more likely the disparity between the ideal and actual (non-ideal) outputs vanishes. Thus, the actually output becomes fairly independent of the slew rate (Figure 6.5b and 6.5c). By contrast, the gain has a larger effect on the postsynaptic neuron's activity in a larger range.

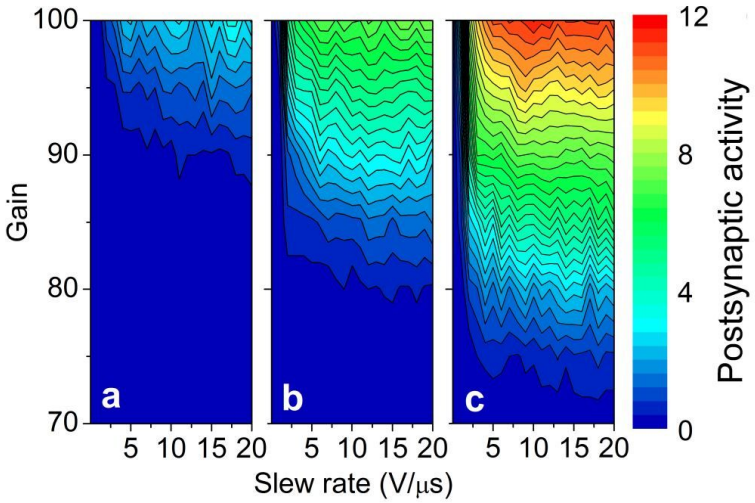


Figure 6.5 Simulated postsynaptic activity maps with respect to the gain and slew rate when the mean presynaptic activities $\langle u \rangle$ were (a) 16.4, (b) 17.7, and (c) 19.6, respectively. The calculations were conducted over 20 trials on the equivalent circuit in Figure 5a at a $R_{syn}$ of 200 kΩ.

### 6.3.7. Synaptic resistance

It is known that synaptic transmission is grounded on the synaptic efficacy causing EPSP. Likewise, synaptic transmission occurs in the pair of neurons through the synaptic resistor $R_{syn}$ leading to EPSP evolution. In this regard, we need to look into the relation between the synaptic resistance and corresponding synaptic weight. Towards this end, the circuit in Figure 6.6a was examined by calculational means at a fixed gain and a slew rate of 100 and 2.5 V $\mu s^{-1}$, respectively. The calculations at various $R_{syn}$'s result in the induced postsynaptic neuron's activity $v$ with presynaptic neuron's one $u$ (Figure 6.6a). Notably, $v$ linearly increases with $u$ at a different onset. The $u$-$v$ relation at non-zero $v$ can simply be expressed as $v = m(u - b)$ unless the $v$ max remains out of reach, where $m$ and $b$ denote the slope and onset, respectively. $m$ is nearly constant while $b$ tends to decrease with $R_{syn}$ (see the inset of Figure 6.6a).

Interestingly, a higher $R_{syn}$ causes more spikes in the postsynaptic neuron, which appears counter-intuitive. For instance, in Figure 6.6a, $v$ at 250 kΩ is approximately five times as large as that at 70 kΩ when 20 in $u$. Given the use of the non-ideal op-amp, the EPSP evolution in due course is a consequence of the coupling between $R_{syn}$ and input impedance $Z_{in}$ – particularly $C_{in}$ – alongside the finite slew rate (2.5 V $\mu s^{-1}$). The lower $R_{syn}$, the shorter the RC delay, i.e. the faster $V_{in}^{post}$ rises (falls) upon spike incidence (termination) as shown in Figure 6.6b where two spikes arrive at $R_{syn}$ at 4.6 and 5.0 μs. The op-amp that works as a low-pass filter then filters out such fast-rising $V_{in}^{post}$ (> $M_{SR}$), so that the output ($V_1^{post}$) is low. In this regard, high $R_{syn}$ is beneficial for a better signal transmission. However, the maximum $V_{in}^{post}$ decreases because of the large voltage drop across the high $R_{syn}$ (Figure 6.6b). Thus, high $R_{syn}$ trades off the consequent reduction in $V_1^{post}$ for a better transmission, so that the maximum $V_1^{post}$ is given at

particular $R_{syn}$ that reconciles these two opposite effects. For different $R_{syn}$'s, $V_1^{post}$ evolution amid arrival of a presynaptic spike train ($u$=20) is seen in Figure 6.6c. In search of $R_{syn}$ at the maximum, maximum $V_1^{post}$ was re-plotted with respect to $R_{syn}$ in Figure 6.6d in which the two regimes are indicated. The maximum is at approximately 250 kΩ, which is reflected in Figure 6.6e; postsynaptic activity $v$ reaches its maximum in the vicinity of 250 kΩ $R_{syn}$ irrespective of the mean presynaptic activity $\langle u \rangle$. As per preferences in practice, one of the two $R_{syn}$ regimes can be chosen in the circuit design when taking into account synaptic plasticity. In the following circuit calculations, we adopted $R_{syn}$ below 250 kΩ (Regime I) whose variation causes the larger change in $v$ than the other regime.

The aforementioned behavior also depends on the slew rate. $R_{syn}$ at the maximum tends to decrease with the slew rate, narrowing down the working $R_{syn}$ window (see Supplementary Information).

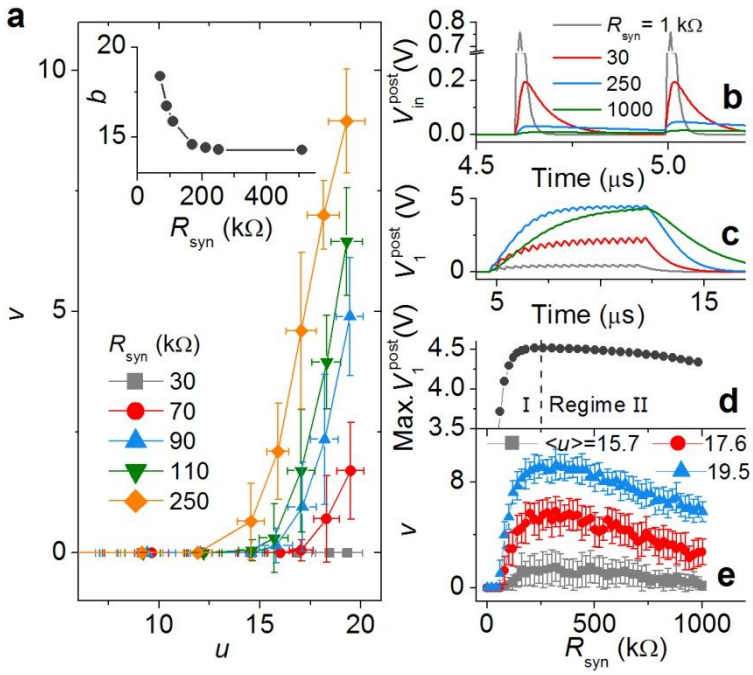


Figure 6.6 (a) Simulated postsynaptic activity $v$ with presynaptic activity $u$ for different $R_{syn}$'s. The inset shows the onset of each curve. Time-varying (b) $V_{in}^{post}$ and (c) $V_1^{post}$ upon incident presynaptic spikes at 4.6 and 5.0 μs for different $R_{syn}$'s $u$ was set to 20. (d) Maximum $V_1^{post}$ with respect to $R_{syn}$ at $u$ = 20. (e) Induced postsynaptic activity $v$ with respect to $R_{syn}$ at three different $\langle u \rangle$'s. The gain and slew rate were set to 100 and 2.5 V μs$^{-1}$, respectively. The datasets in a) and e) were obtained out of 20 trials.

### 6.3.8. Non-linear integration rule

In the SNN, a postsynaptic neuron is generally in connection to a number of presynaptic neurons via synapses. The EPSP thus evolves in due course amid simultaneously incident presynaptic currents. This type of integration is often referred to as spatial integration or spatial summation.[19-21] We examined the spatial integration of the postsynaptic neuron whose equivalent circuit is depicted in Figure 6.7a. The presynaptic neurons are numbered from one to $n$. Note that for the sake of simplicity $R_{syn}$ of all $n$ synapses was set to 30 kΩ. Given the same $V_{in}$ to all presynaptic neurons, the mean $u$, i.e. $\langle u \rangle$, of each presynaptic neuron is the same. To highlight the effect of synapse number on postsynaptic activity $v$, $v$ that is evoked by the spatial integration of $u$'s was identified for different $n$'s ($n$: 1, 13, 16, 25, and 40) whose results are plotted in Figure 6.7b. Notably, the same empirical equation, $v = m(u - b)$, describes the observed behavior with a change in the onset $b$ upon $n$ as shown in the inset of Figure 6.7b. The onset as a whole declines with $n$ – more synapses lead to more postsynaptic neuron's spikes albeit non-linear. Such a tendency is more evidently seen in Figure 6.7c in which the data in Figure 6.7b are re-plotted on an $n$-$v$ plane at three $\langle u \rangle$ values.

This finding is again seemingly counter-intuitive given that parallel synaptic resistors – of the same resistance – hinder $V_{in}^{post}$ from exceeding that for the single presynaptic neuron case when the presynaptic spikes are asynchronous (very probable in light of the Poisson spiking nature). This is evident as per the following equation: $V_{in}^{post} = \frac{G_{syn}}{G_0 + nG_{syn}} V_{out}^{pre}$, where $G_{syn}$ and $G_0$ denote the conductance of the synaptic resistor ($1/R_{syn}$) and the lumped conductance of the postsynaptic neuron, respectively. As a matter of fact, connecting a postsynaptic neuron to 100 presynaptic neurons largely

suppresses an increase in $V_{in}^{post}$ upon spiking as seen in Figure 6.7d in comparison with the single presynaptic neuron case. However, asynchronous presynaptic spikes – elicited from different presynaptic neurons – render it possible to fill the ISI in which $V_{in}^{post}$ drops to the baseline (see Figure 6.7d). The ISI-filling, however, overcompensates for the reduction in $V_{in}^{post}$ peaks when integrated over time by the op-amp, leading to a rather higher $V_1^{post}$ than the single presynaptic neuron case as shown in Figure 6.7e. As a consequence, more presynaptic neurons evoke more postsynaptic spikes in the postsynaptic neuron.

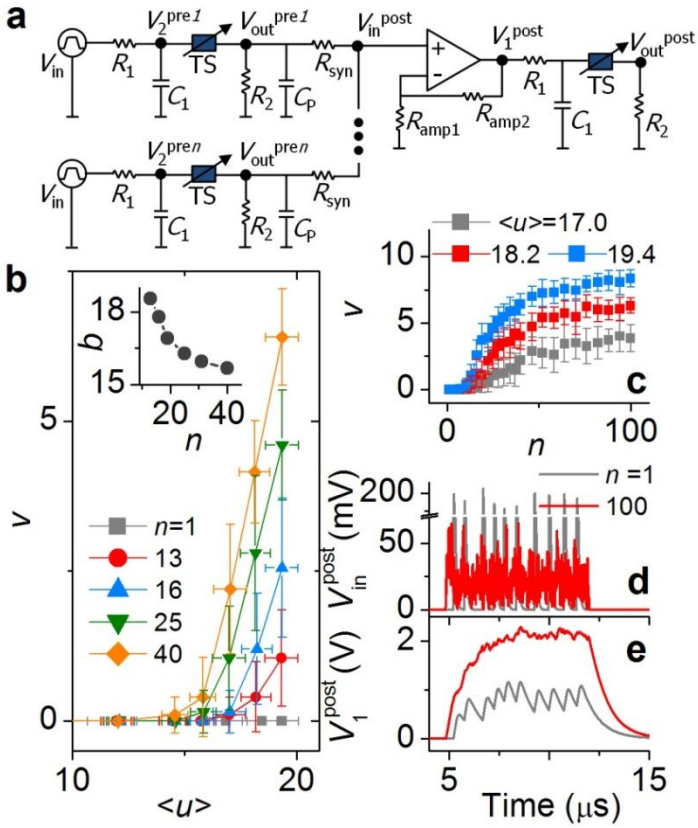


Figure 6.7 (a) Equivalent circuit of *n* presynaptic neurons connected to a single postsynaptic neuron via *n* synaptic resistors. (b) Simulated postsynaptic activity *v* with respect to mean presynaptic activity $\langle u \rangle$. The inset shows the onset of each curve. (c) Non-linear *v*-*n* relations at three different $\langle u \rangle$'s. The datasets in b) and c) were acquired out of 20 trials. (d) Time-varying $V_{in}^{post}$ and (e) $V_1^{post}$ for *n*=1 and 100 at $\langle u \rangle$ = 9.4.

## 6.4. Discussions

Provided that a passive synapse was taken into consideration in this study, the proposed neuron was subject to voltage rather than current. Adopting passive artificial synapses is an ongoing effort in light of their simple device structure that offers large-scale integrated synaptic circuits.[22-25] In particular, two-terminal 'memristive' devices implemented in a fully passive crossbar array[24, 25] have been promisingly addressed on these grounds. Although these simple passive synapses are on the neuroscience-inspired substrate, they differ in plasticity induction protocols from the biological chemical synapse. Synaptic weight in such a device is translated into resistance (or conductance), and the resistance is tweaked as per 'learning'.[25] The synaptic resistance-depending postsynaptic neuron's activity (Figure 6.6) is relevant to this translation, connecting synaptic weight to the activity via synaptic resistance. In this regard, the neuron model in this study is likely compatible with such passive synapses.

There are a number of artificial synapse models[26-29] – mostly built using scalable metal-oxide-semiconductor field-effect transistors (MOSFETs) which are more biologically plausible.[27-29] For some of them, their fidelity to the biological synapse offers excitatory postsynaptic current (EPSC)-driven postsynaptic neuron's spiking.[29] Realizing this requires active circuit elements, e.g. MOSFETs, for the synaptic circuitry, working as a current source for EPSC. Modifying the neuron circuit, particularly the op-amp, the neuron can also be used in association with such *active* artificial synapses. Current or current-to-voltage amplifiers are desirable in this instance. Either amplifier can similarly integrate and amplify the input, relaying the output to the PAO in due course. Simultaneously, an integration takes place on capacitor $C_1$ in Figure 6.1, which lasts until the TS is turned on at $V_{on}$. Therefore, the neuron is likely applicable in conjunction with different

artificial synapses in the SNN albeit different in spiking behavior in detail. The description of synaptic transmission through an active synapse is unlikely as simple as the case of passive synapse, and it is beyond the scope of the present study.

The neuron circuit is likely scalable given the element-wise scalability. The TS has been found to shrink successfully down to a few tens of nanometers in length without significant degradation of the switching property.[30] In particular, the Pt/GeSe/Pt TS represents the off-state resistance scaling with the area.[14] The capacitor in the PAO is scalable if bearing the significant reduction in capacitor area, and thus capacitance. A workaround is to compensate for the area reduction by using high-*k* dielectrics or to build three-dimensional capacitors with high aspect ratios as for capacitance-based RAM such as dynamic RAM and ferroelectric RAM.[31] In this study, a capacitance of 10 pF was assigned to the capacitor in the PAO, which provides an 'accelerated' time scale in comparison with the biological neuron. The accelerated time scale has an advantage in response speed over the real-time scale as the response is more quickly evoked in the accelerated time scale. However, recalling the advantage of the SNN over ANN in interaction with the real world, the advantage in the accelerated time scale requires much more spikes in a given physical time period than the real time scale – which causes the larger power consumption. Thus, it is of importance to reconcile capacitor scaling down with the power consumption. More specifically, the relationship between the power consumption and the activity of the PAO was examined with the size of the PAO layout. (see Figure S6 in Supplementary information)

The op-amp is scalable as well. In addition, the op-amp can be modified as per preferences in the integrated neuron circuit, we employed the particular op-amp in the experiments for experimental preferences though. The simplest case replaces the op-amp with an amplifier of two inverting

stages as for the Axon-Hillock neuron circuit.[1, 2] Irrespective of a type of amp, the slew rate tends to increase with scaling down insomuch as the capacitance-induced response lag diminishes as the capacitor area shrinks. Emphasis should therefore be placed on the gain rather than the slew rate in such integrated neuron circuits in light of the relationship shown in Figure 6.5. In addition, the vanishing response lag due to the high slew rate hinders the input integration over time through the op-amp. Fortunately, the integrator, i.e. $C_1$ in the PAO in Figure 6.1, remains available, rendering it possible to spike in the given circumstance. (see Figure S7 in Supplementary information)

## 6.5. Conclusions

We proposed a neuron circuit by exploiting a PAO and non-ideal op-amp. The proof-of-concept operation of the neuron was successfully demonstrated, which encompasses the feasible synaptic transmission through a passive synapse – equivalent to a synaptic resistor. The neuron was found to resemble the biological neuron mostly regarding the following aspects: (i) analog-type information encoding, (ii) signal amplification, (iii) unidirectional synaptic transmission, and (iv) random Poisson noise. The first and last features basically form the basis of possible application of the neuron to stochastic analog electronics.[32] The generalization of the proposed neuron as well as their connection through a synaptic resistor elucidated the importance of non-ideal phenomena – such as coupling between the synaptic resistor and the input impedance of the op-amp, and the random Poisson noise – in the synaptic transmission between pre and postsynaptic neurons, which also includes spatial integration.

## 6.6. Bibliography

[1] G. Indiveri, B. Linares-Barranco, T. J. Hamilton, A. van Schaik, R. Etienne-Cummings, T. Delbruck, S.-C. Liu, P. Dudek, P. Häfliger, S. Renaud, J. Schemmel, G. Cauwenberghs, J. Arthur, K. Hynna, F. Folowosele, S. SAÏGHI, T. Serrano-Gotarredona, J. Wijekoon, Y. Wang, K. Boahen, *Front. Neurosci.*, 5, 73 (2011).

[2] C. Mead, *Analog VLSI and Neural Systems*, Addison-Wesley, Reading, MA, USA 1989.

[3] M. D. Pickett, G. Medeiros-Ribeiro, R. S. Williams, *Nat. Mater.*, 12, 114 (2012).

[4] H. Lim, V. Kornijcuk, J. Y. Seok, S. K. Kim, I. Kim, C. S. Hwang, D. S. Jeong, *Sci. Rep.*, 5, 9776 (2015).

[5] M. Mahowald, R. Douglas, *Nature*, 354, 515 (1991).

[6] E. Farquhar, P. Hasler, *IEEE Trans. Circuits Syst.*, 52, 477 (2005).

[7] E. M. Izhikevich, *IEEE Trans. Neural Networ.*, 14, 1569 (2003).

[8] E. M. Izhikevich, *IEEE Trans. Neural Networ.*, 15, 1063 (2004).

[9] A. A. Faisal, L. P. J. Selen, D. M. Wolpert, *Nat. Rev. Neurosci.*, 9, 292 (2008).

[10] P. Dayan, L. F. Abbott, *Theoretical Neuroscience*, The MIT Press, Cambridge, MA, USA 2001.

[11] C. Eliasmith, C. H. Anderson, *Neural Engineering*, The MIT Press, Cambridge, MA, USA 2004.

[12] D. S. Jeong, I. Kim, M. Ziegler, H. Kohlstedt, *RSC Adv.*, 3, 3169 (2012).

[13] J. Astrup, P. M. Sorensen, H. R. Sorensen, *Stroke*, 12, 726 (1981).

[14] D. S. Jeong, H. Lim, G.-H. Park, C. S. Hwang, S. Lee, B.-k. Cheong, *J. Appl. Phys.*, 111, 102807 (2012).

[15] A. R. Hambley, *Electrical engineering*, Pearson Education, Upper

Saddle River, NJ, USA 2008.

[16] P. E. Allen, *IEEE Trans. Circuits Syst.*, 25, 565 (1978).

[17] K. H. Britten, M. N. Shadlen, W. T. Newsome, J. A. Movshon, *Visual Neurosci.*, 10, 1157 (1993).

[18] D. J. Tolhurst, J. A. Movshon, I. D. Thompson, *Exp. Brain Res.*, 41, 414 (1981).

[19] J. L. Reed, P. Pouget, H. X. Qi, Z. Y. Zhou, M. R. Bernard, M. J. Burish, J. Haitas, A. B. Bonds, J. H. Kaas, *P. Natl. Acad. Sci. U.S.A.*, 105, 10233 (2008).

[20] M. Adachi, K. Aihara, *Neural Networks*, 10, 83 (1997).

[21] A. Polsky, B. W. Mel, J. Schiller, *Nat. Neurosci.*, 7, 621 (2004).

[22] S. H. Jo, T. Chang, I. Ebong, B. B. Bhadviya, P. Mazumder, W. Lu, *Nano Lett.*, 10, 1297 (2010).

[23] D. Kuzum, R. G. D. Jeyasingh, B. Lee, H. S. P. Wong, *Nano Lett.*, 12, 2179 (2011).

[24] G. S. Snider, *NANOARCH 2008*, 85 (2008).

[25] M. Prezioso, F. Merrikh-Bayat, B. D. Hoskins, G. C. Adam, K. K. Likharev, D. B. Strukov, *Nature*, 521, 61 (2015).

[26] H. Lim, I. Kim, J. S. Kim, C. S. Hwang, D. S. Jeong, *Nanotechnology*, 24, (2013).

[27] M. R. Azghadi, N. Iannella, S. F. Al-Sarawi, G. Indiveri, D. Abbott, *Proc. IEEE*, 102, 717 (2014).

[28] V. Kornijcuk, O. Kavehei, H. Lim, J. Y. Seok, S. K. Kim, I. Kim, W. S. Lee, B. J. Choi, D. S. Jeong, *Nanoscale*, 6, 15151 (2014).

[29] N. Qiao, H. Mostafa, F. Corradi, M. Osswald, F. Stefanini, D. Sumislawska, G. Indiveri, *Front. Neurosci.*, 9, 141 (2015).

[30] M. J. Lee, D. Lee, S. H. Cho, J. H. Hur, S. M. Lee, D. H. Seo, D. S. Kim, M. S. Yang, S. Lee, E. Hwang, M. R. Uddin, H. Kim, U. I. Chung, Y. Park, I. K. Yoo, *Nat. Commun.*, 4, 2629 (2013).

[31] S. K. Kim, S. W. Lee, J. H. Han, B. Lee, S. Han, C. S. Hwang, *Adv. Funct. Mater.*, 20, 2989 (2010).

[32] T. J. Hamilton, S. Afshar, A. van Schaik, J. Tapson, *Proc. IEEE*, 102, 843 (2014).

# 7. Conclusions

In this thesis, the proof-of-concept demonstration was addressed for the hardware realization of building blocks of SNN. Functionalities of the artificial synapse and the artificial neuron were realized by adopting functioning materials based on resistive switching phenomena which can partly replace CMOS-based elements. Thus, SNNs' circuitry could be simplified by employing a less number of CMOS-based elements.

The STM effect of the artificial synapse was demonstrated by employing $TiO_2$-based ECs adopting reactive TEs. The synaptic weight of ECs could be modulated by changing either the polarity of input spike or the input spike activity. The input activity-dependent synaptic potentiation was parameterized by employing empirical equations adopting a 'sliding threshold' concept, which was inspired from BCM rule. The dynamic equilibrium between forward and backward reactions of potentiation could be understood in light of the TE-related redox reaction. Note that there are a few synaptic functionalities which were not realized in ECs, such as a spike-timing-dependent-plasticity. At this moment, how to implement this concept into ECs is an open question.

The spiking phenomenon of the biological neuron was realized by employing non-memory resistive switching systems. The non-faradic type $Pt/TiO_2/Pt$ capacitor exhibited the ionic-to-electronic conduction transition phenomenon, which was induced by EMF originated from the point-defect migration. The abrupt resistance change induced by the ionic-to-electronic conduction transition successfully emulated spike generation in the short time period. However, the non-faradaic capacitor itself could not encode the constant input stimulus by means of the spiking activity. This is due to the fact that, unlike the biological neuron, oscillatory membrane potential under

the constant stimulus could not be realized by single non-faradaic capacitor without assistant circuits for oscillation.

The NLIF neuron is one of the hardware-realizable LIF neuron, which is composed of two PAO encompassing TSs. As discussed in Section 5.2.2, membrane potential of the NLIF neuron could be described by limited cycles in the phase plane, generating a spike train under the constant input stimulus. In this regard, analog-to-analog type information encoding was demonstrated. Provided the potential variability of behavior of the TS, encoding reliability of individual NLIF neuron strongly depended on the neuronal noise. Although the encoding process of individual NLIF neuron was unreliable, however, one could extract reliable information from population of NLIF neurons by employing Bayesian decoding method. On the basis of Bayesian decoder, increase in the number of NLIF neurons in the population tolerated a larger variability of switching parameters of the TS. Nevertheless, the variability of switching parameters should be placed within tolerance range.

Towards the hardware-realized LIF neuron, the proof-of-concept demonstration of the ROLIF neuron was addressed. The ROLIF neuron emulated neuronal functionalities in terms of (i) analog-to-analog type information encoding, (ii) signal amplification, (iii) random Poisson noise, and (iv) unidirectional signal transmission. The last feature was expected to enable the ROLIF neuron to build the neural network along with passive synapses. Notably, the feasibility of the network configuration was demonstrated by means of the basic synaptic transmission via a synapse resistor between ROLIF neurons. Furthermore, both the synaptic weight dependence and effect of the number of presynaptic connections were investigated to verify basic conditions for neural networks by the simulation method. It turned out that non-ideal phenomena - such as coupling between the synaptic resistor and the input impedance of the op-amp, and the random Poisson noise – played a crucial role for spatial integration of signal.

# 8. Supplementary information

### *Calculation of ionic current in a non-faradaic capacitor*

In a MIEC, both electrons and mobile ions/defects contribute to the dc current. In a non-faradaic capacitor, the interface between the MIEC and electrode forms a blocking contact for mobile ions/defects. Hence, the number of the mobile ions/defects is conserved in the capacitor, i.e. they are confined in the MIEC. However, for electrons this capacitor is regarded as an open system connected to an electron reservoir. The dc ionic and electronic currents are described separately below.

Dc current in a MIEC is driven by two driving forces, chemical and galvani potential gradients. The former and the latter are termed diffusion and drift currents. Within the scope of a first-order approximation, the summation of drift and diffusion fluxes of charged particle $i$, $j^i_{drift}$ and $j^i_{diff}$, through a one-dimensional electrode/MIEC/electrode capacitor, which is termed as drift-diffusion flux $j^i_{dd}$, is given by

$$j^i_{dd} = z_i c^i \mu_i E - D_i \frac{dc^i}{dx}, \tag{S1}$$

where $z_i$, $c^i$, $\mu_i$, $D_i$, and $E$ denote the ionization number, the concentration, the mobility of particle $i$, $D_i$,and the internal electric field, respectively. The first and the second term on the right side of Eq. (S1) mean the drift and the diffusion fluxes, respectively. Therefore, the dc ionic current density attributed to the drift-diffusion of particle $i$ is $j^i_{dc} = z_i q j^i_{dd}$, where $q$ means the elementary charge. For $TiO_2$ MIEC, $i = V_O^{\cdot\cdot}$, denoting oxygen vacancy in the Kröger-Vink nomenclature.[1]

In a non-faradaic capacitor, the migration mobile ions/defects are confined within the MIEC, i.e. the drift-diffusion fluxes at the two interfaces of the capacitor are zero. That is, no exchange of ions/defects takes place through

the interfaces. These boundary conditions play a key role in evaluating the time-dependent distribution of ions/defects in the MIEC. When a faradaic type capacitor is dealt with, appropriate formalism for ion/defect fluxes at the interface, e.g. the Butler-Volmer equation, can be used as boundary conditions instead.[2]

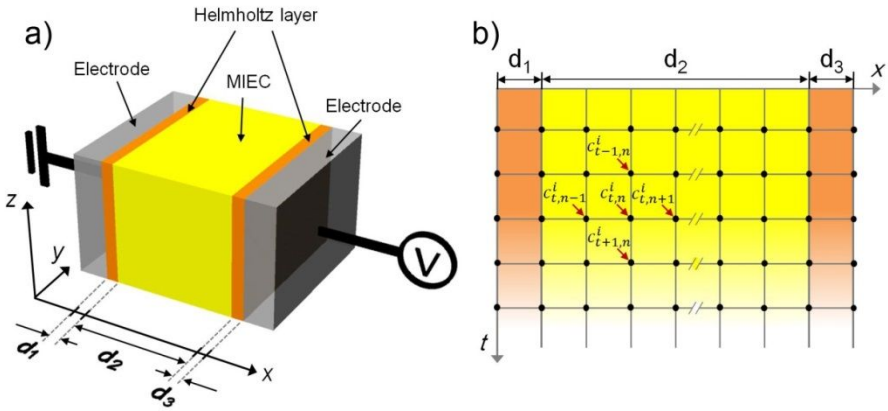


Figure S1. (a) Schematic of a non-faradaic capacitor utilizing an MIEC. A voltage is applied to the right electrode while the left electrode is grounded. (b) Configuration of the nodes in a one-dimensional non-faradaic capacitor in distance *x* and time *t* dimensions.

### *Calculation of dc electronic current in a non-faradaic capacitor*

For electrons, the non-faradaic capacitor is not a closed system so that their injection into and ejection from the capacitor and their drift-diffusion in the MIEC should be taken into account. It was assumed here that electrons in the electrode exhibit free electronic behavior and the MIEC has a single conduction band minimum. Also, it was assumed a mechanism for the injection of electrons from the electrode to the MIEC to be thermionic emission attributed to electron injection overcoming the band offset, i.e. Schottky barrier, at the electrode/MIEC interface.[3, 4] Electronic current

density from the MIEC to electrode (reservoir), i.e. electron's flux from the electrode to the MIEC, is denoted by $j_{dc,1}^{e}$.

The reverse current density $j_{dc,2}^{e}$, attributed to the electron's flux from the MIEC to the electrode, should also be considered to describe the dc electronic current density at the interface. This reverse current density can be expressed as the following equation:

$$j_{dc,2}^{e} = q v_r n_0, \tag{S2}$$

where $v_r = \frac{A^* T^2}{q N_c}$, and $A^*$, $T$, and $N_c$ denote the Richardson constant, temperature, the effect density of states for electrons in the MIEC.[5] And $n_0$ in Eq. (S2) indicates the concentration of electrons at the interface. In this model system, a voltage is applied to the right electrode as shown in Figure S1a. In accordance, electric current along the positive x-axis is taken as positive. This results in the opposite polarity of electric current such as negative current under a positive voltage, however, later we make the polarity reversed. The net current density at the left interface in Figure S1a can therefore be written as $j_{dc}^{e} = j_{dc,1}^{e} - j_{dc,2}^{e}$, whereas that at the right interface $j_{dc}^{e} = -j_{dc,1}^{e} + j_{dc,2}^{e}$. These two equations serve as the boundary conditions for the electrons' transport through the capacitor.

Electronic current density in the MIEC is described in terms of the distribution of electrons and a gradient of their electrochemical potential, i.e. Fermi level $\epsilon_f$. For a one-dimensional system, an electronic current density equation is $j_{dc}^{e} = n \mu_e d\epsilon_f / dx$, where $n$ and $\mu_e$ denote electron concentration and electron's mobility, respectively. In addition, the electron concentration in the MIEC depends on the electron's effective mass $m_e$, the conduction band minimum $\epsilon_c$, and the electron's electrochemical potential $\epsilon_f$, through the following equation:

$$n = \int_{\epsilon_c}^{\infty} g(\epsilon) f(\epsilon) d\epsilon, \tag{S3}$$

where the density of states of electrons $g(\epsilon) = \frac{8\pi(2m_e^3)^{1/2}}{h^3}(\epsilon - \epsilon_f)^{1/2}$. Now, the electronic current density in the MIEC becomes a function of the distribution of the electrons' electrochemical potential and the galvani potential. Note that the conduction band minimum $\epsilon_c$ is a function of the galvani potential $V$ through the equation, $\epsilon_c = \phi_b - qV$, where $\phi_b$ denotes the band offset at the electrode/MIEC interface.

The time-domain calculation of ionic and electronic current density cannot be performed using an analytical method, and thus the Crank-Nicolson method was employed, combing explicit and implicit finite difference methods.[5] In this time-domain calculation, electrons' behavior can be evaluated using a quasi-static approximation since electron's mobility is much larger compared to that of an ion or an ionic defect. Employing the quasi-static approximation gives the important condition that electronic current density is constant at all positions in the one-dimensional MIEC at a given time. This condition defines the relationship between galvani potential and electrochemical potential, implying that these two variables are dependent on each other. That is, if the distribution of galvani potential is known, so is that of electrochemical potential.

### *Calculation of time-dependent current in a non-faradaic capacitor*

Considering the configuration of J-V measurements on a non-faradaic capacitor, a capacitor illustrated in Figure S1a together with an equivalent series resistance (ESR) should be taken into account. An ESR includes all possible resistance contributions in the configuration, e.g. electrode resistance, wire resistance, and internal resistance of the measurement setup. Concerning the voltage division in the configuration, an applied voltage $V_{ap}$, which is time-dependent, is expressed as

$$V_{ap} = -AR_{ESR}j + V_c, \tag{S4}$$

where $A$, $R_{ESR}$, $j$, and $V_c$ mean the area of the capacitor, the ESR, total current density including dc and displacement current, and the voltage drop along the capacitor, respectively. The total current density $j$ is described as

$$j = j_{dc} - \epsilon_r \epsilon_0 \frac{d}{dt}\left(\frac{dV}{dx}\right), \tag{S5}$$

where the first and the second terms on the right side of Eq. (S5) denote dc and displacement currents, respectively. $j_{dc}$ is the summation of dc ionic current $j_{dc}^{i}$ and dc electronic current $j_{dc}^{e}$, which are discussed in Sections 1 and 2, respectively. $\epsilon_r$, $\epsilon_0$, and $V$ are a relative permittivity, the permittivity of vacuum, and galvani potential, respectively. Integrating Eq. (S5) over time from zero to $t'$ gives

$$\left.\frac{dV}{dx}\right|_{t=t'} = \left.\frac{dV}{dx}\right|_{t=0} + (\epsilon_r \epsilon_0)^{-1} \int_0^{t'} (j_{dc} - j) dt. \tag{S6}$$

Again, by integrating Eq. (S6) over $x$ from zero to the capacitor thickness, $d_1 + d_2 + d_3$, one can evaluate the voltage assigned to the capacitor $V_c$ at $t'$ as follows:

$$V_c(t') = V_c(0) + \int_0^d (\epsilon_r \epsilon_0)^{-1} \int_0^{t'} (j_{dc} - j) dt dx. \tag{S7}$$

Due to charge conservation, Fick's second law for electric charge in this one-dimensional capacitor is described as $dj_{dc}/dx = -d\rho/dt$, where $\rho$ means charge density. Using the Poisson's equation, $\rho = dD/dx$, where $D$ means dielectric displacement, $D = -\epsilon_r \epsilon_0 dV/dx$, Fick's second law can be rewritten as

$$\frac{d}{dx}\left(j_{dc} + \frac{dD}{dt}\right) = \frac{d}{dx}\left[j_{dc} - \epsilon_r \epsilon_0 \frac{d}{dt}\left(\frac{dV}{dx}\right)\right] = \frac{dj}{dx} = 0. \tag{S8}$$

Solutions of Eq. (S8) are constant along axis $x$, meaning that the total current density $j$ is not a function of $x$. Therefore, Eq. (S7) can be rewritten as

$$V_c(t') = V_c(0) + \int_0^d (\epsilon_r \epsilon_0)^{-1} \int_0^{t'} j_{dc} dt dx - \int_0^d (\epsilon_r \epsilon_0)^{-1} dx \int_0^{t'} j dt. \tag{S9}$$

Entering Eq. (S9) into Eq. (S4) gives an equation relating an applied voltage $V_{ap}$ to the dc current density $j_{dc}$ and the total current density $j$ as follows:

$$V_{ap} = -AR_{ESR}j + V_c(0) + \int_0^d (\epsilon_r\epsilon_0)^{-1} \int_0^{t'} j_{dc} dt dx - \int_0^d (\epsilon_r\epsilon_0)^{-1} dx \int_0^{t'} j dt. \tag{S10}$$

For an easier calculation, Eq. (S10) needs to be differentiated with respect to time, which leads to

$$\frac{dV_{ap}}{dt} = -AR_{ESR}\frac{dj}{dt} + \int_0^d (\epsilon_r\epsilon_0)^{-1} j_{dc} dx - j\int_0^d (\epsilon_r\epsilon_0)^{-1} dx. \tag{S11}$$

Eq. (S11) can be numerically solved using the Crank-Nicolson method.[6] Nodes along $x$ and $t$ axes are illustrated in Figure S1b. Using the Crank-Nicolson method, Eq. (S11) in the time interval $t_1 - (t_1 + \Delta t)$ is expressed as

$$\Delta t^{-1}\left[V_{ap}(t_1 + \Delta t) - V_{ap}(t_1)\right] = -AR_{ESR}\Delta t^{-1}[j(t_1 + \Delta t) - j(t_1)] + B_1 - B_2 j(t_1 + \Delta t), \tag{S12}$$

where

$$B_1 = \sum_{i=1}^{n+1} (\epsilon_r\epsilon_0)^{-1} j_{dc}(t_1 + \Delta t)\Delta x, \tag{S13}$$

and

$$B_2 = \epsilon_0^{-1}[\epsilon_{r1}^{-1} d_1 + \epsilon_{r2}^{-1} d_2 + \epsilon_{r3}^{-1} d_3]. \tag{S14}$$

where, $\epsilon_{r1}$ $(d_1)$, $\epsilon_{r3}$ $(d_3)$, and $\epsilon_{r2}$ $(d_2)$ denote the relative permittivities (thicknesses) of the left Helmholtz layer, the right Helmholtz layer, and rest of the capacitor volume, respectively. Eq. (S12) can be further rearranged by entering Eq. (S4) into it as follows:

$$j(t_1 + \Delta t) = -(AR_{ESR} + B_2\,\Delta t)^{-1}\left[V_{ap}(t_1 + \Delta t) - V_c(t_1) - B_1\Delta t\right]. \tag{S15}$$

Insomuch as the current density $j$ is constant in the MIEC at a given time, from Eq. (S5), galvani potential distribution in the MIEC can be evaluated as far as the dc current $j_{dc}$ in Eq. (S5) is known at all position nodes in the MIEC at a given time.

As mentioned earlier, electron distribution in the MIEC can be simplified using the quasi-static approximation so that it is time-independent. However,

ion/defect distribution should be taken into account in a time domain. Again, Fick's second law can be utilized for this purpose. Fick's second law for ion/defect $i$ can therefore be described as

$$\frac{dc_i}{dt} = -\frac{d j_{dd}^{i}}{dx}. \tag{S16}$$

The drift-diffusion flux of oxygen vacancies $j_{dd}^{i}$ is a function of galvani potential and so is the concentration of ion/defect $i$ via Eq. (S16). For a non-faradaic capacitor based on $TiO_2$ MIEC, $i = V_O^{\cdot\cdot}$ as mentioned earlier. In a non-faradaic capacitor, the drift-diffusion flux of oxygen vacancies $j_{dd}^{i}$ is zero at the two interfaces so that this condition works as a boundary condition in solving Eq. (S16).

As above-mentioned, all three different current types, $j_{dc}^{i}$, $j_{dc}^{e}$, and $j$, are given by functions of galvani potential distribution and they are indeed self-consistent equations. This means that, by means of an iteration method, one can evaluate the three quantities at all positions (nodes) in the MIEC as well as time nodes in a time domain. In this calculation, the Newton-Raphson iteration was utilized.

### *Impedance spectroscopy of a Pt/TiO$_2$/Pt non-faradic capacitor*

The dielectric constant of $TiO_2$ MIEC was determined from its admittance spectra. As suggested by Jeong et al., an equivalent circuit of a Pt/$TiO_2$/Pt capacitor is a parallel connection of a capacitor and a resistor.[7] The admittance $Y$ of this capacitor is

$$Y = j2\pi\omega C + 1/R, \tag{S17}$$

where $\omega$, $C$, and $R$ denote frequency, the capacitance and the resistance of the capacitor, respectively. Therefore, from the imaginary part of an admittance spectrum, $Im(Y)$, the capacitance can be extracted. For capacitors with five different pad-sizes, each $Im(Y)$ spectrum is plotted in

Figure S2a. Note that, at frequencies below 1 MHz, neither open circuit nor short circuit calibration was necessary. The measured spectra show the good linearity of $Im(Y)$ and frequency as shown in Figure S2a. Eventually, the dielectric constant of $TiO_2$ is evaluated by plotting the capacitance vales of the five capacitors with respect to the pad-sizes. From the slope of the data in Figure S2b, a dielectric constant of approximately 39 can be obtained. This value serves as one of critical parameters for the J-V calculations.

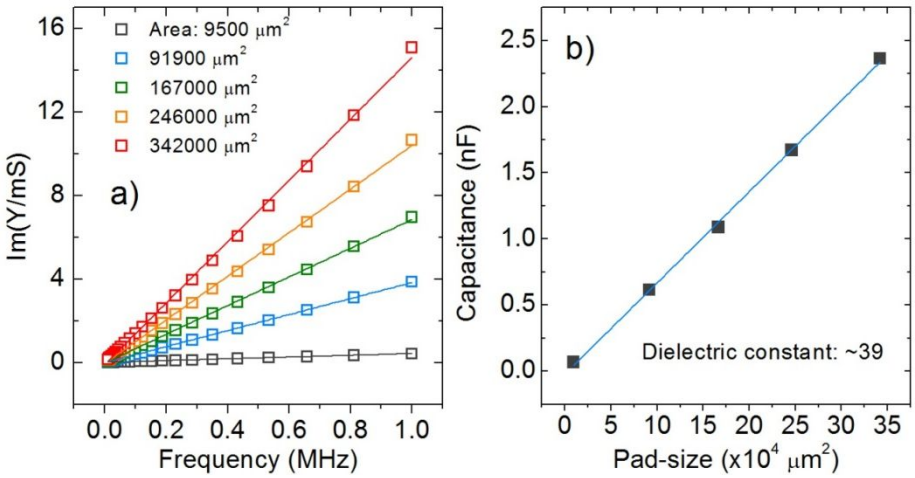


Figure S2. (a) Admittance spectra (imaginary part) of Pt/$TiO_2$/Pt non-faradaic capacitors with five different pad-sizes. (b) Capacitance vales extracted from the admittance spectra with respect to pad-size. The dielectric constant of the MIEC was evaluated from the slope to be approximately 39.

### *Influence of oxygen gas injection during top electrode deposition on the counter-clockwise J-V hysteresis*

To identify the nature of mobile point defects in a Pt/$TiO_2$/Pt capacitor, we fabricated a similar capacitor with injection oxygen gas during TE deposition. It can be predicted that TE deposition perhaps causes the

reduction of $TiO_2$ MIEC in chemical and/or mechanical manners. To prevent this possible reduction, oxygen gas was injected while the Pt TE was deposited. For convenience, let us term this capacitor as Pt(O)/$TiO_2$/Pt. As can be seen in Figure S3, the oxygen injection process leads to significant shrinkage of CCW as well as CW J-V hysteresis. We estimate that the injected oxygen gas was used in the re-oxidation of the $TiO_2$ MIEC, and thus the number of oxygen vacancies is significantly reduced in the Pt(O)/$TiO_2$/Pt capacitor compared with a Pt/$TiO_2$/Pt capacitor. Therefore, this experimental result is believed to indicate oxygen vacancy as a type of the dominant point defect in the Pt/$TiO_2$/Pt capacitor.

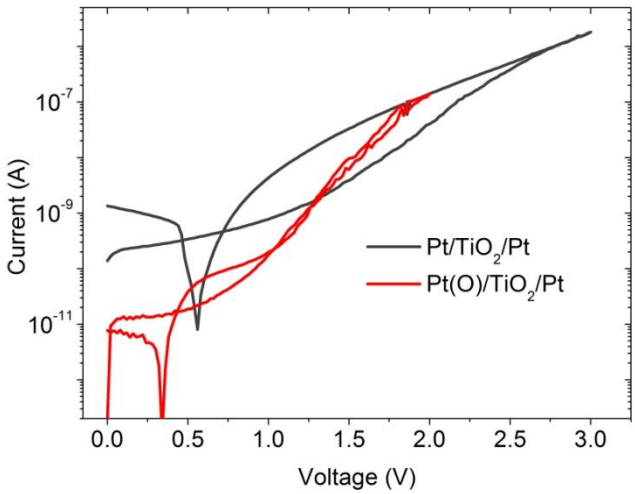


Figure S3. J-V hysteresis of a Pt(O)/$TiO_2$/Pt capacitor, compared with that of a Pt/$TiO_2$/Pt capacitor.

### *Activity limit of the NLIF neuron*

Spike firing in due course in the NLIF neuron significantly depends on charging and discharging of capacitors $C_1$ and $C_2$ as the flicker of switch $S_2$ during its operation results from consecutive charging and discharging of

capacitor $C_2$. It takes a particular time for capacitors to be charged and discharged, which is defined as an RC time constant. It is therefore predictable that the maximum number of spikes over a period of given time (here, 30 ms) is limited by the capacitive behavior. This limit is seen when it comes to high activity, for instance, the NLIF neuron with 5 percent $R_{on}$ and $R_{off}$ deviation (see Figure 5.6). A drastic decrease in variance at high mean activities ( > ca. 20) can be seen, implying that the variance is no longer determined by the deviation of the resistance. To highlight this activity limit, distributions of activity triggered by two different input currents (0.4 and 1.0 A) are acquired for different $R_{on}$ and $R_{off}$ deviations as shown in Figures S3a and b. Considering the spike firing characteristics shown in Figure 5.6, in general, a higher current as well as a smaller resistance deviation results in a larger mean activity. However, when the activity becomes close to the limit (ca. 45), the activity limit no longer allows higher activity, so that the variance is largely suppressed as shown in Figure S3b. The limit effect on variance is obviously seen in the comparison between the two different input current cases shown in Figures S5c and d, in which the variance of the 1.0 A injection case is largely reduced. For a comparison with the Poisson neuron, the Fano factor, denoting a variance to mean ratio, is evaluated for the two different current injection cases with respect to assumed resistance deviation (see Figure S3e). The Poisson neuron exhibits a Fano factor of unity as indicated using a dashed line in Figure S3e.[8] Unlike the perfect Poisson neuron, the Fano factor of the NLIF neuron varies upon the resistance deviation. In particular, at higher resistance deviations the Fano factor is larger than unity; the variance is larger than the mean activity, and thus the variance of the NLIF neuron is larger than that of the Poisson neuron at a given mean activity. This leads to a larger uncertainty in the Bayesian decoding than the Poisson neuron case as shown in Figure 5.9.

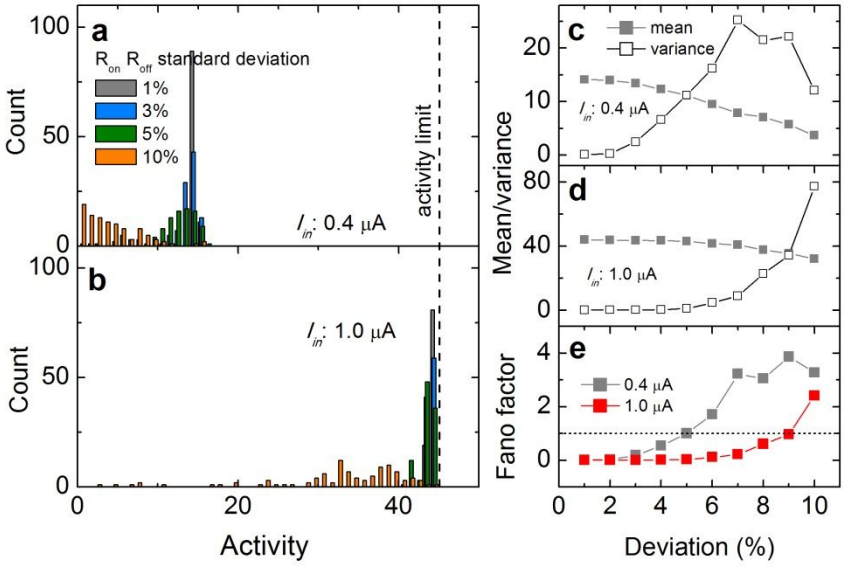


Figure S4. Histrograms of activity for cases of (a) low mean activity ($I_{in}$: 0.4 μA) and (b) high mean activity ($I_{in}$: 1.0 μA), which were acquired over 100 time trials. The dashed line in the left panel indicates the activity limit. The mean and variance of activity for different resistance deviations are plotted for cases of (c) low ($I_{in}$: 0.4 μA) and (d) high ($I_{in}$: 1.0 μA) current injection. (e) The Fano factors, i.e. variance/mean ratio, for the two different current injection cases are shown with respect to resistive deviation.

### *Injected current into each NLIF neuron in a population and its response*

For each NLIF neuron in a population of 20 NLIF neurons, injected current with respect to orientation is plotted in Figure S4a, which represents a bell-shape curve. And the corresponding tuning curve of the NLIF neuron is shown in Figure S4b. The tuning curves were evaluated on the assumption of no deviation of $R_{on}$ and $R_{off}$.

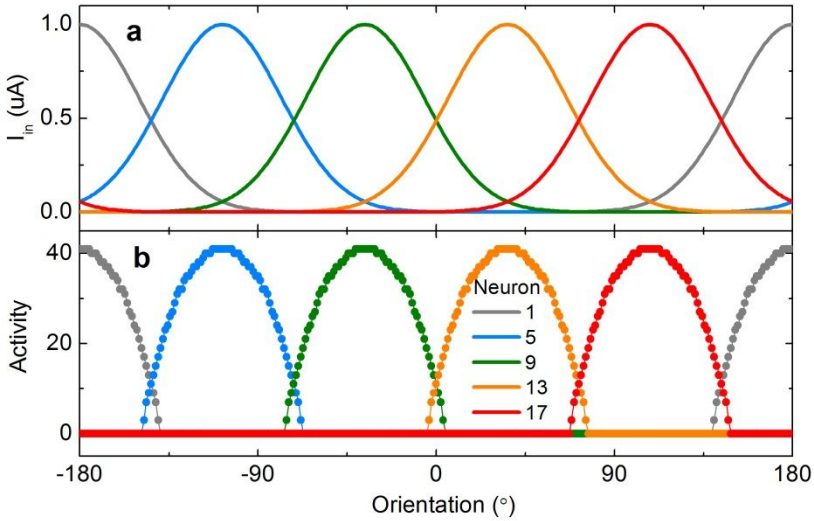


Figure S5. (a) Injected current into each NLIF neuron with an each preferred orientation in a population of 20 neurons in total. Current profiles of only 5 neurons among 20 ones in total are plotted in this figure. (b) Tuning curves of the sampled 5 NLIF neurons responding to the injected current shown in (a). Note that no resistance deviation was assumed in this calculation.

### *Time dependent circuit calculation of the ROLIF neuron*

The calculations of the circuit in Figure 6.4a were performed following three steps: (i) $V_2^{pre}$, $V_{out}^{pre}$, and $V_{in}^{post}$, (ii) $V_1^{post}$, and (iii) $V_2^{post}$ and $V_{out}^{post}$ evaluation steps. First, the three variables ($V_2^{pre}$, $V_{out}^{pre}$, and $V_{in}^{post}$) related to the presynaptic neuron were described by employing the Kirchhoff's current law at each node as follows:

$$C_1 \frac{dV_2^{pre}}{dt} = \frac{V_{in}-V_2^{pre}}{R_1} - \frac{V_2^{pre}-V_{out}^{pre}}{R_{TS}}, \tag{S18}$$

$$C_P \frac{dV_{out}^{pre}}{dt} = \frac{V_2^{post}-V_{out}^{pre}}{R_{TS}} - \frac{V_{out}^{pre}-V_{in}^{post}}{R_{syn}} - \frac{V_{out}^{pre}}{R_2}, \tag{S19}$$

and

$$C_{in}\frac{dV_{out}^{pre}}{dt}=\frac{V_{out}^{pre}-V_{in}^{post}}{R_{syn}}-\frac{V_{in}^{post}}{R_{in}}, \tag{S20}$$

where $R_{\text{in}}$ and $C_{\text{in}}$ are the input resistance and capacitance of the non-ideal op-amp, respectively. Eqs. (S18)-(S20) were numerically solved by the Crank-Nicolson method. The corresponding discrete forms are expressed as

$$\frac{C_1}{\Delta t}\left(V_2^{pre}(t+1)-V_2^{pre}(t)\right)=\frac{1}{2R_1}\left(V_{in}(t+1)+V_{in}(t)\right)+\frac{1}{2}\left(\frac{1}{R_{TS}}-\frac{1}{R_1}\right)\left(V_2^{pre}(t+1)+V_2^{pre}(t)\right)-\frac{1}{2R_{TS}}\left(V_{out}^{pre}(t+1)+V_{out}^{pre}(t)\right), \tag{S21}$$

$$\frac{C_P}{\Delta t}\left(V_{out}^{pre}(t+1)-V_{\text{out}}^{pre}(t)\right)=\frac{1}{2R_{TS}}\left(V_2^{pre}(t+1)+V_2^{pre}(t)\right)-\frac{1}{2}\left(\frac{1}{R_{TS}}+\frac{1}{R_{syn}}+\frac{1}{R_2}\right)\left(V_{out}^{pre}(t+1)+V_{out}^{pre}(t)\right)+\frac{1}{2R_{syn}}\left(V_{in}^{post}(t+1)+V_{in}^{post}(t)\right), \tag{S22}$$

and

$$\frac{C_{in}}{\Delta t}\left(V_{in}^{post}(t+1)-V_{in}^{post}(t)\right)=\frac{1}{2R_{syn}}\left(V_{out}^{pre}(t+1)+V_{out}^{pre}(t)\right)+\frac{1}{2}\left(\frac{1}{R_{in}}+\frac{1}{R_{syn}}\right)\left(V_{in}^{post}(t+1)+V_{in}^{post}(t)\right), \tag{S23}$$

respectively. Second, $V_1^{post}$ was evaluated by numerically solving Eq. (18). Likewise, the equation can be re-written by a discrete formula. Third, employing the Kirchhoff's current law at each node of the postsynaptic neuron, $V_2^{post}$ and $V_{out}^{post}$ – describing postsynaptic dynamics – were finally calculated by solving the following equations:

$$C_1\frac{dV_2^{post}}{dt}=\frac{V_1^{post}-V_2^{post}}{R_1}-\frac{V_2^{post}-V_{out}^{post}}{R_{TS}}, \tag{S24}$$

and

$$\frac{V_2^{post}-V_{out}^{post}}{R_{TS}}=\frac{V_{out}^{post}}{R_2}. \tag{S25}$$

Eqs. (S24) and (S25) were numerically solved by the Crank-Nicolson method. In order to take into consideration random variability in the

switching parameters of the TS, the TS was endowed with random parameters ($R_{on}$, $R_{off}$, $V_{on}$, and $V_{off}$) for each switching cycle, which follow a normal distribution.

### *Relationship between the power consumption and activity of the PAO with the size of PAO layout*

The power consumption of the PAO was calculated. The PAO consumed ~100 pJ/spike at ~2 MHz, (see the red line of Figure S6a at $R_1$=50 kohm; the maximum number of spikes of Figure 6.2c (~20) corresponds to activity of ~2 MHz) which translated to ~2 μJ/spike at 100 Hz. (see the blue line) The relatively high power consumption of the PAO could be reduced with $R_1$ due to reduced activity (see Figure S6b) induced by enlarged RC integration time. One can notice that the power consumption at 100 Hz can be reduced down to ~10 nJ/spike at $R_1$=10 Mohm. Also, the size of the PAO was estimated by employing a layout program, Microwind. $C_1$ (10 pF) and $R_1$ (50 kohm) corresponded to ~ $10^5$ $\mu m^2$ and ~$10^3$ $\mu m^2$, respectively. Provided that the size of TS (25 $\mu m^2$), a large proportion of the layout belongs to the capacitor, $C_1$. The size of $C_1$ (10 pF) is comparable to $R_1$, even though $R_1$ is elevated to 10 Mohm. In addition, there are several methods to reduce the size of the layout; i) employing high-k dielectric materials for the capacitor, ii) employing non-linear semiconducting materials for the resistor, $R_1$, due to the fact that roles of $R_1$ lie in RC integration and voltage dividing.

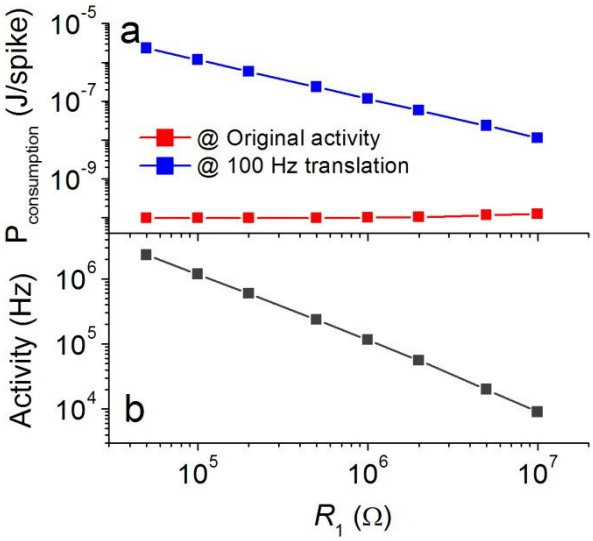


Figure S6. (a) The power consumption and (b) simulated activity of the PAO based on the inset of Figure 6.2c with respect to $R_1$ at constant $V_{in}$ (5 V). The blue line indicates translated power consumption at 100 Hz.

### *Slew rate effect on postsynaptic activity*

The postsynaptic activity $v$ with $R_{syn}$ was examined for different slew rates (2.5 – 2000 V/μs) at 100 gain by following the same calculation method in Sec. 6.3.6. The results are shown in Figure S7.

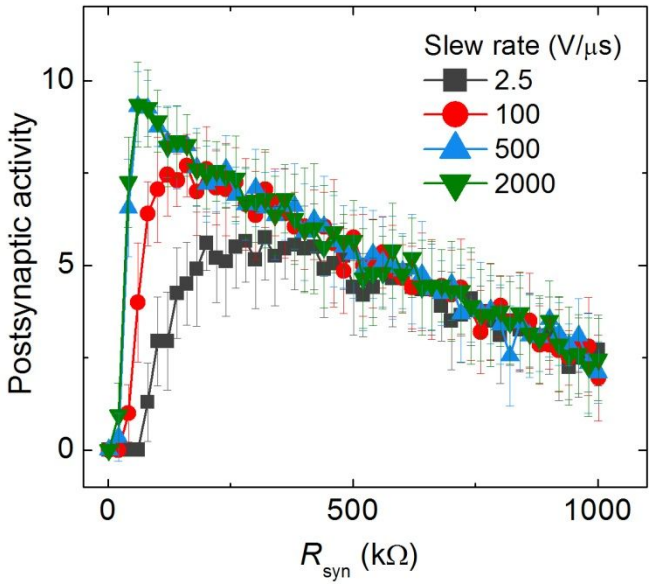


Figure S7. Postsynaptic activity induced by a presynaptic spike train ($\langle u \rangle$ = 17.6) with respect to $R_{syn}$ for different slew rates.

## *Bibliography*


[1] F. A. Kroger, H. J. Vink, *Solid State Phys.*, 3, 307 (1956).

[2] J. A. V. Butler, *Trans. Faraday Soc.*, 19, 729 (1924).

[3] C. Herring, M. H. Nichols, *Rev. Mod. Phys.*, 21, 185 (1949).

[4] D. S. Jeong, H. Schroeder, R. Waser, *Phys. Rev. B*, 79, 195317 (2009).

[5] C. R. Crowell, M. Beguwala, *Solid-State Electron.*, 14, 1149 (1971).

[6] K. W. Morton, D. Mayers, *Numerial solution of partial differential equations*, Cambridge University Press, Cambridge, UK 2005.

[7] D. S. Jeong, H. Schroeder, R. Waser, *Appl. Phys. Lett.*, 89, 082909 (2006).

[8] P. Dayan, L. F. Abbott, *Theoretical Neuroscience*, The MIT Press, Cambridge, MA, USA 2001.

# List of publications

## 1. Refereed Journal Articles (SCI)

### 1.1 Domestic

### 1.2. International

1. Doo Seok Jeong, Goon-Ho Park, **Hyungkwang Lim**, Cheol Seong Hwang, Suyoun Lee, and Byung-ki Cheong, "Dc current transport behavior in amorphous GeSe films", Appl. Phys. A, 102, 1027-1032 (2011)
2. Doo Seok Jeong, **Hyungkwang Lim**, Goon-Ho Park, Cheol Seong Hwang, Suyoun Lee, and Byung-ki Cheong, "Threshold resistive and capacitive switching behavior in binary amorphous GeSe", J. Appl. Phys., 111 102807 (2012)
3. Jun-Woo Park, Misun Song, Seokhyun Yoon, **Hyungkwang Lim**, Doo Seok Jeong, Byung-ki Cheong, and Hosun Lee, "Structural and optical properties of phase-change amorphous and crystalline $Ge_{1-x}Te_x$ ($0 < x < 1$) thin films", Phys. Status Solidi A, 2, 267-275 (2012)
4. **Hyungkwang Lim**, Inho Kim, Jin-Sang Kim, Cheol Seong Hwang, and Doo Seok Jeong, "Short-term memory of $TiO_2$-based electrochemical capacitors: empirical analysis with adoption of a sliding threshold", Nanotechnology, 24, 384005 (2013)
5. **Hyungkwang Lim**, Ho-Won Jang, Doh-Kwon Lee, Inho Kim, Cheol Seong Hwang, and Doo Seok Jeong, "Elastic resistance change and action potential generation of non-faradaic Pt/$TiO_2$/Pt capacitors", Nanoscale, 5, 6363-6371 (2013)

6. Hyung-Woo Ahn, Doo Seok Jeong, Byung-ki Cheong, Su-Dong Kim, Sang yeol Shin, **Hyungkwang Lim**, Donghwan Kim, and Suyoun Lee, "A study on the scalability of a selector device using threshold switching in Pt/GeSe/Pt", ECS Solid State Lett., 2, N31-N33 (2013)
7. Jun Yeong Seok, Seul Ji Song, Jung Ho Yoon, Kyung Jean Yoon, Tae Hyung Park, Dae Eun Kwon, **Hyungkwang Lim**, Gun Hwan Kim, Doo Seok Jeong, and Cheol Seong Hwang, "A review of three-dimensional resistive switching cross-bar array memories from the integration and materials property point of view", Adv. Funct. Mater., 24, 5316-5339 (2014)
8. Vladimir Kornijcuk, Omid Kavehei, **Hyungkwang Lim**, Jun Yeong Seok, Wook-Seong Lee, Seong Keun Kim, Inho Kim, Byung Joon Choi, Cheol Seong Hwang, and Doo Seok Jeong, "Multiprotocol-induced plasticity in artificial synapses", Nanoscale, 6, 15151-15160 (2014)
9. Seong Keun Kim, Shin Ik Kim, **Hyungkwang Lim**, Doo Seok Jeong, Beomjin Kwon, Seung-Hyub Baek, and Jin-Sang Kim, "Electric-field-induced Transport Transition at $LaAlO_3/SrTiO_3$ Heterointerface", Sci. Rep., 5, 8023 (2015)
10. **Hyungkwang Lim**, Vladimir Kornijcuk, Jun Yeong Seok, Omid Kavehei, Seong Keun Kim, Inho Kim, Cheol Seong Hwang, and Doo Seok Jeong, "Reliability of neural information conveyed by unreliable neuristor-based leaky integrate-and-fire neurons: a model study", Sci. Rep., 5, 9776 (2015)

# 2. CONFERENCES

## 2.1 Domestic

1. **Hyungkwang Lim**, Goon-Ho Park, Byung-Ki Cheong, Cheol Seong Hwang, and Doo Seok Jeong, "How to obtain intrinsic impedance spectra of a MIM cell formed in crossbar structure", 한국진공학회 제 40회 동계학술대회, 휘닉스파크, February 9-11 (2011)-oral

2. Goon-Ho Park, Seo Hee Son, **Hyungkwang Lim**, Doo Seok Jeong, Suyoun Lee, and Byung-Ki Cheong, "The electrical characterisitics of GeTe thin films with various Se contents for switching devices", 한국진공학회 제 40회 동계학술대회, 휘닉스파크, February 9-11 (2011)-oral
3. **Hyungkwang Lim**, Inho Kim, Jin-Sang Kim, Cheol Seong Hwang, and Doo Seok Jeong, "Short-term memory of TiO2-based electrochemical capacitors: empirical analysis with adoption of a sliding threshold", 한국물리학회 2013 봄학술대회, 대전컨벤션센터, April 24-26 (2013)-oral
4. Doo Seok Jeong, **Hyungkwang Lim**, Doh-Kwon Lee, and Cheol Seong Hwang, "Elastic resistance change and action potential generation of non-faradaic Pt/TiO2/Pt capacitors: room temperature kinetics of defect migration", 한국물리학회 2013 봄학술대회, 대전컨벤션센터, April 24-26 (2013)-oral

## 1.2 International

1. Zhe Wu, Gang Zhang, Young-Wook Park, **HyungKwang Lim**, Dongmin Kang, Ho-ki Lyeo, Doo Seok Jeong, Jeung-hyun Jeong, Kwangsoo No, and Byung-ki Cheong, "Controlled recrystallization for low-current reset programming characteristics of phase change memory with Ge-doped SbTe", 2011 MRS spring meeting, San Francisco, US, April 25-29 (2011)-oral
2. Doo Seok Jeong, Goon-Ho Park, **Hyungkwang Lim**, and Byung-ki Cheong, "Threshold switching in binary amorphous Pt/GeSe/Pt stacks', 2011 MRS spring meeting, San Francisco, US, April 25-29 (2011)-oral
3. Doo Seok Jeong, Goon-Ho Park, **Hyungkwang Lim**, Cheol Seong Hwang, Suyoun Lee, and Byung-ki Cheong, "Current transport behavior in amorphous GeSe films", 2011 MRS spring meeting, San Francisco, US, April 25-29 (2011)-poster

4. **Hyungkwang Lim**, Ho-Won Jang, Cheol Seong Hwang, and Doo Seok Jeong, "Room-temperature kinetics of defect migration in non-faradaic Pt/TiO2/Pt capacitors", Nature Conference 2012, Aachen, Germany, June 17-20 (2012)-contribution talk
5. **Hyungkwang Lim**, Ho-Won Jang, Cheol Seong Hwang, and Doo Seok Jeong, "Synaptic plasticity of electrochemical capacitors based on $TiO_2$", Nature Conference 2012, Aachen, Germany, June 17-20 (2012)-poster
6. Jun Yeong Seok, Seul Ji Song, Jung Ho Yoon, Kyung Jean Yoon, Tae Hyung park, Dae Eun Kwon, **Hungkwang Lim**, Gun Hwan Kim, Doo Seok Jeong, and Cheol Seong Hwang, "A Review of Three-dimensional Resistive Switching Cross-Bar Array Memories from the Integration and Materials Property Points of View", 2014 E-MRS, Lille, France, May 26-30 (2014)-invited
7. Jun Yeong Seok, Seul Ji Song, Jung Ho Yoon, Kyung Jean Yoon, Tae Hyung Park, Dae Eun Kwon, **Hyungkwang Lim**, Gun Hwan Kim, Doo Seok Jeong, and Cheol Seong Hwang, "A Review of Three-dimensional Resistive Switching Cross-Bar Array Memories from the Integration and Materials Property Points of View", 14th Annual Non-Volatile Memory Technology Symposium (NVMTS 2014), Jeju, Korea, October 27-29 (2014)-poster
8. **Hyungkwang Lim**, Jun Yeong Seok, Vladimir Kornijcuk, Cheol Seong Hwang, and Doo Seok Jeong, "Reliability of neural information conveyed by unreliable neuristor-based leaky integrate-and-fire neurons", International Conference on Electronic Materials and Nanotechnology for Green Environment (ENGE 2014), Jeju, Korea, November 16-19 (2014)-oral
9. Vladimir Kornijcuk, Omid Kavehei, **Hyungkwang Lim**, Jun Yeong Seok, Seong Keun Kim, Inho Kim, Byung Joon Choi, and Doo Seok Jeong, "Multiprotocol-induced Plasticity of Artificial Synapses, ' International Conference on Electronic Materials and Nanotechnology for Green Environment (ENGE 2014), Jeju, Korea, November 16-19 (2014)-oral

10. **Hyungkwang Lim**, Vladimir Kornijcuk, Jun Yeong Seok, Inho Kim, Seong Keun Kim, Cheol Seong Hwang, and Doo Seok Jeong, "Towards artificial electronic neurons and their noises", 2015 MRS Spring Meeting&Exhibit, San Francisco, US, April 6-10 (2015)-oral

# Abstract (in Korean)

인공신경망은 학습능력이라는 독특한 기능을 구현할 수 있기 때문에 많은 관심을 받아왔다. 최근에는 동적인 정보를 처리하기 위한 '스파이킹 인공신경망'에 대한 관심이 고조되고 있다. 하지만 소프트웨어 방식으로 동작하는 스파이킹 인공신경망의 경우, 연산시간이 비효율적으로 늘어나기 때문에 물리적으로 동작하는 하드웨어 기반의 스파이킹 인공신경망의 중요성이 높아지고 있다. 본 논문에서는 메모리/스위치 현상을 나타내는 저항변화 시스템을 연구하고 그 현상학적 특성을 이용하여 스파이킹 인공신경망의 기본구성요소인 뉴런과 시냅스의 기능 구현 개념연구를 진행하였다.

우선 인공시냅스의 단기가소성은 $TiO_2$ 와 반응성 금속 Cr, Ni, Ti 기반의 전기화학적 커패시터에서 산화환원 반응을 통해 구현되었다. 실험적으로, 인공시냅스의 시냅스 강화 현상은 생물시냅스에서 관찰되는 바와 같이 무한정 증가하지 않았다. 생물 시냅스 강화현상을 표현하는 Bienenstock-Cooper-Munro 경험식의 '움직이는 문턱' 개념을 도입하여 인공시냅스의 동역학적 시냅스 강도변화를 실험식으로 모사가능 하였으며 각각의 전기화학적 커패시터의 시냅스 강화현상을 수치정보화 하였다.

다음으로, 뉴런 세포막의 급격한 전도도 변화현상을 모사하기 위하여 세 종류의 스위치 시스템에 대한 연구를 수행하였다. 우선, $TiO_2$ 기반 비전기화학적 커패시터 시스템의 이온-블로킹 접촉과 저항신축성을 알아보기 위해 실험적, 이론적으로 전류-전압 이력현상을 분석하였다. 생물뉴런의 스파이크 생성현상을 유사한 현상을 관찰할 수 있었으나, 단독 비전기화학적 커패시터는 연속적인 스파이크를 생성하는 것은 불가능하였으며 단독 저항 스위치는 회로에 내장된 형태로 구현되어야 함을 확인하였다.

문턱스위를 내장한 neuristor-based leaky integrate and fire (NLIF) 뉴런의 거동을 시뮬레이션을 활용하여 이론적으로 예측하였다. NLIF 뉴런의 동역학적 특징은 2차원 위상면 분석을 통해 위상면 상의 분기선과 고정점의 조건으로 결정됨을 제시하였다. 주목할만한 점은 문턱스위치의 동작시마다 발생하는 동작 산포에 의해 뉴런잡음이 발생한다는 것으로, 결과적으로 이 잡음은 푸아송 분포와 비슷한 형태를 가지며 뉴런 정보전달의 신뢰도를 낮추게 된다. 정보전달의 신뢰도를 평가하기 위해서 군집 NLIF 뉴런을 통한 정보전달 시뮬레이션을 진행하였으며, 그 결과 문턱스위치의 동작산포에도 불구하고 높은 신뢰도의 정보전달이 이루어짐을 확인하였다.

마지막으로, 문턱스위치와 비이상 연산증폭기를 기반으로 한 relaxation oscillator-based leaky integrate-and-fire (ROLIF) 뉴런 회로를 제시하고, 개념연구를 진행하였다. 실험적으로 ROLIF 뉴런의 특성 4가지 즉, 아날로그 타입 정보 암호화, 신호 증폭, 일방향 신호전달, 푸아송 잡음을 평가, 분석하였다. 단일 ROLIF 뉴런의 특성 뿐 아니라 수동 시냅스를 적용하여 흥분성 연접후 전위증가 현상으로 인해 연접전 뉴런에서 연접후 뉴런으로 신호가 전달됨을 실험적으로 확인하였다. 제안된 뉴런모델의 특성을 일반화하기 위하여 다양한 이득값과 슬루율을 갖는 비이상 연산증폭기를 시뮬레이션하였으며 결과적으로, 특정 슬루율이 넘는 조건에서는 이득값이 지배적인 파라미터임을 확인하였다. 최종적으로, 하나의 연접후 뉴런이 다수의 연접전 뉴런과 연결된 경우에도 공간적 신호쌓기에 의한 흥분성 연접후 전위증가가를 예측할 수 있으며, 비동기적인 스파이크의 무작위 잡음이 핵심적인 역할을 수행함을 확인하였다.

**주요어:** 뉴로몰픽 공학, 인공시냅스, 인공뉴런, 문턱스위치, S-모양 음의 미분저항, 단기메모리, 전기화학적 커패시터, 비전기화학적 커패시터, 뉴런 잡음, Neuristor-based leaky integrate-and-fire 뉴런, Relaxation oscillator-based leaky integrate-and-fire 뉴런

**학번:** 2010-22768

임 형 광